

**Parameter Identification of a Flexible Beam
using a
Modal Domain Optical Fiber Sensor**

by

Charles Zachary Furness

Thesis submitted to the Faculty of the
Virginia Polytechnic Institute and State University
in partial fulfillment of the requirements for the degree of

MASTER OF SCIENCE

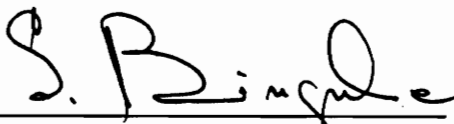
in

Electrical Engineering

APPROVED:



Douglas K. Lindner, Chairman



Stanoje P. Bingulat



Suzanne Weaver Smith

July 1990

Blacksburg, Virginia

LD

5655

V855

1990

F876

C. 2

**Parameter Identification of a Flexible Beam
using a
Modal Domain Optical Fiber Sensor**

by

Charles Zachary Furness

Douglas K. Lindner, Chairman

Electrical Engineering

(ABSTRACT)

An optical fiber sensor is used for identification of a cantilevered beam under conditions of various concentrated mass loadings. A model of the sensor as well as the dynamic system is developed and used to test the reliability of the identification. Input/output data from an experiment is gathered and used in the identification. A survey of the existing areas of damage detection and parameter identification is included, along with suggestions for incorporating fiber optic sensors into existing techniques. The goal of this research was to show that the fiber sensor can be used for identification purposes, and that it is sensitive to parameter changes within the system (in this case concentrated mass changes).

ACKNOWLEDGEMENTS

Without the help and encouragement of a great number of individuals, this work would never have been realized. I would like to extend my sincerest thanks and gratitude to the members of my thesis committee. Dr. Bingulac has contributed greatly in expanding my knowledge of system identification. Dr. Smith provided me with extensive insight of the damage detection and parameter estimation fields. My chairman, Dr. Lindner has shaped this research from its inception, and has given me valuable guidance throughout my graduate career.

I am forever indebted to David Cox for the development of the beam experiment. His expertise in the hardware implementation made the experimental work possible. More importantly, his friendship these past two years has made everything worthwhile.

Most of all, I'd like to thank my parents for their continuing support throughout my education. Without their encouragement and love, none of this would have been possible.

Finally, I'd like to dedicate this work to the memory of my grandfather, Dr. Charles Albert Browne, Jr. Although I never got a chance to meet him, his enthusiasm for science has always been a part of me.

TABLE OF CONTENTS

1.0	INTRODUCTION	1
1.1	Motivation	1
1.2	Goals of Research	4
2.0	REVIEW OF PARAMETER IDENTIFICATION AND DAMAGE DETECTION TECHNIQUES	6
2.1	Sensitivity Methods	6
2.2	Direct Methods	15
2.3	Applications for Damage Detection	26
3.0	MODEL DEVELOPMENT	31
3.1	Beam Dynamics	31
3.2	Fiber Optic Sensor	42
3.3	Piezoelectric Actuator	49
3.4	State Space Description	51

4.0	SYSTEM IDENTIFICATION	55
4.1	Eigensystem Realization Algorithm	55
4.2	Identification from Simulation	63
4.3	Impulse Response Estimation	67
4.4	Identification from Experiment	70
5.0	MASS IDENTIFICATION	84
5.1	Model Limitations	84
5.2	Identified Systems	91
5.3	Mass Identification from Simulation	97
5.4	Mass Identification from Experiment	102
6.0	CONCLUSIONS	105
6.1	Summary	105
6.2	Further Research	107
	APPENDIX A: SIMULATION PROGRAMS	110
	APPENDIX B: IDENTIFICATION PROGRAMS	124
	REFERENCES	130
	VITA	133

LIST OF FIGURES

FIGURE 1.1 Flow Chart of the Identification Process 2

FIGURE 3.1 Cantilevered Beam with Fiber Sensor, Piezoelectric, and Mass 33

FIGURE 3.2 Beam Frequencies for Different Mass Loadings..... 39

FIGURE 3.3 Intensity Pattern in a Dual-Mode Fiber 45

FIGURE 3.4 Intensity of the Fiber Output vs. Γ 48

FIGURE 4.1 Singular Values for Varying Levels of Measurement Noise 65

FIGURE 4.2 Experimental Set-up 72

FIGURE 4.3 Nine Measured Responses to a Pulse Input 75

FIGURE 4.4 Spectrum of Unaveraged, Averaged, and Noise Responses 76

FIGURE 4.5 Actual and Simulated Beam Responses 81

FIGURE 4.6 Bode Plot of Simulated and Identified Systems 82

FIGURE 4.7 Responses to Actual and Identified Systems 83

FIGURE 5.1	Identified and Theoretical Frequencies - $M_c/M_b = 0.10$	86
FIGURE 5.2	Identified and Theoretical Frequencies - $M_c/M_b = 0.33$	87
FIGURE 5.3	Identified and Theoretical Frequencies - $M_c/M_b = 0.65$	88
FIGURE 5.4	Simulated and Actual Responses for Varying Mass Loads	90
FIGURE 5.5	Mode Shapes and Derivatives for Varying Mass Loads	92
FIGURE 5.6	Inaccurate Identification due to Poor Sensor Placement	93
FIGURE 5.7	Identified and Actual Responses for Varying Mass Loads	98
FIGURE 5.8	Identified Bode Plots for Varying Mass Loads	99
FIGURE 5.9	Error Norms for Identified Frequencies of the System	101

LIST OF TABLES

TABLE 3.1	Normalization Constants for a Five Mode Model	54
TABLE 4.1	MAC Values for Various Levels of Measurement Noise	66
TABLE 4.2	Experimental Beam, Piezoelectric and Fiber Parameters	73
TABLE 4.3	Eigenvalues and MAC Values - ETFE vs. Pulse Input	78
TABLE 5.1	Eigenvalues and MAC Values for Varying Mass Loads	95
TABLE 5.2	Frequency Identification by FFT and ERA	96
TABLE 5.3	Actual and Identified Mass Parameters	103

1.0 INTRODUCTION

1.1 MOTIVATION

System identification consists of using input and output data to arrive at a mathematical model of the system at hand. It is important to be able to identify a system model in such areas as control, so that a control law can be adequately designed. It is also useful in validating analytical models. Identification is important in areas such as damage detection, where parameters of the system must be monitored for change. Parameter identification involves the detection of specific physical parameters of the system.

It would be an advantage to incorporate the control and identification into one system. The actuator that provides feedback in the control system, can also be used to generate input signals for identification. The response can then be measured using sensors distributed throughout the system. An identified model is determined and compared to an analytical one of the system. If a change has occurred, then the control law is updated and the system reconfigured. This process is summarized in Figure 1.1.

The most widely used methods of measuring the responses of the system are discrete sensors such as accelerometers and strain gauges. Typically, a large

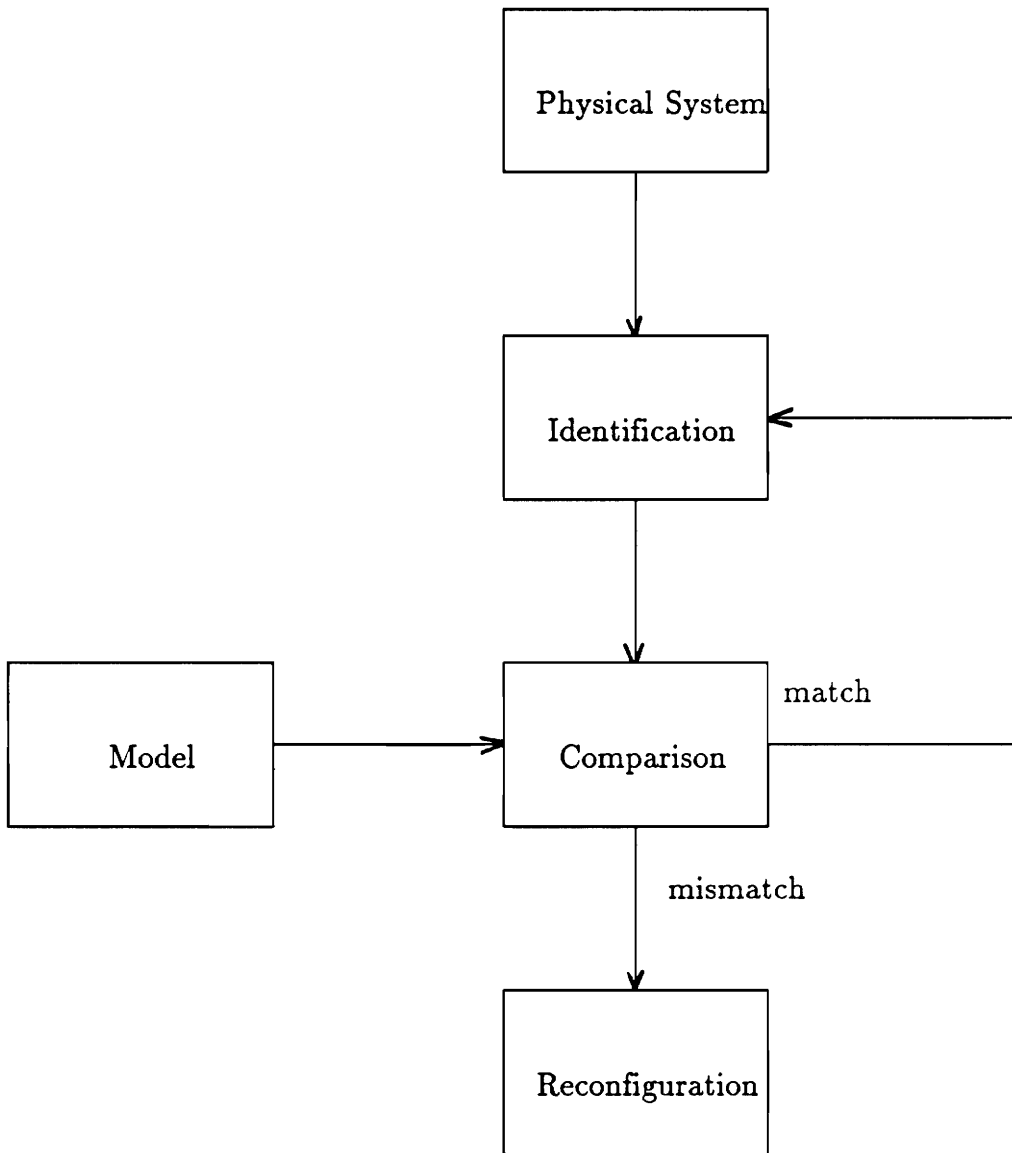


Figure 1.1 Flow Chart of the Identification Process

number of these sensors are placed throughout the structure in order to obtain an appropriate amount of spatial information. Recently, it has been shown that a modal domain fiber-optic sensor can be operated as a vibration transducer with a limited amount of measurement noise. This has led to the idea of using fiber-optic sensors as a tool for identification.

Besides having very low noise properties, these sensors consist of a continuous optical medium that could have advantages over discrete sensors. Since the sensing region spans the entire structure, an optical fiber might be better able to pick up information. A change that occurs in between two point sensors may not be as readily accessible. In addition, such sensors would have a decided advantage in convenience. It would be much easier to monitor one output from the fiber optic sensor than multiple outputs from many discrete sensors.

Previous work in damage detection using fiber-optic sensors has been limited to detecting damage due to breakage of the fiber itself. Measures [1] has embedded optical fibers in semi-transparent Kevlar composites and located damaged sections by detecting light leakage in broken fiber leads. This type of destructive testing is limited to situations in which the damage is great enough to break the fiber. In cases where damage does not break the fiber, one alternative method is to detect acoustic waves arising from cracks [2]. Other methods rely on using a mesh of optical fibers to derive strain fields in two dimensions [3].

The methods mentioned above all share the similar idea of detecting damage by direct measurement of some quantity (acoustic waves, light leakage, strain, etc.). In contrast, this research has concentrated on using the output of the sensor to identify a mathematical description of the system, and to monitor

this identified model for changes. An excellent review of existing parameter identification and system identification techniques can be found in [4].

1.2 GOALS OF RESEARCH

The main purpose of this research is to demonstrate that a modal domain fiber optic sensor can be used for system and parameter identification. The first objective was to show that the fiber could be used to identify a mathematical model, relating the input and output of the system. By instrumenting a fiber sensor on a cantilevered beam and measuring the response to a known excitation, it will be shown that a model of the system is identified that corresponds to the theoretical characteristics of the beam. In addition, it will be shown that the fiber is sensitive to changing parameters of the system. By adding a concentrated mass to the beam, the location and amount of the mass can be estimated from the identified model.

Chapter 2 contains a review of the important parameter identification techniques used in the structures community. Techniques are categorized as either sensitivity (iterative) or direct (non-iterative) methods. Some applications to damage detection are explored at the end of this chapter.

Chapter 3 develops the model of the cantilevered beam, fiber-optic sensor, and piezoelectric actuator. Mode shapes and frequencies are derived that are used in the derivation of the model.

A method known as the Eigensystem Realization Algorithm (ERA) is used to perform the system identification in Chapter 4. Coherence measures, that

quantify the accuracy of the identification are also derived. Two different methods of impulse response estimation are explored, which are used in conjunction with the ERA. The simulated and identified models are compared, using different performance criteria.

Finally, in Chapter 5 a series of concentrated masses are applied to the cantilevered beam and the identified frequencies are used in determining mass location and amount. The limitations of the model are discussed, as well as the resolution of mass location and amount. Simulated and experimental results are both presented.

2.0 REVIEW OF PARAMETER IDENTIFICATION AND DAMAGE DETECTION TECHNIQUES

In the past few years a number of identification techniques have gained popularity that seek to determine specific parameters in a flexible structure. In the following chapter a number of techniques that have as their goal the identification of mass and stiffness parameters, will be explored. Such techniques generally fall into one of two categories: sensitivity methods, which iteratively update the parameters until the desired convergence is achieved, or direct methods that generate a “best fit” of an updated model.

Stiffness information is especially important to identify, because it can be directly related to damage detection. Some applications of parameter identification to the problem of damage detection will also be explored.

2.1 SENSITIVITY METHODS

All sensitivity methods share the same basic concept. A set of parameters

is iteratively updated based on identified quantities, until convergence to the true parameters is achieved. Parameters are usually related to the physical make-up of the system, such as the mass or stiffness distributions. If the system model is discretized into a finite element model, then these distributions are represented by the magnitude of the elements in the mass and stiffness matrices. Identified quantities are usually the natural frequencies, eigenvalues, or mode shapes of the system. Such quantities are determined from the identified system model.

2.1.1 Problem Formulation

Consider a dynamical system governed by a set of linear differential equations of the form:

$$\mathbf{M}(\mathbf{p}) \ddot{\mathbf{x}} + \mathbf{K}(\mathbf{p}) \mathbf{x} = \mathbf{B}(\mathbf{p}) \mathbf{F}(t), \quad (2.1)$$

where

- \mathbf{M} = mass matrix,
- \mathbf{K} = stiffness matrix,
- $\mathbf{F}(t)$ = input forcing function,
- \mathbf{B} = ($m \times n$) input matrix (m - # inputs, n - degrees of freedom) and
- \mathbf{p} = parameter vector.

Damping effects have been neglected in (2.1). The matrices in (2.1) are arrived at by some analytical modeling technique (finite element, Rayleigh-Ritz, etc.). The \mathbf{M} and \mathbf{K} matrices are functions of the physical parameters of the system, such as mass distribution, modulus of elasticity, etc. A vector, \mathbf{p} , can be considered to be a collection of these parameters such that

$$\mathbf{p} = [p_1 \ p_2 \ p_3 \ \dots \ p_g]^T, \quad (2.2)$$

The eigenvalue problem associated with equation (2.1) is given by

$$(\mathbf{M} \Lambda^2 + \mathbf{K}) \Phi = 0, \quad (2.3)$$

where Λ is a matrix of eigenvalues displayed along the diagonal, and Φ is a matrix of associated eigenvectors. Eigenvalues of this problem are functions of the parameter vector, \mathbf{p} , since the mass and stiffness matrices are functions of the parameter vector. For lightly damped structures, the eigenvalues of the system are related to the natural frequencies in the usual manner

$$\omega_i(\mathbf{p}_o) = \sqrt{\lambda_i(\mathbf{p}_o)} \quad i = 1, 2, \dots, h \quad (2.4)$$

and the h identified frequencies are a function of the system parameters such that

$$\tilde{\omega} = f(\mathbf{p}_o + \Delta\mathbf{p}), \quad (2.5)$$

where $\tilde{\omega}$, is a vector of the h identified frequencies, \mathbf{p}_o is the initial parameter estimate, and $\Delta\mathbf{p}$, the parameter update. Equation (2.5) can be expanded with a Taylor series around the initial parameter estimate to give [5]

$$\tilde{\omega} = f(\mathbf{p}_o) + \left. \frac{\partial f(\mathbf{p})}{\partial \mathbf{p}} \right|_{\mathbf{p}_o} \Delta\mathbf{p} + \dots, \quad (2.6)$$

where

$\frac{\partial f(\mathbf{p})}{\partial \mathbf{p}}$ - is a Jacobian matrix containing frequency sensitivities to the structural parameters.

and the higher order terms have been neglected in the Taylor expansion.

The heart of this analysis lies in the determination of the Jacobian matrix. This matrix is determined as

$$\left[\frac{\partial f_i}{\partial \mathbf{p}_j} \right] = \frac{\Phi_i^T \left[\frac{\partial \mathbf{K}}{\partial \mathbf{p}_j} - \omega_i^2 \frac{\partial \mathbf{M}}{\partial \mathbf{p}_j} \right] \Phi_i}{2\omega_i \Phi_i^T \mathbf{M} \Phi_i}. \quad (2.7)$$

Partial derivatives in the numerator of (2.7) can be found from the particular model that relates the set of parameters, \mathbf{p} , to the mass and stiffness matrices. However, in complicated structures this computation must be done numerically. Once, the Jacobian matrix is determined, the parameter update, $\Delta \mathbf{p}$, can be found from

$$\Delta \mathbf{p} = \left[\frac{\partial f}{\partial \mathbf{p}} \right]^{-1} \Delta \omega, \quad (2.8)$$

where $\Delta \omega = \tilde{\omega} - \omega$. In the case where more measurements are available than parameters, $\Delta \mathbf{p}$ can be solved for in a least square sense as follows:

$$\Delta \mathbf{p} = \left(\left[\frac{\partial f}{\partial \mathbf{p}} \right]^T \mathbf{W} \left[\frac{\partial f}{\partial \mathbf{p}} \right] \right)^{-1} \left[\frac{\partial f}{\partial \mathbf{p}} \right]^T \mathbf{W} \Delta \omega, \quad (2.9)$$

where \mathbf{W} is a weighting matrix. The final step is to update the parameter vector by

$$\mathbf{p} = \mathbf{p}_o + \Delta \mathbf{p}. \quad (2.10)$$

Creamer and Hendricks [5], use the development above to arrive at

parameter estimates of the physical structural quantities. Their method uses W as the inverse of the measurement error covariance matrix. Parameter updates from (2.9) are used as initial parameter estimates in (2.6) so that the routine is run iteratively until the desired convergence is established. One problem with this algorithm is that it requires a number of known parameters in order to converge. Creamer and Hendricks also showed that information of the mass and length scale is a necessary condition, but not always a sufficient one. In other words, mass and length at a few locations must be known *a priori*, for convergence to be likely. Because of this difficulty with convergence, care must be exercised in using this method.

2.1.2 Rayleigh-Ritz Method

An identification algorithm based on the Rayleigh-Ritz method is described by Norris and Meirovitch [6]. This method uses a Rayleigh-Ritz model of the structure to update a set of parameters in the same way that was presented in the previous section. The difference is that the parameters in this case are the coefficients of a mass and stiffness distribution expansion. A general description of the Rayleigh-Ritz modeling method will first be presented, along with a description of the parameter identification method.

Mass and stiffness matrices of a structure can be determined using the mode shapes of the structure in the following way [7]:

$$\mathbf{M} = \int_0^l \mu(z) \psi_i \psi_j dz \quad i, j = 1, 2, \dots, n, \quad (2.11)$$

$$\mathbf{K} = \int_0^l \sigma(z) \psi_i'' \psi_j'' dz \quad i, j = 1, 2, \dots, n, \quad (2.12)$$

where $\mu(z)$ and $\sigma(z)$ are the mass and stiffness distributions respectively, and ψ_i are the mode shapes. By using a finite number of modes in the model, a reasonable set of equations governing the dynamics of the system can be obtained. The Rayleigh-Ritz method is based on approximating the mode shapes with a given set of eigenfunctions, $\phi_i(z)$ as follows

$$\psi_i(z) = c_1 \phi_1(z) + c_2 \phi_2(z) + \dots + c_n \phi_n(z), \quad (2.13)$$

where the values c_i , are scalar multiples. The spatial functions, $\phi_i(z)$, need only be functions satisfying the boundary conditions of the problem. The greater the number of eigenfunctions used, the better the approximation of the model.

After determination of the mass and stiffness matrices, the eigenvalue problem reduces to (2.3) (where the damping of the structure has been omitted). Frequencies of the model can be determined in the usual way.

It is possible to make an estimation of the mass distribution of the beam based on the identification of the natural frequencies of the structure. The idea is to identify the frequencies of the structure and iteratively update a parameter vector using the Rayleigh-Ritz model. Under ideal conditions, the parameter updates will eventually converge to the true parameters of the system.

If the unknown mass and stiffness distributions are expanded with a series of basis functions, they can be written as

$$\mu(z) = \sum_{i=1}^n \alpha_i \chi_i(z) \quad \sigma(z) = \sum_{i=1}^m \beta_i \kappa_i(z). \quad (2.14)$$

A parameter vector, \mathbf{p} , that contains the coefficients in (2.14) is given by

$$\mathbf{p} = [\alpha_1 \ \alpha_2 \ \cdots \ \alpha_n \ \beta_1 \ \beta_2 \ \cdots \ \beta_m]. \quad (2.15)$$

The first step in the algorithm involves making a choice of the initial parameter estimate vector. Based on this choice, the mass and stiffness matrices (\mathbf{M}_{rs} , \mathbf{K}_{rs}) can be generated in the same way as in the Rayleigh-Ritz method:

$$\mathbf{M}_{rs} = \int_0^l \left(\sum_{i=1}^n \alpha_i \chi_i \right) \psi_r \psi_s dz = \sum_{i=1}^n \alpha_i \int_0^l \chi_i \psi_r \psi_s dz = \sum_{i=1}^n \alpha_i m_{rsi} \quad (2.16)$$

and

$$\mathbf{K}_{rs} = \int_0^l \left(\sum_{i=1}^m \beta_i \kappa_i \right) \psi_r'' \psi_s'' dz = \sum_{i=1}^m \beta_i \int_0^l \kappa_i \psi_r'' \psi_s'' dz = \sum_{i=1}^m \beta_i k_{rsi}. \quad (2.17)$$

Once again, the eigenvalue problem reduces to the form of (2.3) and the frequencies can be determined. Once the frequencies of the system under investigation are identified, then the difference between the identified values, $\tilde{\omega}$, and the model estimates, ω , can be expressed as

$$\Delta\omega = \tilde{\omega} - \omega \quad (2.18)$$

The change in frequency is related to the change in the parameter vector through

equation (2.6) in the previous section. Elements of the Jacobian matrix $[\partial\omega/\partial\mathbf{p}]$ can be computed from the following

$$\frac{\partial\omega_i}{\partial\mathbf{p}_j} = \frac{1}{2\omega_i} \left[\mathbf{u}_i^\top \frac{\partial\mathbf{K}}{\partial\mathbf{p}_j} \mathbf{u}_i - \omega_i^2 \mathbf{u}_i^\top \frac{\partial\mathbf{M}}{\partial\mathbf{p}_j} \mathbf{u}_i \right] \quad i = 1, 2, \dots, f \quad j = 1, 2, \dots, n+m. \quad (2.19)$$

The stiffness and mass sensitivities above can be calculated using (2.16) and (2.17):

$$\frac{\partial\mathbf{K}}{\partial\mathbf{p}_j} = \Theta \quad \frac{\partial\mathbf{M}}{\partial\mathbf{p}_j} = \mathbf{m}_{r,sj} \quad j = 1, 2, \dots, n \quad (2.20)$$

$$\frac{\partial\mathbf{K}}{\partial\mathbf{p}_j} = \mathbf{k}_{r,sj} \quad \frac{\partial\mathbf{M}}{\partial\mathbf{p}_j} = \Theta \quad j = n+1, n+2, \dots, n+m ,$$

where Θ is a null matrix of appropriate order. The change in the parameter vector is found as in the previous section and updated accordingly.

The advantage of this method lies in the fact that the only information that needs to be identified is the set of vibration frequencies of the system. No displacement information needs to be measured and no mode shapes of the system need to be estimated. However, the drawbacks of this technique are that for a highly nonlinear mass and stiffness distribution, the expansion in (2.16) and (2.17) will contain a large number of coefficients. The choice of the expansion functions is very important, in that the proper choice could limit the need for a large number of coefficients.

2.1.3 Over-determined Systems

In the previous section, a sensitivity method was presented that relied on having as many or more frequencies available than parameters to be estimated. In general, there are a more parameters to be solved for than measurements available, leading to an over-determined system of equations. A technique was developed by Chen and Garba [8] to deal with such situations.

Equation (2.8) relating identified frequencies to parameter changes can be rewritten as

$$[\Delta\omega_1, \Delta\omega_2, \dots, \Delta\omega_m]^T = \left[\frac{\partial\omega}{\partial p} \right] [\Delta p_1, \Delta p_2, \dots, \Delta p_n]^T, \quad (2.21)$$

where there are now m identified frequencies and n parameter estimates ($n > m$). Chen and Garba begin by defining the quantity

$$Q = (\Delta p_1)^2 + (\Delta p_2)^2 + \dots + (\Delta p_n)^2. \quad (2.22)$$

A solution is sought to minimize Q , and satisfy (2.21). The first m parameter updates are also functions of the last $(n - m)$ parameter updates. With m frequencies available, the parameter changes can be written as

$$\begin{bmatrix} \Delta p_1 \\ \Delta p_2 \\ \vdots \\ \Delta p_m \end{bmatrix} = f(\Delta p_{m+1}, \Delta p_{m+2}, \dots, \Delta p_n) \quad (2.23)$$

and Q can be minimized as

$$\frac{\partial Q}{\partial \Delta p_{m+1}} = \frac{\partial Q}{\partial \Delta p_{m+2}} = \dots = \frac{\partial Q}{\partial \Delta p_n} = 0. \quad (2.24)$$

Equation (2.24) generates a set of $(n-m)$ equations while (2.21) contains m equations. The unknown quantities, Δp_i , are solved for from these two sets of equations. As in the previous sections, the parameter vector update can be iterated until convergence is achieved.

In all of the sensitivity methods described above, the parameter changes were related to the frequency changes in a linear fashion. This was the result of truncating terms in the Taylor series expansion of (2.6). Due to this linear approximation, these methods only work well for small parameter changes. For large changes to the system, the linear approximations are no longer valid and the convergence of the algorithm is suspect.

2.2 DIRECT METHODS

Direct parameter identification methods refer to those methods that are non-iterative. Parameter estimates in these methods seek to satisfy some constraints imposed by the physical nature of the problem. Common constraints are the orthogonality of the eigenvectors with respect to the mass and stiffness matrices. Direct methods adjust a mathematical model of the structure to be more consistent with the measured data.

Methods described in this section depend upon an original mathematical

model of the system. This is typically a finite element model, whose order is taken to be the number of sensors on the structure. If the system undergoes some change (additive mass, damage, etc.), the original model no longer describes the current system. Measured data from a structure is used to determine a set of mode shapes, which are used to update the original model. The updated model is then analyzed to determine the parameter that has undergone change.

2.2.1 Model Correction Based on Measured Data

Berman [9] has developed a method of updating a finite element mass matrix to reflect the properties of a changing system. The method is based on the experimental determination of the system mode shapes and the use of the orthogonality condition of the mode shapes with the mass distribution.

Assume that an initial model of a structure is developed that contains an $(n \times n)$ analytical mass matrix, \mathbf{M}_a . If displacement measurements are made at various points along the structure for each mode and if the model is an exact representation of the dynamics of the structure, then the following orthogonality relationship holds

$$\Phi^T \mathbf{M}_a \Phi = \mathbf{I}, \quad (2.25)$$

where Φ is an $(n \times m)$ matrix of m mode shape vectors, each with n degrees of freedom, corresponding to the number of sensors on the structure. If a mass change occurs somewhere within the structure, then a corrected mass matrix must

meet the requirements that

$$\Phi^T(\mathbf{M}_a + \Delta\mathbf{M})\Phi = \mathbf{I} \quad (2.26)$$

and Φ is now a matrix of mode displacement measurements from the changed structure. The goal is to determine the matrix $\Delta\mathbf{M}$ from the measured displacement so that the analytical model can be updated. Rewriting (2.26) gives

$$\Phi^T\Delta\mathbf{M}\Phi = \mathbf{I} - \Phi^T\mathbf{M}_a\Phi = \mathbf{I} - \mathfrak{M}_a. \quad (2.27)$$

Berman minimizes $\Delta\mathbf{M}$ through the function

$$\epsilon_m = \left[\mathbf{M}_a^{-1/2}\Delta\mathbf{M}\mathbf{M}_a^{-1/2} \right]. \quad (2.28)$$

If a Lagrange multiplier, λ_{ij} , is defined for each element of (2.27), then a Lagrangian function may be written as follows [9]

$$\mathfrak{L} = \epsilon_m + \sum_{i=1}^m \sum_{j=1}^m \lambda_{ij} (\Phi^T\Delta\mathbf{M}\Phi - \mathbf{I} + \mathfrak{M}_a)_{ij}. \quad (2.29)$$

Equation (2.29) is differentiated with respect to the elements of $\Delta\mathbf{M}$, and the results set equal to zero. This calculation results in

$$2\mathbf{M}_a^{-1}\Delta\mathbf{M}\mathbf{M}_a^{-1} + \Phi\Lambda^T\Phi^T = 0 \quad (2.30)$$

and

$$\Delta\mathbf{M} = -\frac{1}{2}\mathbf{M}_a\Phi\Lambda^T\Phi^T\mathbf{M}_a. \quad (2.31)$$

The eigenvalues, Λ , can be solved for by substituting (2.31) into (2.26). The result is

$$\Lambda = -2 \mathfrak{M}_a^{-1}(\mathbf{I} - \mathfrak{M}_a) \mathfrak{M}_a^{-1}. \quad (2.32)$$

The mass change, $\Delta\mathbf{M}$, can now be solved for in terms of the available quantities

$$\Delta\mathbf{M} = \mathbf{M}_a \Phi \mathfrak{M}_a^{-1}(\mathbf{I} - \mathfrak{M}_a) \mathfrak{M}_a^{-1} \Phi^T \mathbf{M}_a \quad (2.33)$$

and a corrected mass matrix can be determined. Berman and Nagy [10] applied this technique to update a stiffness matrix from the updated mass matrix. Their derivation begins with

$$\mathbf{K}\Phi = \mathbf{M}\Phi\Omega^2 \quad (2.34)$$

or

$$\Phi^T \mathbf{K} \Phi = \Omega^2.$$

If similar minimization procedure is applied to the stiffness correction as was applied to the mass matrix correction, an analogous quantity can be defined as

$$\epsilon_k = \left| \mathbf{M}^{-1/2}(\Delta\mathbf{K})\mathbf{M}^{-1/2} \right| \quad (2.35)$$

and the stiffness matrix correction term is determined to be

$$\Delta\mathbf{K} = -\mathbf{K}_a \Phi \Phi^T \mathbf{M} - \mathbf{M} \Phi \Phi^T \mathbf{K}_a + \mathbf{M} \Phi \Omega^2 \Phi^T \mathbf{M} + \mathbf{M} \Phi \Phi^T \mathbf{K}_a \Phi \Phi^T \mathbf{M} \quad (2.36)$$

where

M - is the corrected mass matrix and
K_a - is the original stiffness matrix.

The major drawback to this method is that it does not preserve sparsity of the original mass and stiffness matrices. The original mass matrix will contain diagonal elements that reflect the mass distribution at various points along the beam. The original stiffness matrix will be block diagonal, and will also reflect the distribution of stiffness. Using the method above, off diagonal elements of both matrices become nonzero, so that unrealistic coupling occurs. As sparsity is lost, the updated model no longer displays the correct mass and stiffness distributions along the diagonal. Despite this restriction, the updated models do correctly reflect the measured data and often contain enough information to approximate the location of the system change.

In many experimental cases there are a limited number of sensor locations. It would be desirable to interpolate other displacement values along a structure, given the limited set of available measurements. If mode shape displacements are determined at a subset of the coordinates of the analytical model, the model can be rearranged as follows [10]

$$\left\{ \begin{bmatrix} K_1 & K_2 \\ K_2^T & K_3 \end{bmatrix} - \Omega_i^2 \begin{bmatrix} M_1 & M_2 \\ M_2^T & M_3 \end{bmatrix} \right\} \begin{bmatrix} \Phi_{1i} \\ \Phi_{2i} \end{bmatrix} = 0, \quad (2.37)$$

where

and Φ_{1i} - is a vector corresponding to the *i*th mode measured displacements
 Φ_{2i} - is a vector of unknown modal displacements.

The unknown displacements, Φ_{2i} , are found in terms of the measured values from

$$\Phi_{2i} = -(\mathbf{K}_3 - \Omega_i^2 \mathbf{M}_3)^{-1} (\mathbf{K}_2^T - \Omega_i^2 \mathbf{M}_2^T) \Phi_{1i}. \quad (2.38)$$

Determination of the mass and stiffness matrix corrections proceeds as before.

2.2.2 Perturbation Techniques

White and Maytum [11] have developed a matrix perturbation technique that updates an initial model to fit the measured data from a physical system. Like the method above, it postulates an initial model in terms of mass and stiffness matrices and seeks to perturb them in such a way that they will better reflect the actual system. Once again, the starting point in the derivation is the statement of the eigenvalue problem

$$\mathbf{K}\Phi = \mathbf{M}\Phi\Omega^2. \quad (2.39)$$

Updated matrices are assumed to be a linear combination of scale factors such that

$$\mathbf{M} = \mathbf{M}_o + \sum_{i=1}^m \alpha_i \mathbf{M}_i \quad (2.40)$$

and

$$\mathbf{K} = \mathbf{K}_o + \sum_{j=1}^n \beta_j \mathbf{K}_j, \quad (2.41)$$

where

\mathbf{M}_o - initial mass matrix,
 \mathbf{K}_o - initial stiffness matrix, and
 α, β - scale factors.

The true and approximate eigenvectors are related in the following manner

$$\Phi = \Phi_o \Psi, \quad (2.42)$$

where Φ is the true modal matrix, Φ_o is the initial modal matrix and Ψ is a general transformation matrix. Substitution of (2.40) and (2.41) into (2.39) yields

$$(\mathbf{K}_o + \sum_{j=1}^n \beta_j \mathbf{K}_j) \Phi = (\mathbf{M}_o + \sum_{i=1}^m \alpha_i \mathbf{M}_i) \Phi \Omega^2 \quad (2.43)$$

and using (2.42), and multiplying through by Φ_o^T , the equation can be rewritten as

$$(\Omega_o^2 + \sum_{j=1}^n \beta_j \Phi_o^T \mathbf{K}_j \Phi_o) \Psi = (\mathbf{I} + \sum_{i=1}^m \alpha_i \Phi_o^T \mathbf{M}_i \Phi_o) \Psi \Omega^2, \quad (2.44)$$

where Ω_o^2 is found from

$$\mathbf{K}_o \Phi_o = \mathbf{M}_o \Phi_o \Omega_o^2. \quad (2.45)$$

To solve for the scale factors, an approximation is made in (2.44) that the initial modal matrix, Φ_o , is equal to the true modal matrix, Φ (let $\Psi = \mathbf{I}$). This simplification results in the k th row of (2.44) becoming

$$\Omega_{o_k}^2 - \Omega_k^2 = \Omega_k^2 \sum_{i=1}^m \alpha_i \Phi_{o_k}^T \mathbf{M}_i \Phi_{o_k} - \sum_{j=1}^n \beta_j \Phi_{o_k}^T \mathbf{K}_j \Phi_{o_k} \quad (2.46)$$

$$= \mathbf{E}_o \begin{bmatrix} \alpha \\ \beta \end{bmatrix}.$$

The matrix \mathbf{E}_o represents the energy distribution of each mode of the original model [11]. The scale factors are determined with a least squares solution to give

$$\begin{bmatrix} \alpha \\ \beta \end{bmatrix} = (\mathbf{E}_o^T \mathbf{E}_o)^{-1} \mathbf{E}_o^T (\Omega^2 - \Omega_o^2). \quad (2.47)$$

2.2.3 Distributed Parameter Identification

The two previous direct methods have used identification techniques that have dealt with the identification of lumped mass parameters within a finite element model. A method developed by Baruh and Meirovitch [12] identifies the mass and stiffness distributions directly. This is accomplished by expanding the distributions with an infinite series and by solving for the coefficients in the series. The case of the mass distribution is considered below. A similar method holds for the identification of stiffness information.

The mass distribution expansion, as in (2.14), is

$$\mu(z) = \sum_{i=1}^{\infty} \alpha_i \chi_i(z), \quad (2.48)$$

where α_i are the undetermined coefficients. Once again, the orthogonality condition requires that

$$\int_0^l \mu(z) \psi_n \psi_m dz = \delta_{nm}. \quad (2.49)$$

If mode shapes can be determined to within a multiplicative constant, β , then the measured mode shape, ψ_i , can be written as

$$\hat{\psi}_i = \beta_i \psi_i \quad (2.50)$$

and (2.49) can be rewritten as

$$\int_0^l \mu(z) \hat{\psi}_n \hat{\psi}_m dz = \beta_n \beta_m \int_0^l \mu(z) \psi_n \psi_m dz = \beta_n^2 \delta_{nm}. \quad (2.51)$$

Substituting (2.48) into (2.51) and truncating the summation at p terms yields

$$\int_0^l \mu(z) \hat{\psi}_n \hat{\psi}_m dz = \sum_{i=1}^p \alpha_i \int_0^l \chi_i \hat{\psi}_n \hat{\psi}_m dz = \beta_n^2 \delta_{nm}. \quad (2.52)$$

From (2.52) it can be seen that if the mode shapes, ψ_i , and the spatial functions, χ_i , are known, then the coefficients are found by solving a system of linear equations:

$$\sum_{i=1}^p \alpha_i U_{nmi} = \beta_n^2 \delta_{nm}, \quad (2.53)$$

where

$$U_{nmi} = \int_0^l \chi_i \hat{\psi}_n \hat{\psi}_m dz. \quad (2.54)$$

Equation (2.54) can be rewritten in matrix form as

$$[\mathbf{T} : \mathbf{U}] [\boldsymbol{\beta}^T : \boldsymbol{\alpha}^T] = \boldsymbol{\Theta}, \quad (2.55)$$

where

$$\boldsymbol{\beta}^T = [\beta_1^2 \ \beta_2^2 \ \dots \ \beta_q^2], \quad (2.56)$$

$$\boldsymbol{\alpha}^T = [\alpha_1 \ \alpha_2 \ \dots \ \alpha_p],$$

$$\mathbf{U} = \begin{bmatrix} U_{111} & U_{112} & \dots & U_{11p} \\ U_{121} & U_{122} & \dots & U_{12p} \\ \vdots & \vdots & \ddots & \vdots \\ U_{q(q-1)1} & U_{q(q-1)2} & \ddots & \\ U_{qq1} & \dots & \dots & U_{qqp} \end{bmatrix},$$

and

$$\mathbf{T} = \begin{bmatrix} -1 & 0 & \dots & \dots & 0 \\ \vdots & \ddots & \ddots & \ddots & \vdots \\ 0 & -1 & 0 & \dots & 0 \\ \vdots & \ddots & \ddots & \ddots & \vdots \\ 0 & \dots & \dots & 0 & -1 \end{bmatrix}.$$

The index q refers to the number of modes to be used. The matrix \mathbf{T} has $q(q+1)/2$ rows and q columns. \mathbf{U} contains the same number of rows as \mathbf{T} but has p columns corresponding to the number of coefficients to be kept in the mass distribution expansion. The matrix \mathbf{T} contains zeros everywhere except at locations, $\mathbf{T}_{i,j}$, where $i = 1+q-l$ ($l = q, q-1, \dots, 1$) and $j = 1, 2, \dots, p$.

A unique solution to (2.55) does not exist due to the right side of the equation being zero. Therefore, additional information must be appended to (2.55) for a solution to exist. If the mass distribution at a point, z_0 , is known, the solution becomes:

$$\begin{bmatrix} \mathbf{T} & \mathbf{U} \\ 0 & \chi^T \end{bmatrix} \begin{bmatrix} \beta \\ \alpha \end{bmatrix} = \begin{bmatrix} \theta \\ \mu(z_0) \end{bmatrix} \quad (2.57)$$

where

$$\chi^T = [\chi_1(z_0), \chi_2(z_0), \dots, \chi_p(z_0)] \quad (2.58)$$

The solution of equation (2.57) can be found from which the coefficients, α_i , are determined. Once this has been done, an estimate of the mass distribution is made using the required summation.

If the mass distribution changes drastically, as is the case for a concentrated mass being placed on a beam, a large number of coefficients will be needed in (2.57). A judicious choice of basis functions, χ , will keep the number of terms to a minimum. If the basis functions are chosen to be sinusoidal, as in the case of a Fourier series expansion, then a large number would be needed in order to approximate the distribution. Another possibility is to use the mode shapes themselves. Another choice could be to use pulses that are shifted in space along the beam length. However, these functions do not span the entire space of the mass distribution, and a large number of pulses with small pulse widths would be needed.

2.3 APPLICATIONS FOR DAMAGE DETECTION

The techniques outlined above have a wide range of applications in areas such as buildings, aircraft, and space platforms, where structures must be monitored for change. Because such structures are very large and intricately designed, it is unrealistic to monitor every point in looking for damage. Also, damaged areas may not be detectable with visual, x-ray, or ultrasonic scanning methods. Identification through dynamic testing has the advantage of revealing such flaws by changes in the response of the system.

In many structures that suffer internal damage, a number of valid assumptions can be used to determine a damaged location. For instance, in most cases it can be assumed that the mass of the structure is unchanged. In cases where the structure has undergone permanent deformation, or a loss of internal adhesion, the mass of the structure will not change. Frequency response analysis may show a shift in the natural frequencies of the structure or more subtle changes in the shape of the frequency response function. Since the mass is unchanged, stiffness or damping properties must have changed, indicating that damage has occurred.

The difficult task is to pinpoint the damaged location from the identified model of the damaged system. In general, one cannot infer where damage has occurred by examining changes to the frequency response function. However, if a particular mode of vibration is seen to change, and that vibration is tied to a particular part of the structure, then conclusions about the type of damage may be drawn. Detection schemes that interrogate small areas of a structure might also be used, although it is often difficult to isolate specific areas from the rest of

the structure. Another possibility is one suggested by Hajela [13]. Hajela uses approximate methods, such as modeling large space trusses as beams, in order to gain a first estimate to damaged locations. Once a general area of damage has been established, he reverts to more sophisticated models to refine the location.

In the rest of this chapter, damage detection techniques applied to three different structural disciplines will be reviewed. These areas are in buildings, aircraft, and large flexible space structures.

2.3.1 Buildings

Because of their large size and complexity, it would be costly and time consuming to search for damaged areas within a building by carefully scrutinizing the entire structure. Dynamic testing of the structure, resulting in modal information is much more practical. A comparison of modal data taken over a period of time would show whether or not important structural properties were changing over time. A shift in the frequency spectra over time might indicate that internal damage has occurred.

Kircher [14], looked at frequency response measurements of identically designed buildings in an effort to determine changes due to earthquake damage. Ideally, response measurements would show the same shape, excluding small variations that exist. Kirchner also looked at smaller areas of each structure, taking measurements of different floors within each building. It was hoped that damage could be detected within a smaller area by monitoring the frequency response of the isolated subsection.

Kircher's work found that the power spectra of identically designed buildings were similar, although each building had discernable differences. He also found that those buildings that were built by the same contractor showed power spectra that were most similar. Measurements taken at specific locations within a building over a time period of inactivity did not change. Therefore, such areas could be periodically monitored for structural damage.

2.3.2 Aircraft

West [15] has used dynamic testing methods to determine damage in a wing flap of the Space Shuttle Orbiter. Modal testing was of particular interest in this case because the area under investigation was covered with protective thermal tiles. It was desirable to determine if damage could be detected without removal of the tiles. The analysis consisted of removing a section of the Orbiter body flap and subjecting it to an environment that would create internal damage to the flap. Modal data taken both before and after exposure were compared and analyzed for damage detection.

The results of modal testing showed a significant shift in the modal frequencies after exposure of the flap. Surprisingly though, x-ray and ultrasonic inspections failed to detect any changes to the system. In addition, West was able to infer that the damage was restricted to only a few areas of the structure, from his knowledge of the bending and torsional modes of the flap. Upon disassembly, two of the three inferences were seen to be correct.

Much of the success of this experiment lay in the off-line analysis used.

Such damage detection techniques for “real time” systems are much more difficult. Problems arise in exciting structural responses while operating on-line.

2.3.3 Space Structures

Much of the damage detection work that is seen in the literature is driven by research on large space structures. Such structures are inaccessible for inspection because of the surrounding hostile environment, making them prime candidates for modal testing. It is desirable that such structures be monitored for changes induced by vibration or by external disturbances. However, since the structure must be monitored while in orbit, the determination of specific areas of damage can be difficult.

Smith and Hendricks [16] used a technique to identify the stiffness parameters of a “damaged” truss model and look for changes between the original and the damaged model. Damage consisted of removing of one of the truss members and the goal was to determine how well the missing element could be located. By making measurements of the mode shapes of the object, a stiffness matrix was determined using a technique known as Kabe’s method [17]. The advantage of this method is that it preserves the sparsity of the original model. Initially zero off-diagonal elements remain zero and the change in stiffness can be better interpreted from the non-zero elements of the stiffness matrix. Elements of reduced stiffness were searched for that would signify the missing truss element. Location of the reduced element in the matrix determines the location within the structure.

The analysis was conducted on two simulated truss structures - a ten bay planar truss, and a ten bay tetrahedral truss. In both cases, simulated damage in the form of removed members was detected and located. The results also showed that the identification performed well with a limited amount of modal data - only the first three elastic modes were used. Drawbacks included the large computational effort required with Kabe's method, and the insensitivity of some structural members to detection.

2.3.4 Composites

Damage detection in composite materials has, in the past, been limited to qualitative analysis using x-ray, ultrasonic, and visual scanning techniques. The use of fiber-optic sensors for such detection has been mentioned previously [1]-[3]. However, these methods do not provide quantitative information such as stiffness distribution.

Soeiro and Hajela [18] have investigated damage detection in composite materials by identifying areas of reduced stiffness in a composite structure. Their work consisted of developing analytical models of a composite structure and comparing identifying models from a representative structure. Results of their work show that stiffness identification techniques were able to identify damage caused by delamination and cracking.

3.0 MODEL DEVELOPMENT

A mathematical model of the cantilevered beam, fiber-optic sensor, and piezoelectric actuator is developed in this chapter. A modal summation technique is employed, that allows for a description of the system in terms of a finite number of allowable vibration modes. A concentrated mass, to be placed on the beam, is modeled as a delta function, acting at a single point along the beam. Mode shapes and frequencies are derived and used to develop a state space model. The model incorporates the piezoelectric actuator and the fiber-optic sensor as the input and output respectively.

3.1 BEAM DYNAMICS

3.1.1 Derivation of Mode Shapes and Natural Frequencies

The equation and boundary conditions that govern the motion of a cantilevered beam with a concentrated mass located at an arbitrary point are

given by the following [19]:

$$E_b I \frac{\partial^4 y}{\partial z^4} + [\rho A + M_c \delta(z-a)] \frac{\partial^2 y}{\partial t^2} = F(t) \quad (3.1)$$

$$y(0,t) = y'(0,t) = 0 \quad (3.2)$$

$$y''(l,t) = y'''(l,t) = 0$$

where

- M_c = concentrated mass,
- E_b = Young's modulus of the beam,
- I = area moment of inertia of the beam,
- ρ = beam density,
- A = cross sectional area,
- $y(z,t)$ = displacement at a given point and time,
- l = beam length,
- a = distance of the concentrated mass from the root, and
- $F(t)$ = input forcing function.

The cantilevered beam with concentrated mass is shown in Figure 3.1. The boundary conditions refer to the fact that there is no displacement or slope at the root of the beam, and no strain or shear forces at the tip. The quantity in brackets in (3.1) is the mass distribution and the concentrated mass is considered to be applied at a single point, $z=a$. The differential equation can be solved by the method of separation of variables. The solution must satisfy the free vibration condition so that $F(t) = 0$. The solution is assumed to have the following form,

$$y(z,t) = \psi(z)\eta(t), \quad (3.3)$$

where $\psi(z)$ and $\eta(t)$ represent the mode shapes and modal amplitudes of the

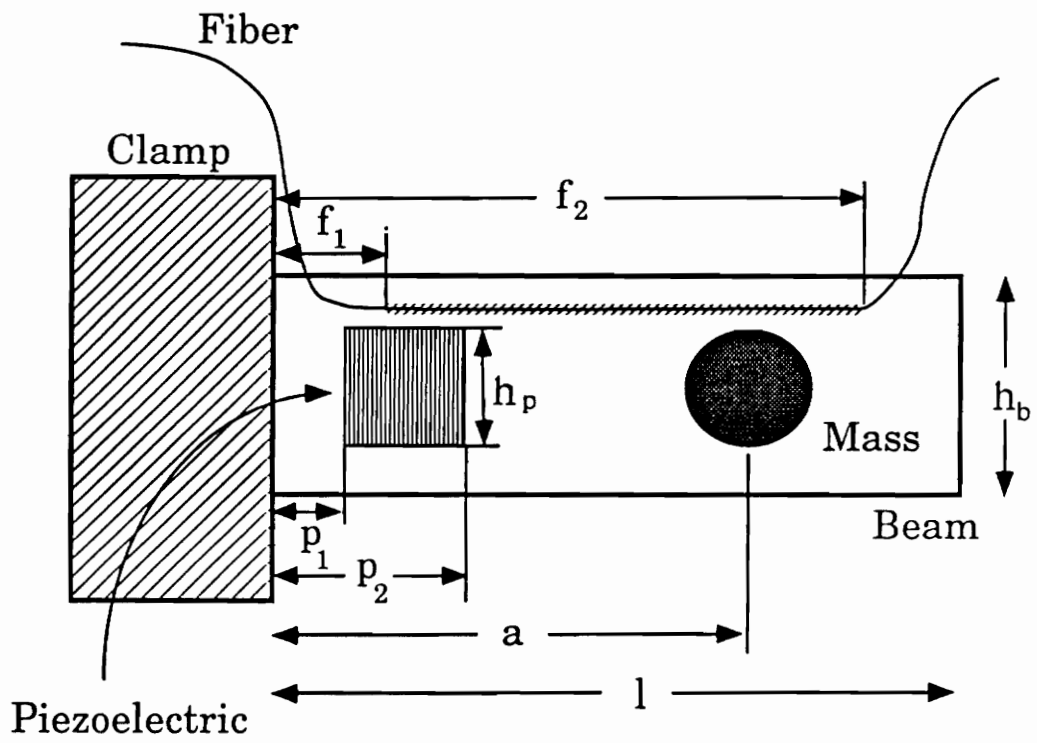


Figure 3.1 Cantilevered Beam with Fiber Sensor, Piezoelectric, and Mass [23] .

beam. Substitution of (3.3) into (3.1), with $F(t) = 0$, yields the following:

$$E_b I \psi^{iv}(z) \eta(t) + [\rho A + M_c \delta(z-a)] \psi(z) \ddot{\eta}(t) = 0. \quad (3.4)$$

If the time dependent solution is assumed to be harmonic, then $\ddot{\eta}(t) = -\omega^2 \eta(t)$ and the equation above simplifies to

$$\psi^{iv}(z) - k^4 \left[1 + \frac{M_c \delta(z-a)}{\rho A} \right] \psi(z) = 0, \quad (3.5)$$

where

$$k^4 = \frac{\omega^2 \rho A}{E_b I}. \quad (3.6)$$

Equation (3.5) can most readily be solved by using the Laplace transform and the first two boundary conditions of (3.2). The transformed equation after substitution yields

$$\Psi(s) s^4 - \Psi(s) k^4 - s \cdot \psi''(0) - \psi'''(0) - \frac{M_c k^4}{\rho A} \psi(a) e^{-as} = 0 \quad (3.7)$$

or

$$\Psi(s) = \frac{s}{s^4 - k^4} \psi''(0) + \frac{1}{s^4 - k^4} \psi'''(0) + \frac{M_c k^4}{\rho A (s^4 - k^4)} \psi(a) e^{-as} \quad (3.8)$$

where $\Psi(s)$ is the Laplace transform of $\psi(z)$. Taking the inverse Laplace transform of (3.8) gives the general solution as

$$\psi(z) = \frac{\psi''(0)}{2k^2}[\cosh(kz) - \cos(kz)] + \frac{\psi'''(0)}{2k^3}[\sinh(kz) - \sin(kz)] +$$

$$\frac{M_c k \psi(a)}{2\rho A} U(z-a) \left\{ \sinh[k(z-a)] - \sin[k(z-a)] \right\}. \quad (3.9)$$

Using the other two boundary conditions, the constants $\psi''(0)$ and $\psi'''(0)$ are found in terms of $\psi(a)$. The values become

$$\psi''(0) = \frac{M_c k^3 \psi(a) A'}{2\rho A [1 + \cosh(kl) \cdot \cos(kl)]} \quad (3.10)$$

and

$$\psi'''(0) = \frac{M_c k^4 \psi(a) B'}{2\rho A [1 + \cosh(kl) \cdot \cos(kl)]}, \quad (3.11)$$

where $b = l - a$ and A' and B' are defined to be

$$A' = [\cosh(kb) + \cos(kb)][\sinh(kl) + \sin(kl)] -$$

$$[\sinh(kb) + \sin(kb)][\cosh(kl) + \cos(kl)], \quad (3.12)$$

$$B' = [\sinh(kb) + \sin(kb)][\sinh(kl) - \sin(kl)] -$$

$$[\cosh(kb) + \cos(kb)][\cosh(kl) + \cos(kl)]. \quad (3.13)$$

Combining the equations above results in the following form for the beam mode shapes:

$$\psi(z) = \frac{M_c(kl)\psi(a)}{4M_b} \left\{ \frac{A'[\cosh(kz) - \cos(kz)] + B'[\sinh(kz) - \sin(kz)]}{[1 + \cosh(kl) \cdot \cos(kl)]} \right\} + \frac{M_c(kl)\psi(a)}{2M_b} U(z-a) \left\{ \sinh[k(z-a)] - \sin[k(z-a)] \right\}, \quad (3.14)$$

where M_b is the mass of the beam and $U(z-a)$ refers to the unit step function beginning at $z=a$.

There are an infinite number of solutions for the mode shapes in (3.14), each one corresponding to a particular eigenvalue, k . To determine the eigenvalues of this equation substitute the condition $z=a$ into (3.14). By rearranging the equation, the following form results

$$\psi(a) \left[1 - \frac{M_c(kl)}{4M_b} \left\{ \frac{A'[\cosh(ka) - \cos(ka)] + B'[\sinh(ka) - \sin(ka)]}{[1 + \cosh(kl) \cdot \cos(kl)]} \right\} \right] = 0. \quad (3.15)$$

If the trivial solution, $\psi(a) = 0$, is disregarded, then a condition exists for determining the eigenvalues associated with each mode of vibration. After substituting in the values for A' and B' and simplifying the equation, the following expression for the eigenvalues is found:

$$\frac{2M_b[1 + \cos(kl) \cdot \cosh(kl)]}{klM_c} = \left\{ [1 - \cos(ka)\cosh(ka)][\cos(kb)\sinh(kb) - \sin(kb)\cosh(kb)] \right. \\ \left. + [1 + \cos(kb)\cosh(kb)][\cosh(ka)\sin(ka) - \cos(ka)\sinh(ka)] \right\}. \quad (3.16)$$

An infinite number of eigenvalues, k , satisfy (3.16). Each eigenvalue corresponds to a spatial solution, or mode shape, of the beam. Therefore, the forced displacement of the beam at any moment in time can be considered to be a summation of the mode shapes. Mode shapes are scaled by functions that vary in time, known as modal amplitudes, $\eta(t)$. Together with the mode shapes, an equation representing the displacement of any point along the beam at any time can be expressed as

$$y(z,t) = \sum_{i=1}^{\infty} \psi_i(z)\eta_i(t). \quad (3.17)$$

For the condition of a concentrated mass placed at the end, the parameters become $a=l$ and $b=0$ and the eigenvalue criteria reduces to

$$\frac{M_c}{M_b} = \frac{1}{kl} \left[\frac{1 + \cos(kl)\cosh(kl)}{\cosh(kl)\sin(kl) - \cos(kl)\sinh(kl)} \right], \quad (3.18)$$

which corresponds exactly to the frequency equation given in [20], although arrived at by a different method.

Natural frequencies of the beam are directly related to the eigenvalues of the mode shapes. The formula for the frequencies of vibration is found from (3.6)

to be

$$\omega_n = (k_n l)^2 \sqrt{\frac{E_b I}{\rho A l^4}}. \quad (3.19)$$

In the equation above, the values of ω_n correspond to a solution of the harmonic portion of the displacement equation.

Figure 3.2 shows how the natural frequencies of the beam vary for position ($0 < a < 1$), and for the ratio of concentrated mass to beam mass ($0 < M_c/M_b < 1$). Variations are shown for the first four modes of vibration in the beam. Of particular interest is how the oscillatory behavior increases as the modes increase - especially for larger concentrated masses. These oscillations define a unique frequency “signature” for a particular mass position and quantity. Also note that there are nodes along the beam where the frequencies do not change - regardless of the amount of concentrated mass attached at the node.

3.1.2 Orthogonality Condition

After determination of the mode shapes, a representation of the entire system can be found in state space form. The key to creating this model lies in taking advantage of the orthogonality condition that exists between the mode shapes and the mass distribution, $\mu(z)$, such that [21],

$$\int_0^l \mu(z) \cdot \psi_n(z) \cdot \psi_m(z) dz = 0, \quad (n \neq m), \quad (3.20)$$

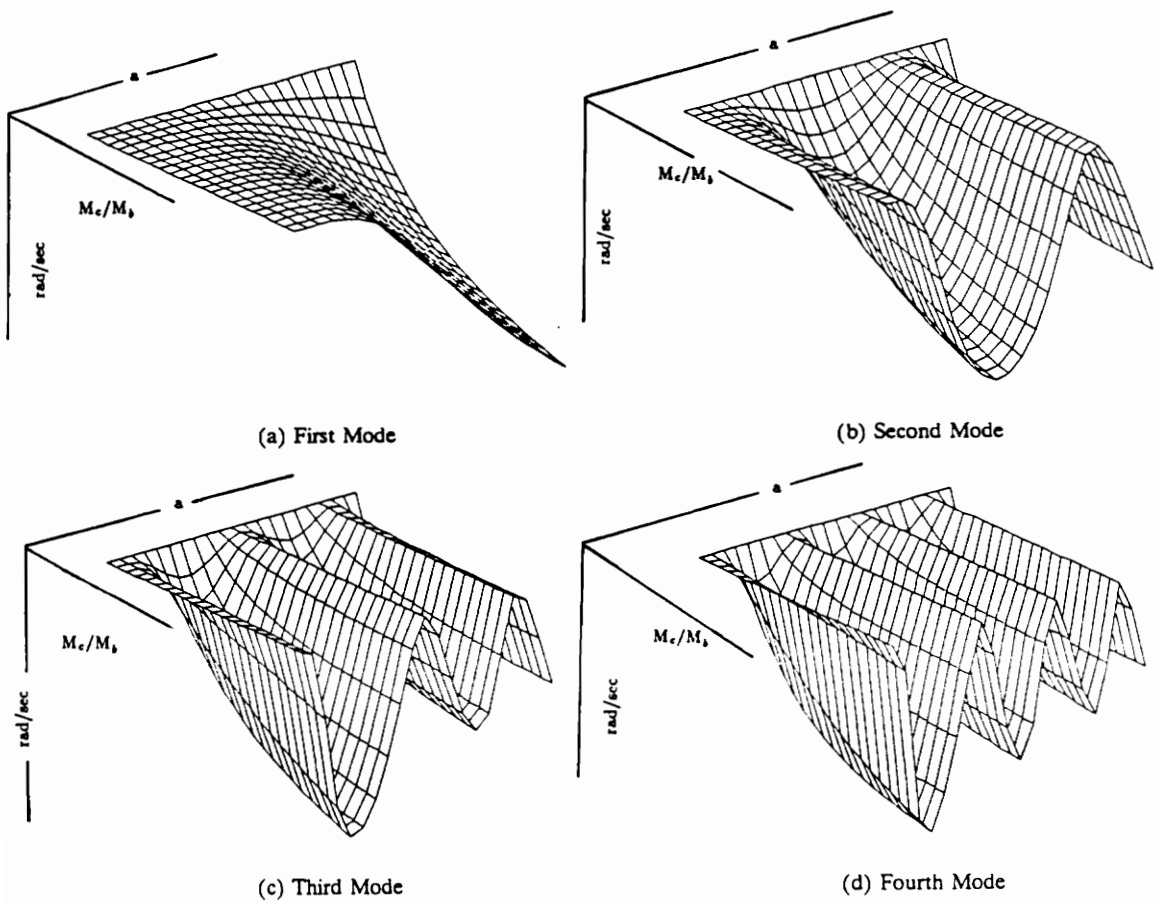


Figure 3.2 Beam Frequencies for Different Mass Loadings

where

$$\mu(z) = [\rho A + M_c \delta(z-a)]. \quad (3.21)$$

Equation (3.21) can be substituted into (3.20), resulting in

$$\rho A \int_0^l \psi_n(z) \psi_m(z) dz + M_c \psi_n(a) \psi_m(a) = 0, \quad (n \neq m). \quad (3.23)$$

If $n=m$ in (3.23) the equation is no longer zero. Instead, integration produces the normalization constants, N_n :

$$\rho A \int_0^l \psi_n^2(z) dz + M_c \psi_n^2(a) = N_n. \quad (3.24)$$

Thus, mode shapes corresponding to different modes will have different normalization constants.

The normalization constants provide a means of orthonormalizing mode shapes. The original mode shape equation (3.14) contains a term, $\psi(a)$, that is set to an arbitrary constant. Therefore, mode shapes determined from (3.14) will be scaled arbitrarily. By dividing each mode shape by the square root of its normalization constant, a set of mutually orthonormal mode shapes is produced.

In addition to the mode shapes being orthogonal with respect to the mass distribution, the 2nd derivative of the mode shapes are orthogonal with respect to the stiffness distribution of the beam. For (3.1), the strain distribution, $\sigma(z)=E_b I$, remains constant despite the addition of the concentrated mass to the beam, and the strain shapes are orthogonal. This condition is summarized as

$$\int_0^l E_b I \psi_i''(z) \psi_j''(z) dz = E_b I \delta_{ij}, \quad (3.25)$$

where it is assumed that the strain shapes, ψ_i'' have been normalized with respect to the constant stiffness, $E_b I$.

The orthogonality condition can be used to derive a set of separate differential equations corresponding to each mode. Substituting the assumed solution of (3.17) into (3.1), results in

$$E_b I \left\{ \sum_{i=1}^{\infty} \psi_i^{iv} \eta_i \right\} + \mu(z) \left\{ \sum_{i=1}^{\infty} \psi_i \dot{\eta}_i \right\} = 0. \quad (3.26)$$

Using (3.5) it follows that

$$E_b I \left\{ \sum_{i=1}^{\infty} [k_i^4 + \frac{M_c k_i^4 \delta(z-a)}{\rho A}] \psi_i \eta_i \right\} + \mu(z) \left\{ \sum_{i=1}^{\infty} \psi_i \dot{\eta}_i \right\} = 0, \quad (3.27)$$

$$E_b I \left\{ \sum_{i=1}^{\infty} [\frac{\omega_i^2 \rho A}{E_b I} + \frac{M_c \omega_i^2 \delta(z-a)}{E_b I}] \psi_i \eta_i \right\} + \mu(z) \left\{ \sum_{i=1}^{\infty} \psi_i \dot{\eta}_i \right\} = 0,$$

and

$$\sum_{i=1}^{\infty} \omega_i^2 \mu(z) \psi_i \eta_i + \sum_{i=1}^{\infty} \mu(z) \psi_i \dot{\eta}_i = 0.$$

If both sides of the preceding equation are multiplied by ψ_j and integrated over the beam length, then the orthogonality condition can be used to generate a set of independent differential equations. This set of equations can be recast in matrix form as

$$\mathbf{K} \eta(t) + \mathbf{M} \dot{\eta}(t) = 0, \quad (3.28)$$

where

$$\mathbf{M} = \begin{bmatrix} N_1 & 0 & & \\ 0 & N_2 & \ddots & \\ & \ddots & \ddots & 0 \\ & & 0 & N_N \end{bmatrix} \quad \mathbf{K} = \begin{bmatrix} \omega_1^2 N_1 & 0 & & \\ 0 & \omega_2^2 N_2 & \ddots & \\ & \ddots & \ddots & 0 \\ & & 0 & \omega_N^2 N_N \end{bmatrix} \quad (3.29)$$

The variable, N , is the number of modes that are approximated by the model. The variables $\eta(t)$ and $\dot{\eta}(t)$ can now be thought of as vectors containing the modal amplitudes and second time derivatives:

$$\eta(t) = [\eta_1(t) \quad \eta_2(t) \quad \cdots \quad \eta_N(t)]^T \quad (3.30)$$

$$\dot{\eta}(t) = [\dot{\eta}_1(t) \quad \dot{\eta}_2(t) \quad \cdots \quad \dot{\eta}_N(t)]^T \quad (3.31)$$

Because a closed form solution to (3.1) does not exist, the best that can be accomplished is to model the solution by a large number of finite terms.

3.2 FIBER OPTIC SENSOR

Fiber-optic waveguides have generated a great deal of interest in the past few years as vibration sensors because of their sensitivity and simplicity of operation. Unlike traditional vibration transducers, an optical waveguide has no moving parts and has the capability to sense information over a spatially

continuous medium, unlike an accelerometer or strain gauge that acts as a point sensor. Fiber-optic sensors also have the advantage of being relatively immune to noise problems. This section will outline the optical theory and mathematical model governing the fiber sensor as a vibration transducer.

3.2.1 Sensor Physics

A multimode optical fiber is one that allows more than one optical mode of light to propagate through the fiber. Such an optical fiber is basically an interferometer, in that the multiple modes interfere with one another as they travel through the fiber, creating a predictable interference pattern in the far-field at the output. As the fiber is strained along its longitudinal axis, three factors contribute to change the interference pattern at the output [22]. The first of these is a change in length of the fiber. The second is a reduction of the radius of the fiber due to Poisson's effect. Finally, there is a change in the index of refraction under axial strain, known as the photoelastic effect.

If the fiber is operated in dual mode (two optical modes of light propagating within the fiber), then a two lobed intensity pattern will be seen at the output of the fiber. Axial strain induced in the fiber causes the intensity of this pattern to change - due to constructive and destructive interference. As one of the lobes increases in intensity, the other will decrease, and vice versa. By monitoring a point on one of the lobes, a direct relationship between intensity and strain can be developed.

The two modes that are excited are the first linearly polarized mode

(LP₀₁), and the even second linearly polarized mode (LP₀₁^e). The intensity pattern at the output then becomes [23]

$$I(r, \phi, z) = I_1(r) + I_2(r, \phi) + I_3(r, \phi) \cos(\Gamma), \quad (3.32)$$

where $I_1(r)$ and $I_2(r, \phi)$ are the intensity contributions from the LP₀₁ and LP₀₁^e modes respectively and $I_3(r, \phi)$ is the intensity term due to interference. The term, Γ , in (3.32) represents the phase difference between the two modes. This intensity pattern, as a function of r and ϕ , is shown in Figure 3.3. If a point on one of the two lobed patterns is monitored, then r and ϕ become fixed quantities and the intensity terms all become constants in (3.32). In order to simplify the analysis, it is also assumed that the LP₀₁ mode carries as much power as the LP₀₁^e mode, and the amplitude of the interference term is equal to the sum of the individual terms. Then equation (3.32) can be rewritten as

$$I_f = \frac{I_p}{2} [1 + \cos(\Gamma)], \quad (3.33)$$

where

$$I_p/2 = I_1 + I_2 = I_3. \quad (3.34)$$

3.2.2 Measurement of Strain

As mentioned before, the term, Γ , expresses the phase difference between the modes. If the fiber is unstrained, this phase difference can be expressed by

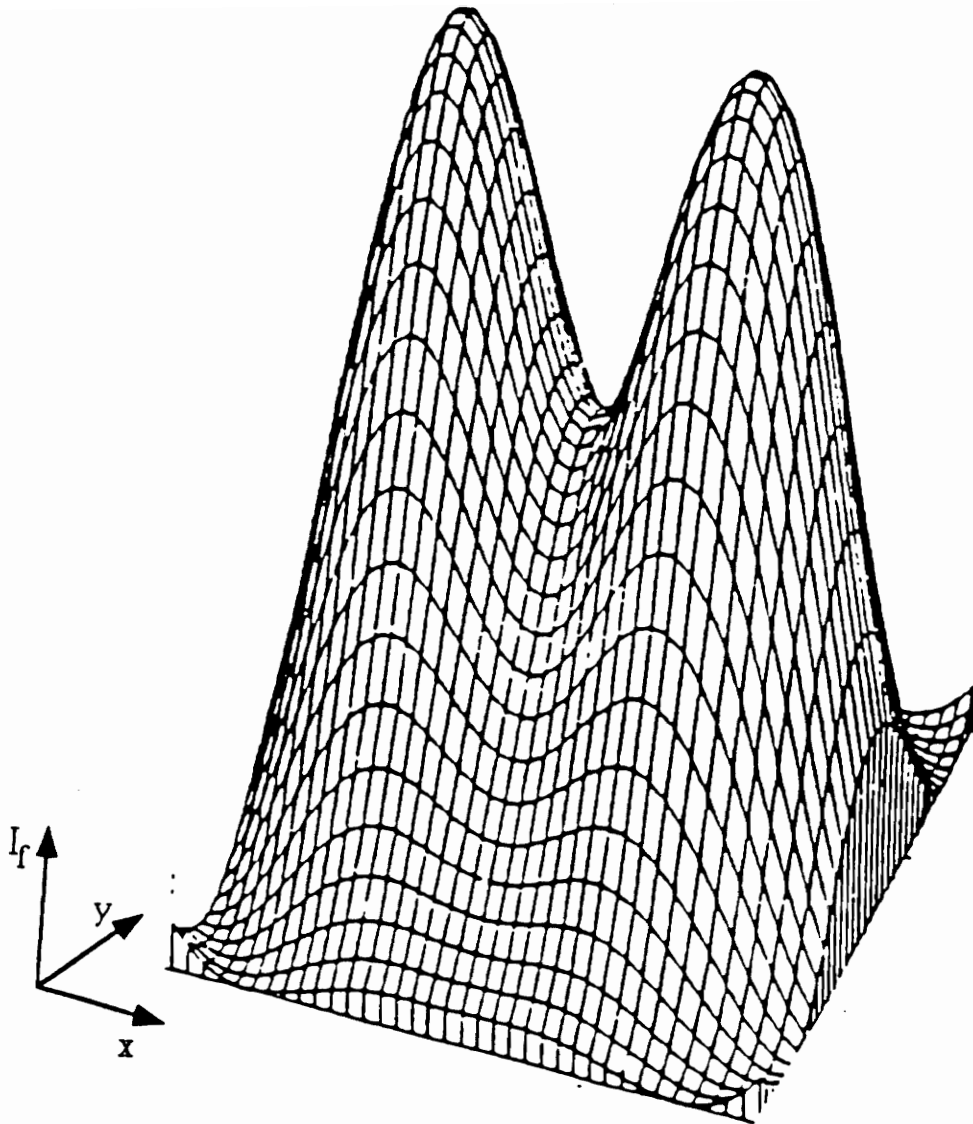


Figure 3.3 Intensity Pattern in a Dual-Mode Fiber [24].

$$\Gamma = \Delta\beta z_f + \Delta\theta_o, \quad (3.35)$$

where $\Delta\beta$ is the difference in the propagation constants between the two modes, $\Delta\theta_o$ is the initial phase difference between the two modes and z_f represents the fiber length. As the fiber undergoes axial strain, the phase difference must be rewritten as

$$\Gamma(\epsilon(z,t)) = \Delta\beta(\epsilon)z_f(\epsilon) + \Delta\theta_o \quad (3.36)$$

where $\epsilon(z,t)$ is the strain in the fiber. Therefore, the difference in the propagation constants, $\Delta\beta$, and the fiber length both become functions of the strain in the fiber. The fiber length is related to strain through the following equation:

$$z_f(\epsilon) = z_o + \int_0^{z_o} \epsilon(z,t) dz, \quad (3.37)$$

where z_o is the initial length of the fiber before undergoing strain. If the effect of strain on $\Delta\beta$ is assumed to be first order, then it can be shown that the phase difference is related to the strain by [25]

$$\Gamma_f(t) = \Delta\beta_o z_o + \Delta\tilde{\beta} \int_0^{z_o} \epsilon(z,t) dz \quad (3.38)$$

where $\Delta\beta_o$ is the initial propagation constant difference and $\Delta\tilde{\beta}$ is a constant. Substituting this expression into (3.33), yields [23]

$$I_f(t) = \frac{I_p}{2} [1 + \cos(\Delta\beta_o z_o + \Delta\tilde{\beta} \int_0^{z_o} \epsilon(z,t) dz)], \quad (3.39)$$

and a relationship exists between the strain in the fiber, and the intensity at the output. Equation (3.39) is plotted in Figure 3.4. Note that for the condition of no strain, the intensity is biased at the point, $\Gamma_o = \Delta\beta_o z_o$. This point is known as the quadrature, or Q point. If the DC term in (3.39) is removed, and the fiber is pre-strained so that the Q-point is set to zero, equation (3.39) can be re-written as

$$I_f(t) = \frac{I_p}{2} \sin(\Delta\tilde{\beta} \int_0^{z_o} \epsilon(z,t) dz) \quad (3.40)$$

For small strains induced in the beam, the intensity will remain within the linear region on either side of the Q-point, and the further simplification can be made that

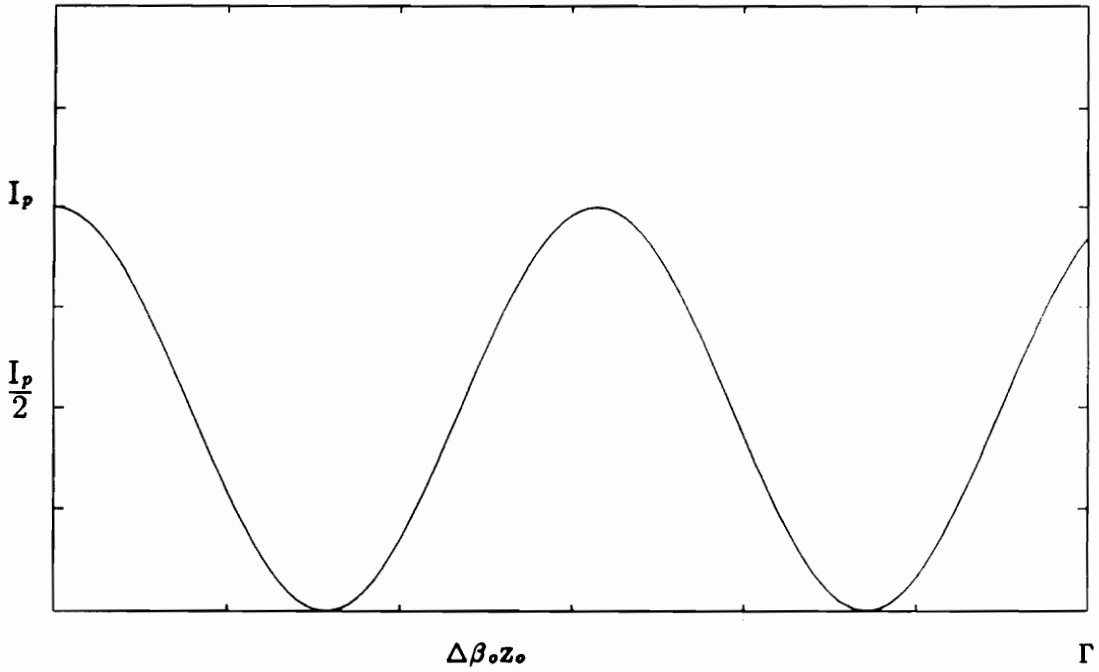
$$I_f(t) = \frac{I_p}{2} \Delta\tilde{\beta} \int_0^{z_o} \epsilon(z,t) dz . \quad (3.41)$$

If the fiber-optic waveguide is attached to the cantilevered beam, (3.41) describes how the strain in the beam is related to the intensity of light at the output (for small strain). This assumes that all of the strain in the beam is coupled into the fiber, excluding losses due to adhesion of the bonding material. The strain at any point along a rectangular beam surface at any given time is

$$\epsilon(z,t) = \frac{t_b}{2} \frac{\partial^2 y(z,t)}{\partial z^2}, \quad (3.42)$$

where t_b is the thickness of the beam, and $y(z,t)$ is the solution to the Euler-Bernoulli equation developed earlier. Substitution of (3.42) into (3.41) yields

$$I_f(t) = \frac{I_p}{2} \Delta\tilde{\beta} \int_0^{z_o} \frac{t_b}{2} \frac{\partial^2 y(z,t)}{\partial z^2} dz. \quad (3.43)$$



$$I_f(t) = \frac{I_p}{2} \left[1 + \cos \left(\Delta\beta_0 z_0 + \Delta\tilde{\beta} \int_{z_1}^{z_2} \epsilon(z,t) dz \right) \right]$$

Figure 3.4 Intensity of the Fiber Output vs. Γ

Also we can consider the sensors gage length, z_o , to be defined over two points on the beam, z_2 and z_1 . This leads to the following simplification

$$\begin{aligned}
 I_f(t) &= \frac{I_p t_b \Delta \tilde{\beta}}{4} \int_{z_1}^{z_2} \sum_{i=1}^{\infty} \psi_i''(z) \eta_i(t) dz & (3.44) \\
 &= \frac{I_p t_b \Delta \tilde{\beta}}{4} \sum_{i=1}^{\infty} \eta_i(t) \int_{z_1}^{z_2} \psi_i''(z) dz \\
 &= \frac{I_p t_b \Delta \tilde{\beta}}{4} \sum_{i=1}^{\infty} \eta_i(t) [\psi_i'(z_2) - \psi_i'(z_1)]
 \end{aligned}$$

Therefore, the intensity in the output is proportional to the derivative of the mode shape evaluated at the end points of the fiber sensor. If one end of the fiber is placed at the root of the beam, then $\psi_i'(z_1) = 0$ since the slope of the mode shape goes to zero at the root of a cantilevered beam. The fiber acts like a point sensor in this configuration - picking up information proportional to the mode shape derivative at z_2 .

3.3 PIEZOELECTRIC ACTUATOR

A piezoelectric crystal is a ceramic that changes shape when a voltage is applied across it. When bonded or embedded in a structure, such crystals have the ability to alter the shape of the structure in response to an applied voltage.

From a dynamic modeling standpoint is it desirable to know the relationship between the input voltage on the piezo and the force that it exerts on the structure while being driven. The input voltage couples a portion of its voltage to each mode of the beam. The equation that accounts for this coupling is given by [26]

$$F^i(t) = \frac{-E_b t_b^2 h_p}{l(6 + \frac{E_b t_b h_b}{E_p t_p h_p})} \cdot \frac{d_{31}}{t_p} [\psi_i'(p_2) - \psi_i'(p_1)] \cdot V(t) = \mathbf{R}^i \cdot V(t), \quad (3.45)$$

where

- p_1, p_2 - end points of the piezoelectric crystal,
- h_b - height of the beam,
- h_p - height of the piezoelectric,
- t_b - thickness of the beam,
- t_p - thickness of the piezoelectric,
- d_{31} - charge constant of piezoelectric,
- E_p - modulus of elasticity of the piezoelectric,
- $V(t)$ - voltage applied to the piezoelectric, and
- $F^i(t)$ - force imparted to the i th mode.

The piezoelectric also creates a small amount of stiffness that is added to the dynamics of the beam. Crawley and DeLuis [26] account for this added stiffness with

$$K_p^{ij} = \frac{E_b t_b^3 h_b}{2l^3(6 + \frac{E_b t_b h_b}{E_p t_p h_p})} [\psi_i''(p_2)\psi_i'(p_2) - \psi_i''(p_1)\psi_i'(p_1)] \delta_{ij}. \quad (3.46)$$

With the mathematical model of the piezoelectric actuator and the fiber optic sensor developed, we can now turn our attention to integrating the set of equations together into a state space representation of the entire dynamic system.

3.4 STATE SPACE DESCRIPTION

3.4.1 State Equations

Structural damping must be added to this system to provide a more realistic model of the beam behavior. Also, the piezoelectric creates additional stiffness that must be added. In order to incorporate these two effects, equation (3.28) is rewritten as

$$\mathbf{M} \ddot{\eta} + \mathbf{D} \dot{\eta} + (\mathbf{K} + \mathbf{K}_p) \eta = 0, \quad (3.47)$$

where \mathbf{D} reflects the amount of structural damping seen in the actual experiment, and \mathbf{K}_p is the added stiffness from the actuator given by equation (3.46).

Damping coefficients were determined by driving the beam at a particular mode, and measuring the decay time of the output. The damping factor, ζ_i , corresponding to the i th mode of vibration was determined experimentally from the exponential decay of the response. The damping matrix, \mathbf{D} , is related to the damping coefficient through

$$\mathbf{D}_{ii} = 2 \zeta_i \sqrt{\mathbf{M}_{ii} \mathbf{K}_{ii}}, \quad (3.48)$$

and the matrix \mathbf{D} , has diagonal structure. The added damping has the effect of moving the system poles off of the imaginary $j\omega$ axis and into the left-half complex plane.

Defining states of the system to be the modal amplitudes and their

derivatives such that

$$\mathbf{x} = [\eta_1 \ \eta_2 \ \cdots \ \eta_N \ \dot{\eta}_1 \ \dot{\eta}_2 \ \cdots \ \dot{\eta}_N]^T, \quad (3.49)$$

a complete set of equations can be formulated that express the relationship of the piezoelectric voltage to the output intensity of the fiber. Equations (3.44), (3.45) and (3.47) can be put into the following state space form.

$$\dot{\mathbf{x}}(t) = \begin{bmatrix} 0 & \mathbf{I} \\ -\mathbf{M}^{-1}(\mathbf{K} + \mathbf{K}_p) & -\mathbf{M}^{-1}\mathbf{D} \end{bmatrix} \mathbf{x}(t) + \begin{bmatrix} 0 \\ -\mathbf{M}^{-1}\mathbf{R} \end{bmatrix} v(t) \quad (3.50)$$

$$y(t) = \begin{bmatrix} \mathbf{C} & 0 \end{bmatrix} \mathbf{x}(t)$$

where $v(t)$ represents the input voltage across the piezo, and $y(t)$ is the output intensity of one of the two-lobed patterns.

3.4.2 Numerical Approximations

In order to develop the model described above, a number of numerical approximations were invoked to simplify the analysis. Rather than solving the characteristic equation (3.16) analytically, the equation was implemented via

computer and the eigenvalues found through a secant method iterative solution. The eigenvalues were then used to determine the mode shapes from equation (3.14). A vector of 101 points equally spaced along the beam was used to approximate each mode shape.

To uncouple the partial differential equation into a series of ordinary differential equations, the orthogonality property of the mode shapes was used. Multiplying both sides of (3.26) by the mode shapes and integrating over the beam length uncouples the equations. This was done by multiplying together each of the 101 points of the mode shape and using a Simpson's rule numerical integration routine. Accuracy of the integration can be seen from Table 3.1 which shows the normalization constants for the case of $M/M_b = 1$, and $a=1$ for a five mode model. Off-diagonal elements in this matrix should be zero due to the orthogonality with respect to the mass distribution. The numerical approximations yield off-diagonal elements that are at least 10^{-6} lower than the diagonal elements.

Table 3.1. Normalization Constants for Five Mode Model

mode	1st	2nd	3rd	4th	5th
1st	0.2279 e+0	0.0027 e-6	0.0265 e-6	0.1133 e-6	0.3293 e-6
2nd	0.0027 e-6	2.0450 e+0	0.0284 e-6	0.1191 e-6	0.3242 e-6
3rd	0.0265 e-6	0.0284 e-6	5.4196 e+0	0.1217 e-6	0.4054 e-6
4th	0.1133 e-6	0.1191 e-6	0.1217 e-6	1.0715 e+1	0.2836 e-6
5th	0.3293 e-6	0.3242 e-6	0.4054 e-6	0.2836 e-6	1.7813e+1

4.0 SYSTEM IDENTIFICATION

The system identification problem consists of trying to determine the underlying dynamics of a system from the input and output data. This is the reverse of the traditional problem in which a set of equations describing the system is available and the output to an arbitrary input is desired. Given an input, $u(n)$, and output, $y(n)$, the goal of any system identification algorithm is to determine a mathematical model relating the two. A vast number of algorithms exist that will generate a model in state space or as a transfer function. This chapter will explore the use of one such technique, the Eigensystem Realization Algorithm, in identifying a model of the cantilevered beam.

4.1 EIGENSYSTEM REALIZATION ALGORITHM

4.1.1 Description of ERA

There are many possible ways of finding minimal order realizations based

on model reduction. The technique that will be employed here is known as the Eigensystem Realization Algorithm (ERA) [27]. This algorithm is a modified version of the Ho-Kalman identification algorithm. The advantage of using this algorithm lies in the fact that it returns a state space representation that graphically displays the order of the system and provides easy determination of the natural frequencies and mode shapes. The only required data for the algorithm is a good estimation of the impulse response.

The first step in implementing the ERA is to assemble the values of the impulse response into a generalized $(r+1) \times (s+1)$ Hankel matrix as follows:

$$H_{r,s}(k-1) = \begin{bmatrix} h(k) & h(k+1) & \dots & h(k+r) \\ h(k+1) & h(k+2) & \dots & h(k+r+1) \\ \vdots & \vdots & \ddots & \vdots \\ h(k+s) & h(k+s+1) & \dots & h(k+r+s) \end{bmatrix} \quad (4.1)$$

Each of the $h(k)$ impulse values consist of a $(p \times m)$ block where p is the number of outputs from the system, and m is the number of inputs. The variables r and s are such that the dimensions of the Hankel matrix, $H_{r,s}(k-1)$, are $(s+1) \cdot p \times (r+1) \cdot m$. If the number of independent rows and columns of this matrix are each larger than the order of the system, then the Hankel matrix above has rank equal to the order of the system [27].

Initial dimensions of the Hankel matrix, $H(k)$, are important in the

identification process. There are two constraints on the dimensions of this matrix in the ERA algorithm. If the matrix is chosen as too large, the singular value decomposition can become computationally intensive. If the matrix is too small (but still larger than the order of the system), then there may not be enough information to identify the lower modes of the system. Enough of the response measurement must be provided such that the lowest mode is discernable by the algorithm. This means that the sampling time becomes a concern. Obviously, one needs to sample at a rate at least twice the highest frequency in the system, although the rate must be slow enough so that a great number of points are not needed to see the lowest mode of the response.

The Hankel matrix can also be written in the following form:

$$H_{r,s}(k) = V_r A^k W_s, \quad (4.2)$$

where V_r and W_s are the observability and controllability matrices, respectively,

$$V_r = \begin{bmatrix} C & CA & CA^2 & \dots & CA^r \end{bmatrix}^T, \quad (4.3)$$

and

$$W_s = \begin{bmatrix} B & AB & A^2B & \dots & A^{s-1}B \end{bmatrix}. \quad (4.4)$$

The matrices A , B , and C form the state space description of the system.

The first step in the process is to perform a singular value decomposition on $H_{r,s}(0)$, which leads to the following equation:

$$H_{rs}(0) = P D Q^T = \begin{bmatrix} P_d & P_e \end{bmatrix} \begin{bmatrix} D_d & 0 \\ 0 & 0 \end{bmatrix} \begin{bmatrix} Q_d^T \\ Q_e^T \end{bmatrix} = P_d D_d Q_d^T, \quad (4.5)$$

and

$$P_d^T P_d = Q_d^T Q_d = I_d. \quad (4.6)$$

Equation (4.5) can be rearranged as follows:

$$H_{rs}(0) Q_d D_d^{-1} P_d^T = I_d. \quad (4.7)$$

The matrix, D_d , refers to the submatrix containing the non-zero singular values of $H_{rs}(0)$. The number of non-zero singular values contained in D_d is equal to the order of the system [27] and can be used to find a minimum realization. Two additional matrices are defined for convenience as:

$$E_p^T = \begin{bmatrix} I_p & \Theta_p & \cdots & \Theta_p \end{bmatrix} \quad (4.8)$$

$$E_m = \begin{bmatrix} I_m & \Theta_m & \cdots & \Theta_m \end{bmatrix}^T \quad (4.9)$$

where I and Θ are identity and null matrices respectively, of order p and m . Dimensions of the matrices above are established such that the following equation holds:

$$h(k) = E_p^T H_{rs}(k) E_m. \quad (4.10)$$

If the system is single input, single output (SISO), $p = m = 1$, and the identity and null matrices in (4.8) and (4.9) reduce to dimension one.

Equation (4.10) can be expanded to find a minimal state space realization in the following way:

$$\begin{aligned}
 h(k) &= E_p^T H_{rs}(k) E_m & (4.11) \\
 &= E_p^T [V_r A^k W_s] E_m \\
 &= E_p^T H_{rs}(0) [Q_d D_d^{-1} P_d^T] V_r A^k W_s [Q_d D_d^{-1} P_d^T] H_{rs}(0) E_m \\
 &= E_p^T H_{rs}(0) Q_d D_d^{-1/2} [D_d^{-1/2} P_d^T H_{rs}(1) Q_d D_d^{-1/2}]^k D_d^{-1/2} P_d^T H_{rs}(0) E_m \\
 &= E_p^T P_d D_d^{1/2} [D_d^{-1/2} P_d^T H_{rs}(1) Q_d D_d^{-1/2}]^k D_d^{1/2} Q_d^T E_m
 \end{aligned}$$

For an arbitrary set of state space equations, the impulse response, $h(k)$, can be expressed in the following form:

$$h(k) = \tilde{C} \cdot \tilde{A}^k \cdot \tilde{B}, \quad (4.12)$$

where

$$\tilde{C} = E_p^T P_d D_d^{1/2}, \quad (4.13)$$

$$\tilde{B} = D_d^{1/2} Q_d^T E_m, \quad (4.14)$$

and

$$\tilde{A} = D_d^{-1/2} P_d^T H_{rs}(1) Q_d D_d^{-1/2}, \quad (4.15)$$

from the equations above. The corresponding state space representation is:

$$\tilde{\mathbf{x}}(k+1) = \tilde{\mathbf{A}} \tilde{\mathbf{x}}(k) + \tilde{\mathbf{B}} \mathbf{u}(k) \quad (4.16)$$

$$\mathbf{y}(k) = \tilde{\mathbf{C}} \tilde{\mathbf{x}}(k).$$

which is a minimal order system. This state space representation can be further simplified by calculating the eigenvalues and eigenvectors of the matrix $\tilde{\mathbf{A}}$. Eigenvalues and eigenvectors are determined by use of the following equation:

$$\tilde{\mathbf{A}} \Phi = \mathbf{Z} \Phi \quad (4.17)$$

where \mathbf{Z} is a matrix containing the eigenvalues along the diagonal and Φ is a matrix of corresponding eigenvectors. If a change of states is made through use of the following equation

$$\tilde{\mathbf{x}} = \Phi \hat{\mathbf{x}} \quad (4.18)$$

then (4.18) can be used to transfer the identified state space into modal coordinates.

$$\hat{\mathbf{x}}(k+1) = \mathbf{Z} \hat{\mathbf{x}}(k) + [\Phi^{-1} \mathbf{D}_d^{1/2} \mathbf{Q}_d^T \mathbf{E}_m] \mathbf{u}(k) \quad (4.19)$$

$$\mathbf{y}(k) = [\mathbf{E}_p^T \mathbf{P}_d \mathbf{D}_d^{1/2} \Phi] \hat{\mathbf{x}}(k)$$

The matrix $[\Phi^{-1} \mathbf{D}_d^{1/2} \mathbf{Q}_d^T \mathbf{E}_m]$ is known as the initial modal amplitude matrix and $[\mathbf{E}_p^T \mathbf{P}_d \mathbf{D}_d^{1/2} \Phi]$ is known as the mode shape matrix. Modal damping rates and damped natural frequencies are the real and imaginary parts of the eigenvalues

(along the main diagonal of Z) after transformation into the s domain.

The columns of $\tilde{C}\Phi$, should be thought of as mode shapes only as long as the output being measured is displacement. If the outputs of the system are proportional to the strain (as the case for a strain gauge) then the values in the $\tilde{C}\Phi$ matrix will be proportional to the second derivative of the mode shape. The more discrete sensors that are used, the more points appear in $\tilde{C}\Phi$, and the better the interpolation of the strain function.

If the system under consideration is underdamped with complex eigenvalues, then the identified values in the $\tilde{C}\Phi$ matrix will occur in complex conjugate pairs. A normalized mode shape can be found from these values through a method given in [28]. For an identified system, the matrix $\tilde{C}\Phi$ looks like

$$\tilde{C}\psi = \begin{bmatrix} a_{11}+jb_{11} & a_{11}-jb_{11} & \cdots & a_{1n}+jb_{1n} & a_{1n}-jb_{1n} \\ \vdots & \vdots & \vdots & \vdots & \vdots \\ a_{p1}+jb_{p1} & a_{p1}-jb_{p1} & \cdots & a_{pn}+jb_{pn} & a_{pn}-jb_{pn} \end{bmatrix} \quad (4.20)$$

where there are p rows corresponding to the p sensors and $2n$ columns equal to twice the number of modes. Each pair of complex conjugate columns can be combined into one real mode shape, and then normalized with the first value being unity [28]. The displacement of the i th sensor from the first point of the vector is given by $\sqrt{a_i^2+b_i^2}$, and its motion lags that of the first sensor by $\tan^{-1}(b_i/a_i)$. Again, if strain gauges are used, the “mode shapes” will actually be strain shapes.

Natural frequencies of the system can be determined directly from the

discrete eigenvalues that appear along the main diagonal of Z . The eigenvalues are first transformed from the z to the s domain through the relationship

$$s = [\ln(z) \pm 2\pi ij] / \Delta\tau \quad (4.21)$$

where

$$\begin{aligned} i &= \sqrt{-1} \\ \Delta\tau &= \text{sampling interval} \\ j &= \text{an integer} \end{aligned}$$

The natural frequencies are then just the magnitude of the continuous eigenvalues. For lightly damped structures, the poles will be very close to the $j\omega$ axis and the imaginary component will approximate the natural frequencies.

4.1.2 Modal Amplitude Coherence

The easiest way of determining how well the identified model approximates the theoretical model is to compare the eigenvalues and frequencies of both (if known). However, there exist a number of other correlation methods that can quantify the degree to which the identified system represents the actual one. The one described here is known as the Modal Amplitude Coherence (MAC) [29].

Modal Amplitude Coherence is defined as the coherence between the modal amplitude history and an ideal one formed by extrapolating the initial value of the history to latter points using the identified eigenvalue [29]. The identified modal amplitudes can be rewritten as

$$\psi^{-1}\tilde{\mathbf{B}} = [b_1, b_2, \dots, b_n]^*, \quad (4.22)$$

where $*$ denotes complex conjugate transpose. Next, a sequence is formed as

$$\bar{q}_j^* = [b_j^*, \exp(t_1 \Delta \tau s_j) b_j^*, \dots, \exp(t_{s-1} \Delta \tau s_j) b_j^*], \quad (4.23)$$

where s_j is a system eigenvalue (in the continuous domain), and $t_i \Delta \tau$ represents the sampled time. Now, form the matrix

$$\psi^{-1} D^{1/2} Q^T = [q_1, q_2, \dots, q_n]^*. \quad (4.24)$$

The coherence parameter for the j th mode can now be expressed as

$$\gamma_j = |\bar{q}_j^* q_j| / (|\bar{q}_j^* \bar{q}_j| |q_j^* q_j|)^{1/2}. \quad (4.25)$$

The coherence parameter provides a way of measuring how well the system mode was identified. Values of the coherence parameter can vary between 0 and 1. As $\gamma_j \rightarrow 1$ the identified eigenvalue and the true eigenvalue are very close. As $\gamma_j \rightarrow 0$, the identified mode corresponds to noise in the system.

4.2 IDENTIFICATION FROM SIMULATION

4.2.1 Effect of Noise on Identification

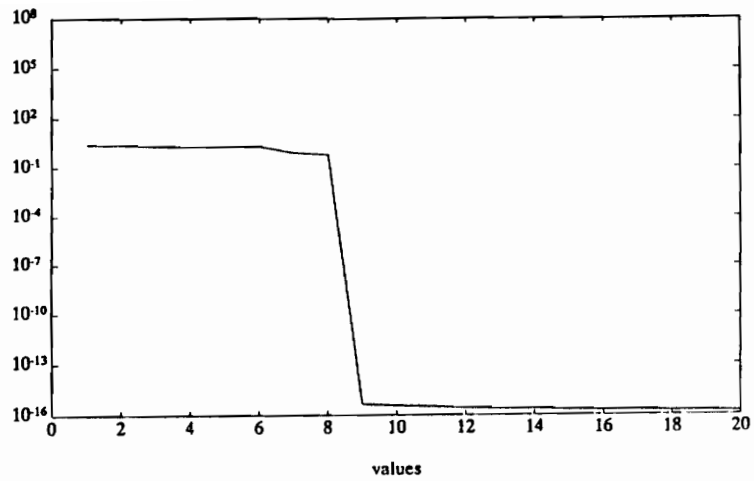
A number of identification checks were performed on the simulated model developed in Chapter 3 by generating input and output data and by developing a

state space description of the system. Modal amplitude coherence was used to quantify the accuracy of the identified model.

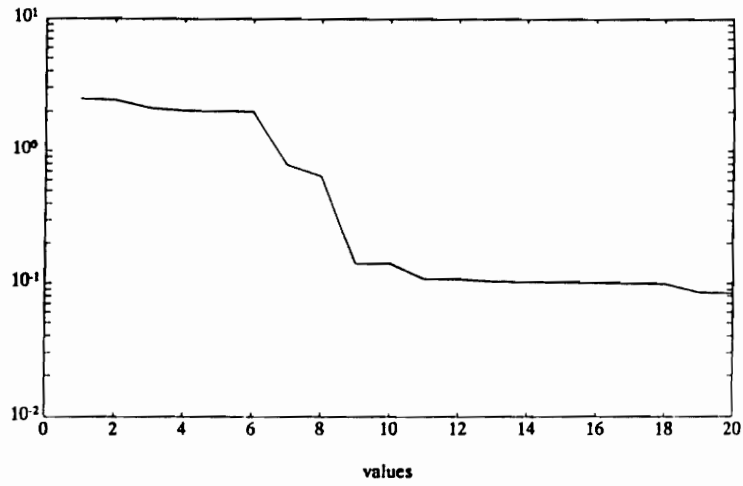
Figure 4.1 shows the first twenty singular values that were determined by the ERA for a model with no concentrated mass on the beam. The simulated model contained four modes, corresponding to an 8th order system. Theoretically, there should be eight singular values determined from the decomposition of the Hankel matrix. Figure 4.1a shows the singular values determined without noise. As can be seen from the graph, the singular values are essentially zero after the 8th, excluding round-off error.

Figure 4.1b shows the effect on the singular values if a small amount of measurement noise is added. The added noise was zero mean and wideband in nature and resulted in a signal-to-noise ratio of 36 dB. As can be seen from the graph, the effect is to smooth the distinction between the zero and nonzero values. A jump in the graph is still evident, but has become much less pronounced than in Figure 4.1a. If more noise is added to the output, as in Figure 4.1c, it becomes difficult to discern the order of the system. Noise in the last graph was created such that the signal-to-noise ratio dropped to 17 dB.

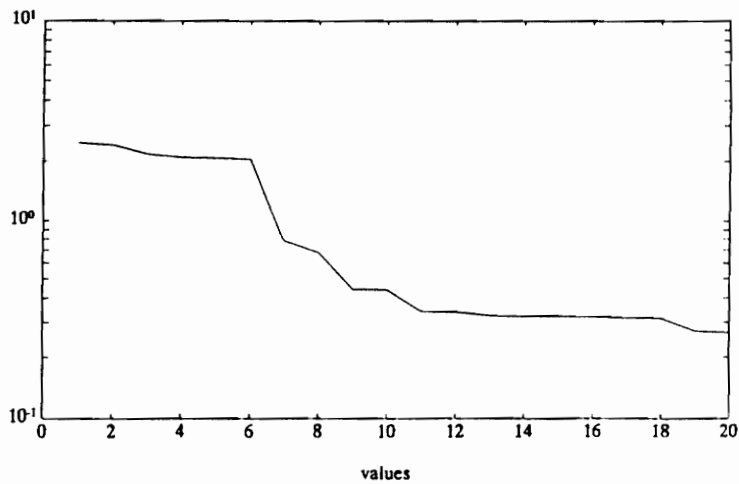
The MAC was applied to the three identified cases of additive noise above. Results of the analysis are shown in Table 4.1. A four mode simulated model was used, and the effect of retaining 16 singular values was investigated. For the case with no noise, the left column shows that the four identified modes are actual system modes. The middle column shows some degradation of the coherence measures and the last column shows even worse degradation, as would be expected.



(a). No noise



(b). S/N = 36 dB



(c). S/N = 17 dB

Figure 4.1 Singular Values for Varying Levels of Measurement Noise

Table 4.1 MAC Values for Various Levels of Measurement Noise

mode	no noise	S/N = 36 dB	S/N = 17 dB
1st	1.0000	0.9987	0.9993
2nd	1.0000	1.0000	0.9998
3rd	1.0000	1.0000	0.9997
4th	1.0000	1.0000	0.9999
5th	-	0.8093	0.7609
6th	-	0.8237	0.7145
7th	-	0.8519	0.8629
8th	-	0.4320	0.4896

4.3 IMPULSE RESPONSE ESTIMATION

The discrete impulse response, $h(n)$, is related to the input, $u(n)$, and the output, $y(n)$ of a system through the following:

$$y(n) = \sum_{k=0}^{\infty} h(k)u(n-k) \quad (4.26)$$

Since the ERA relies on the impulse response of the system, it must be estimated from input/output data. This section will explore ways in which the impulse response can be extracted from input/output data.

4.3.1 Deconvolution

Equation (4.26) can be rewritten in matrix form as [30]

$$\begin{bmatrix} y(0) \\ y(1) \\ \vdots \\ y(n) \end{bmatrix} = \begin{bmatrix} h(0) & 0 & & & \\ h(1) & h(0) & \ddots & & \\ \vdots & \ddots & \ddots & 0 & \\ h(n) & \dots & h(1) & h(0) & \end{bmatrix} \begin{bmatrix} u(0) \\ u(1) \\ \vdots \\ u(n) \end{bmatrix} \quad (4.27)$$

Since the system of equations is in lower triangular form, the values of $h(k)$ can be solved for recursively. The first few terms in the iteration are

$$h(0) = y(0)/u(0), \quad (4.28)$$

$$h(1) = [y(1) - h(0)u(1)]/u(0),$$

and
$$h(2) = [y(2) - h(1)u(1) - h(0)u(2)]/u(0).$$

In general,

$$h(k) = [y(k) - \sum_{i=1}^k h(k-i)u(i)]/u(0).$$

Theoretically, the impulse response can be recovered exactly by the recursive solution of (4.28). However, if the impulse response is lengthy, successive values of the solution are subject to greater and greater round-off errors. If the system is subjected to noise as well, then the recovery of the impulse response becomes more difficult. In structures that are lightly damped and have impulse responses that decay over long periods, this type of algorithm does not perform well.

4.3.2 Empirical Transfer Function Estimate

If equation (4.26) is transformed into the z domain, the z transform of the output is related to the input and impulse response by the following [31]:

$$Y(z) = H(z) \cdot U(z). \quad (4.29)$$

This relationship provides a way of estimating the discrete transfer function, $H(z)$, given a set of sampled input and output data. With the condition that $z=e^{-j\omega\Delta\tau}$ ($\Delta\tau$ - sampling interval) the input and output values can be transformed using a Fast Fourier Transform (FFT) and ratios formed [31]:

$$H_i(k) = \frac{Y_i(k)}{U_i(k)} \quad \text{and} \quad H_{N-i}(k) = H_i^*(k) \quad \text{for} \quad \{ 0 \leq i \leq N/2, U_i(k) \neq 0 \} \quad (4.30)$$

where N is the number of sampled data points. Once $H(k)$ has been determined, one can find the impulse response by performing an inverse FFT on $H(k)$. This process of forming ratios of the transformed input and output is known as the Empirical Transfer Function Estimate (ETF E) [31]. Values of $H(e^{-j\omega\Delta\tau})$ up to $N/2$ are all that are required since the complex conjugates of these fill out the rest of the sequence, insuring that the impulse response will be real. If the impulse response of the system is finite (which is never the case in a real system), then the ETF E can determine the impulse response exactly. This is a great advantage over deconvolution, because the length of the input and output are not limited. The only factor in determining how well the impulse is estimated is to what degree the response can be considered to be finite. A heavily damped system would be easier to estimate than a lightly damped one, given the same input/output data lengths.

If a lightly damped system is driven over a short period of time and a large amount of output data is taken, then the estimate of the impulse response will improve. As the input is shortened further, it will begin to approximate an impulse to the system, and the output will resemble the impulse response of the

system. An alternative to using the ETFE would be to drive the system with a narrow pulse and use the output as an estimated impulse response.

4.3.3 Pulse Response

By using a pulse of sufficiently small width as an input to a system, the output is an estimate of the impulse response. The narrower the pulse width, the closer the pulse will approximate a theoretical impulse into the system. However, if the pulse is too narrow, it will not be able to drive the lower modes of the system. By lengthening the pulse width, more energy is coupled into the lower modes, but the input will no longer resemble an impulse. Therefore, a trade-off between these two extremes must be maintained for good impulse estimation.

A pulse width that is n times larger than the sampling time, $\Delta\tau$, is given by $\Delta w = n\Delta\tau$. If the pulse has height, h , then the output must be scaled by $1/(n \cdot h)$, before it is used as an impulse response estimate. In addition, the pulse width of the input will cause a slight phase shift between the pulse response and the true impulse response of the system.

4.4 IDENTIFICATION FROM EXPERIMENT

4.4.1 Description of Experiment

The fiber optic sensor described in Chapter 3 was fixed to a cantilevered

beam and used to sense the vibrations of the beam as it was driven by a piezoelectric actuator. A diagram of the experiment is shown in Figure 4.2. Three separate sections of the fiber make up the path from the laser to the photodiode at the output. The first section, from the laser to the cantilevered beam, is composed of single mode elliptical core fiber that allows one optical mode to propagate. As only one mode travels through this section, it insures that any disturbances to this section of the fiber will not show up as induced strain at the output. This first section is fused to the sensing section of the fiber, which is elliptical core fiber that operates in dual mode (two optical waves propagate through the fiber). At the end of the beam an offset splice is made to a single mode circular core fiber that monitors one of the two lobed intensity patterns from the dual mode fiber. Again, use of a single mode fiber as the lead-out, insures that any disturbances from the beam to the photodetector will not interfere with the strain measurement from the beam.

A pair of piezoelectric actuators, placed on either side of the beam, provided the necessary excitation to the beam. The pair operate out of phase - as one expands, the other contracts, inducing a bending moment at the root of the beam. Because of restrictions on the amount of voltage that could be applied to each actuator, the maximum voltages used were ± 100 Volts peak-to-peak. Voltages to each of the piezoelectrics were provided by a digital computer and D/A board. Sets of input/output data were stored, for processing off-line.

Table 4.2 lists the parameters of the beam, actuator, and fiber that were used in the experiment. A more complete description of the hardware is given in reference [23].

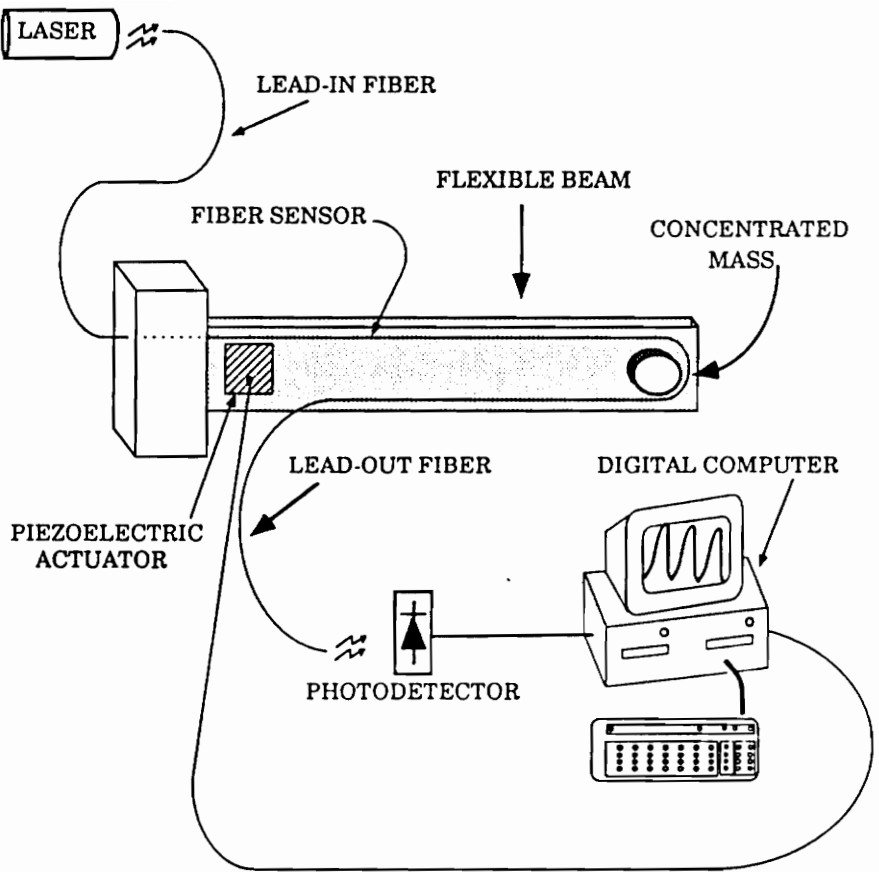


Figure 4.2 Experimental Set-up [23]

Table 4.2 Experimental Beam, Piezoelectric, and Fiber Parameters

Beam	
modulus of elasticity, E_b	200 GPa [32]
moment of inertia, I	$1.84 \times 10^{-12} \text{ m}^4$
height, h_b	0.05 m
length, l	0.6144 m
density, ρ	7860 g/m^3 [32]
mass, M_b	0.184 kg
thickness, t_b	0.74 mm
damping constants, ζ_i	0.0026 - 1st mode 0.0018 - 2nd mode 0.0016 - 3rd mode 0.0013 - 4th mode
Piezoelectric	
modulus of elasticity, E_p	630 GPa
charge constant, d_{31}	$0.166 \text{ } \mu\text{m/kV}$
end locations, p_1, p_2	0.012, 0.050 m*
height, h_p	0.038 m
thickness, t_p	$190 \text{ } \mu\text{m}$
Fiber	
fiber end locations, f_1, f_2	0.0, 0.566 m*

* as measured from the root of the beam

4.4.2 Experimental Noise

In many experimental situations measurements are averaged to reduce the effects of noise. However, the effects of noise upon the fiber-optic sensor were so small that averaging did not produce any significant changes in the data. To illustrate this point, the signal characteristics of an averaged set of data were compared to the characteristics of one data set. Measurements chosen were system responses to a pulse input with no concentrated mass attached to the beam.

Figure 4.3 shows plots of the response to a pulse of nine different trials. The plots all display the same relative shape; the only discernable difference is the DC offset. With the DC component removed by subtracting out the mean value of each signal, better agreement is obtained.

The spectrum of the nine averaged signals was compared to that of one of the signals, with no discernable difference. Peaks in the frequency spectra due to the vibrational modes of the system are well above the noise floor of the sensor. Figure 4.4a shows an FFT of one data set. Figure 4.4b is an FFT showing the effect of averaging the nine data sets. Figure 4.4c is an FFT of the noise level in the fiber. The two strong peaks in the lower portion of the last plot are the first two vibration modes of the beam. Even with the beam at rest, the fiber recorded ambient vibrations caused by air currents, etc. The 60 Hz “mode” appears due to the frequency of the AC power line that drives the digital computer and acquisition process.

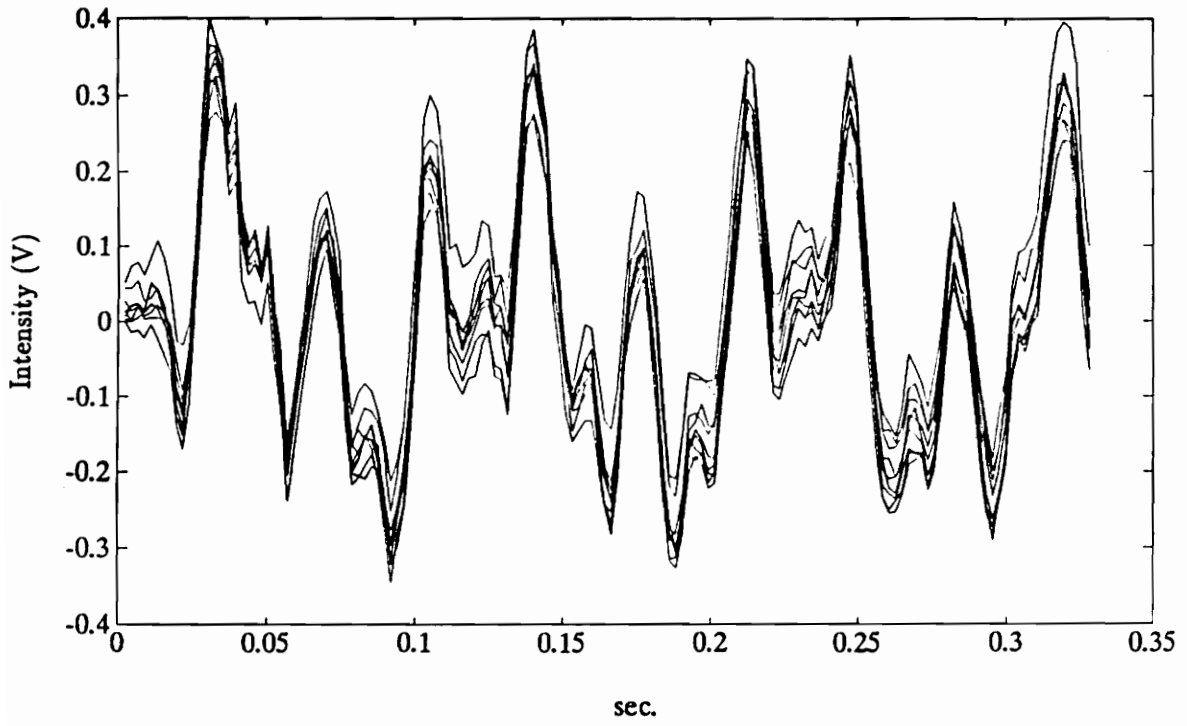
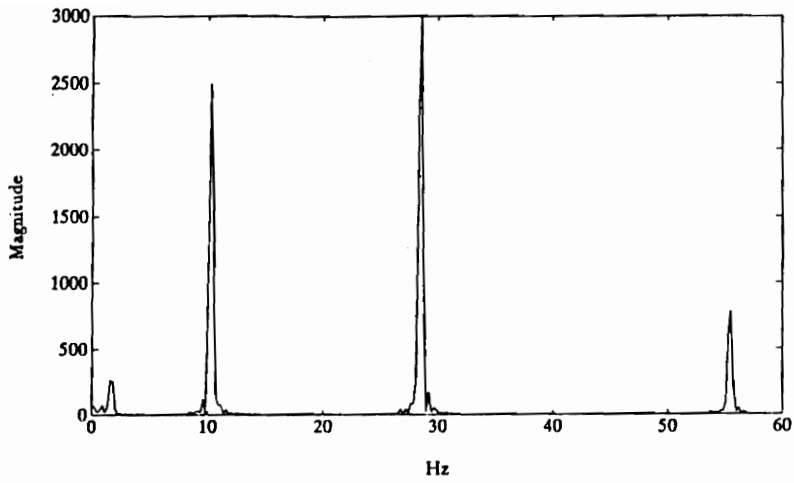
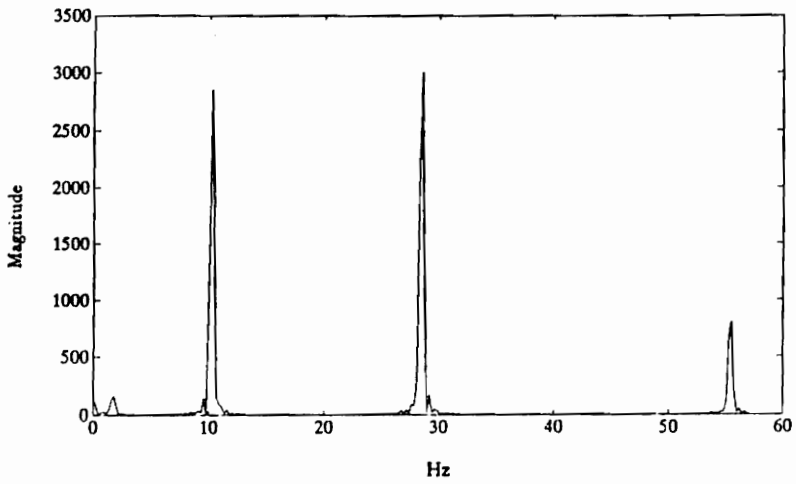


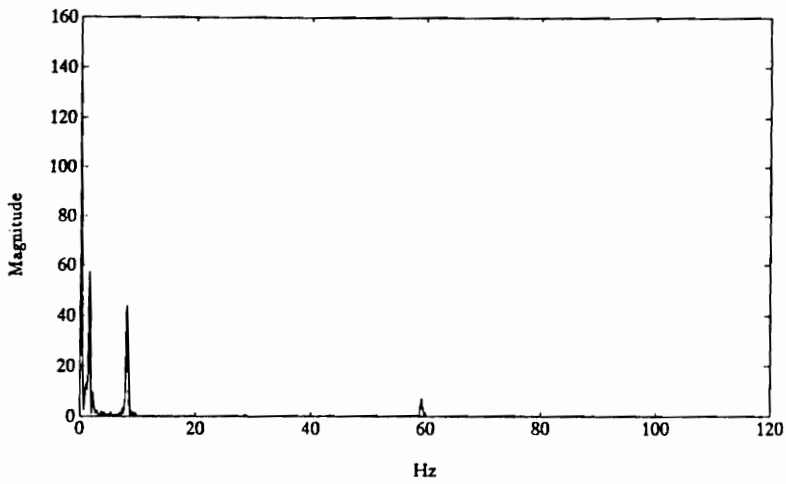
Figure 4.3 Nine Measured Responses to a Pulse Input



(a). FFT of unaveraged response



(b). FFT of averaged responses



(c). FFT of measurement noise (no input)

Figure 4.4 Spectrum of Unaveraged, Averaged, and Noise Responses

4.4.3 ETFE vs. Pulse Approximation

Two methods of impulse estimation discussed previously were applied to the cantilevered beam experiment. Both the ETFE and pulse approximation techniques were used with the ERA to identify a model that was compared to theory. The results of both techniques are presented below.

The first method used a narrow pulse to approximate an impulse to the system. A pulse of height +50 V and width 0.0088 sec. (4 sampling intervals) was applied to the piezoelectric actuator and the response was recorded. The responses were scaled appropriately by a factor of 200 (50 V * 4 sampling intervals). Using the ERA, eight of the singular values were seen to dominate, indicating that the system contained four strong modes. Continuous eigenvalues and MAC values of this identified model are shown in the far left column of Table 4.3.

The second method utilized the ETFE to estimate the impulse response. A variable square wave drove the system for approximately 0.5 seconds and 3 seconds of output data were measured. The impulse response estimate was used by the ERA to identify a model of the system. The middle column of Table 4.3 shows the eigenvalues and MAC values for the ETFE estimation. The final column shows the the eigenvalues and MAC values from the simulated model.

A comparison between the two methods and the simulated results show that both impulse response estimation techniques performed well. The only noticeable differences occur in the highest mode between the identified eigenvalues and the ones from simulation. The real part of all the eigenvalues is identified as negative, insuring that the system is stable. In addition, the real part is much

Table 4.3 Eigenvalues and MAC Values: ETFE vs. Pulse Input

	Pulse Input	ETFE	Simulation
mode	Eigenvalues		
1st	$-0.207 \pm 10.038j$	$-0.131 \pm 10.607j$	$-0.030 \pm 10.553j$
2nd	$-0.022 \pm 64.737j$	$-0.047 \pm 64.647j$	$-0.110 \pm 65.415j$
3rd	$-0.092 \pm 178.952j$	$-0.431 \pm 180.283j$	$-0.296 \pm 181.765j$
4th	$-0.178 \pm 348.332j$	$-0.281 \pm 347.872j$	$-0.458 \pm 354.203j$
mode	MAC values		
1st	0.9717	0.9988	1.0000
2nd	1.0000	0.9996	1.0000
3rd	0.9994	0.9782	1.0000
4th	0.9974	0.9842	1.0000

smaller in magnitude than the complex part. This is not surprising considering the small amount of damping in the beam. MAC values for both techniques are all close to unity, indicating that the identified eigenvalues represent the system modes.

Despite both methods performing well, several factors favor the pulse approximation technique. The response can be fed directly into the ERA (after scaling). Additional processing need not be done as in the case for the ETFE. Also, the ETFE can produce erroneous results if not enough output data is taken. As long as the shape of the pulse input satisfy the conditions of excitation and impulse approximation, good identification will be achieved with the pulse approximation technique.

4.4.4 Identification and Model Comparison

The pulse approximation method and ERA were applied to the cantilevered beam and the identified model compared to the simulated one. A number of criteria were used to compare experiment to simulation. These including looking at the responses of each model to the same inputs, and comparing the identified frequencies to the theoretical ones.

To validate the model, a 100 V peak-to-peak variable frequency square wave was applied to the piezoelectric actuator and the response of the beam was measured using the fiber-optic sensor. The square wave guaranteed wide band excitation and insured that beam would be displaced significantly from rest. In addition, this same variable frequency square wave was used as an input to the

simulated model of the beam developed previously. The resulting outputs are plotted together in Figure 4.5. As can be seen from the graph, the responses are almost identical, indicating that the model and experiment agree extremely well under conditions of no concentrated mass. The model in this case contained only the lowest four modes of vibration, which implies little contribution of the higher modes in the experiment.

As was seen in Table 4.3, the identified and simulated natural frequencies are comparable. The light damping in the system, is shown by the relatively small real parts of the eigenvalues compared to the imaginary components. Therefore, the natural frequencies of the system are approximated by the complex part of the eigenvalues.

Another comparison between the identification and the simulation consisted of an analysis of the Bode plot of each. Figure 4.6 shows the identified and the simulated Bode plots for the cantilevered beam. Again, since the system is underdamped, the resonant frequencies of the system show up as peaks in the plot at the appropriate frequency. The simulated and identified plots show the same resonant frequencies, and roughly the same shape except for small variations in slope.

Finally, the identification itself was tested by looking at the response of the identified model. The same +50 V pulse was used to drive the identified model, and the response recorded. Figure 4.7 shows the original beam response and the response to the identified system. Both responses agree very closely, except for an apparent phase shift. This phase difference is caused by the pulse width of the input used to generate the impulse response estimate. If the two responses are time shifted by the amount of the pulse width, there is better agreement.

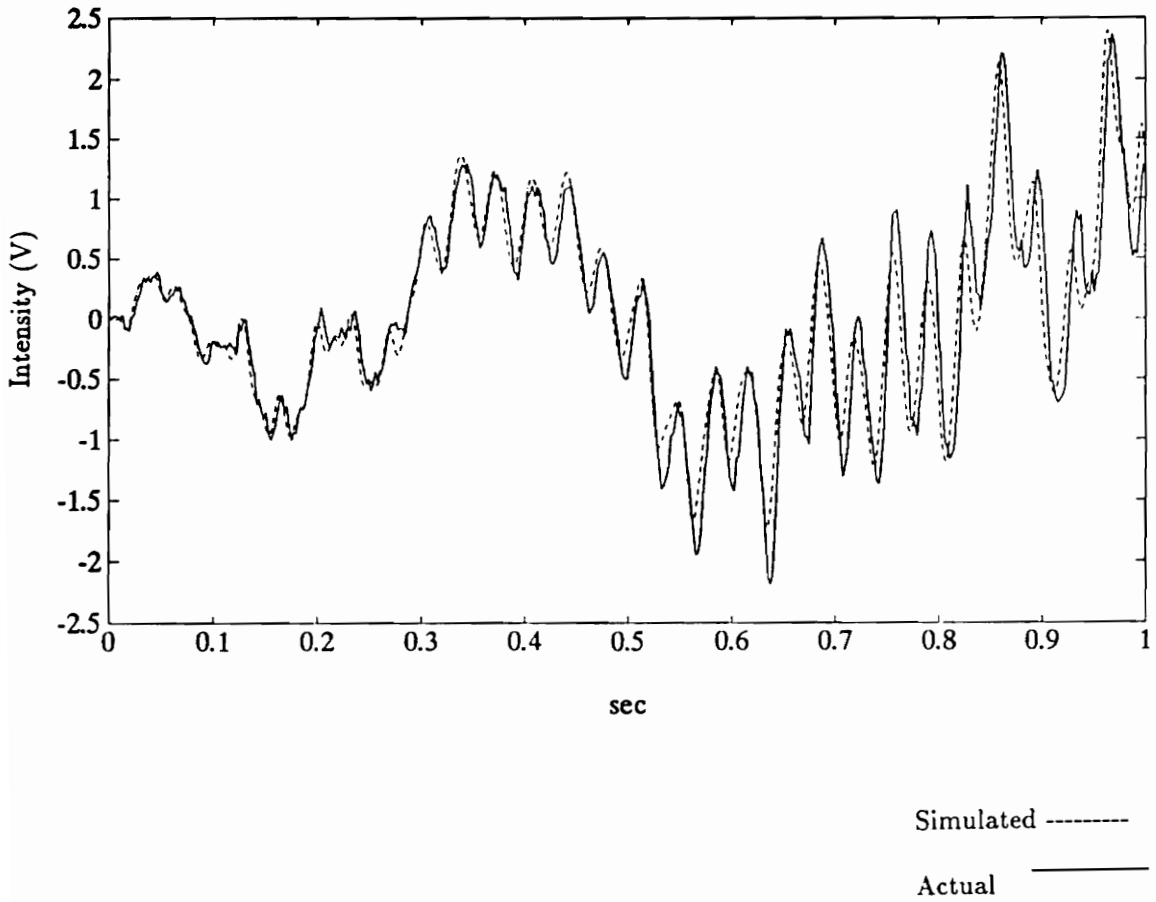


Figure 4.5 Actual and Simulated Beam Responses

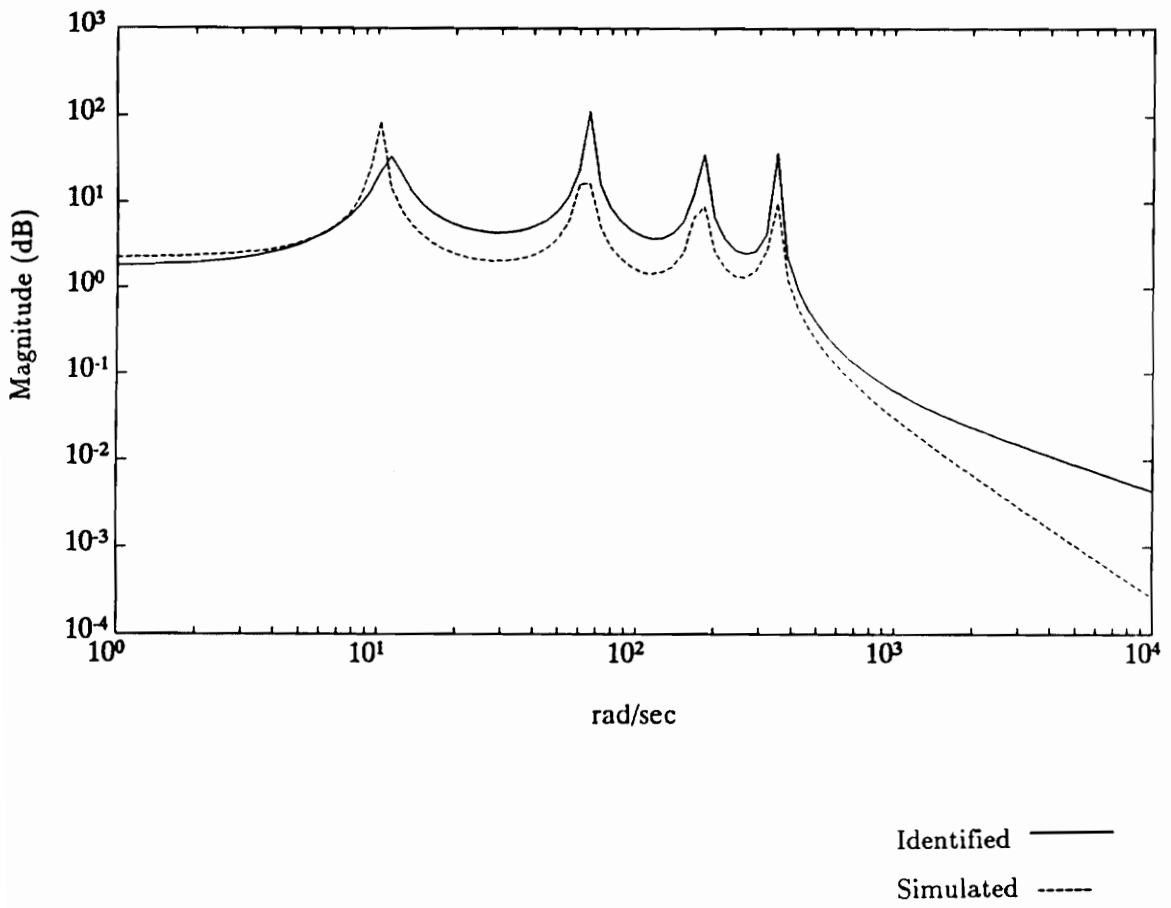


Figure 4.6 Bode Plot of Simulated and Identified Systems

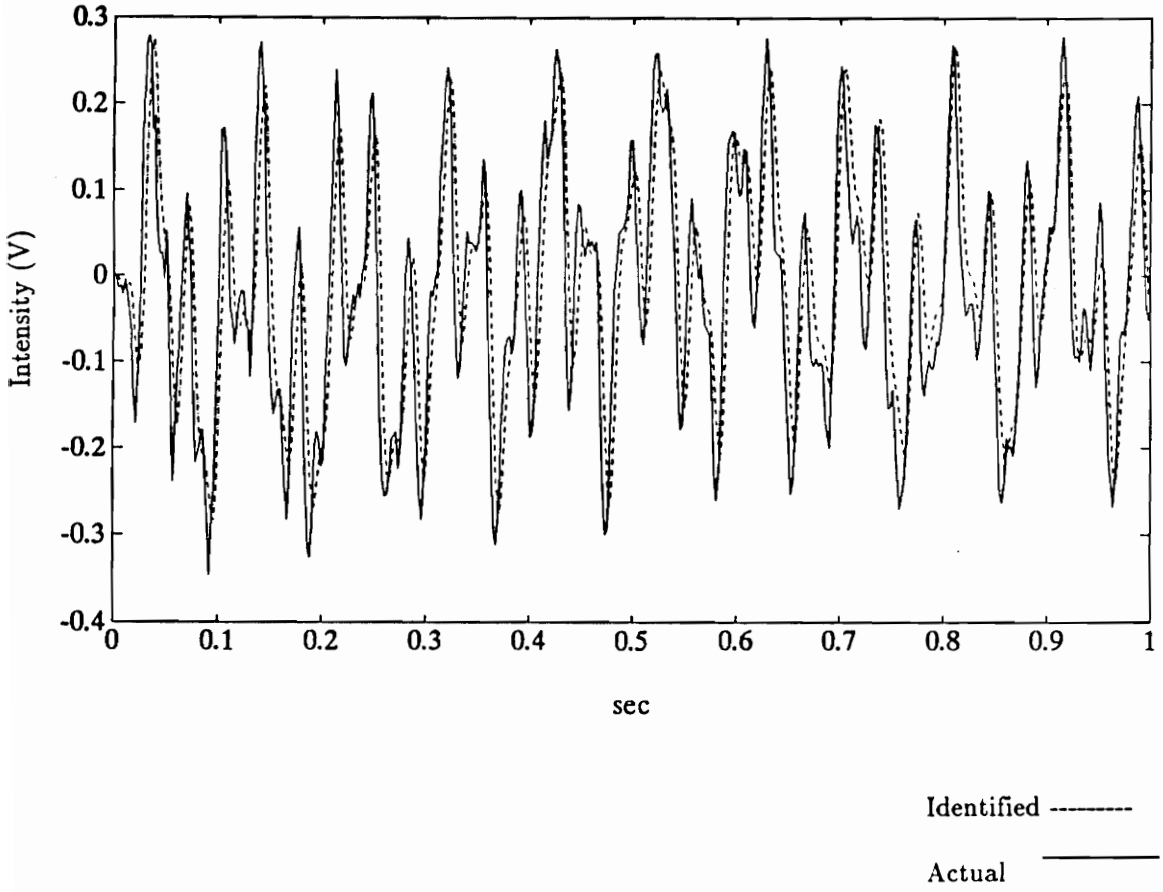


Figure 4.7 Responses to Actual and Identified Systems

5.0 MASS IDENTIFICATION

A concentrated mass is attached to the cantilevered beam described in the previous chapter and the identification techniques applied to the system. The frequencies under a variety of concentrated mass placements are determined and compared to the theoretical values derived in Chapter 3. The problem of determining the mass amount and location from the identified system model is investigated. Both simulated and experimental results are presented.

5.1 MODEL LIMITATIONS

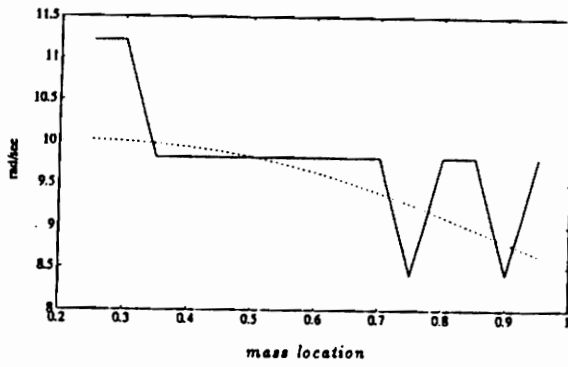
In order to compare the simulated model with the actual experiment, two performance criteria were considered. Identified frequencies of the beam were compared to those predicted by theory for a variety of concentrated mass conditions. Also, responses of the simulated model were compared to the actual beam responses. The model shows good agreement with smaller concentrated masses, but departs from theory with larger and larger masses. This is a result of the underlying assumptions in the model development.

5.1.1 Frequency Comparison for Different Mass Locations

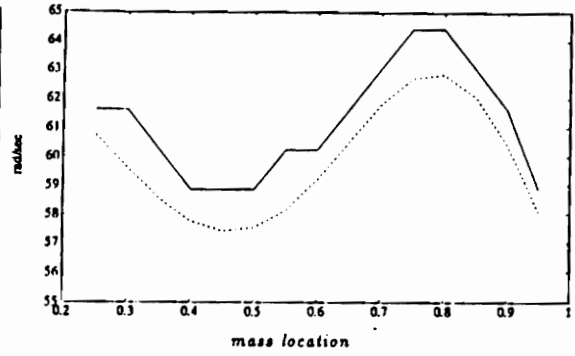
To compare theoretical and experimental frequencies, three different masses were moved along the beam, one at a time, from the free end toward the root. The frequencies of vibration were determined. An impulse was applied to the piezoelectric and an FFT of the recorded response was analyzed. By looking at the location of the amplitude peaks of the FFT, an estimate of the natural frequencies was found. Figures 5.1, 5.2 and 5.3 show the first four natural frequencies of vibration along with plots of the theoretical frequencies. Each individual plot corresponds to frequency variations in one mode of the system. By referring to the 3-D plots in Figure 3.1, the current plots are seen to be cross sections taken at the appropriate mass-to-beam ratio.

Figure 5.1 corresponds to the case of a mass-to-beam ratio of $M_c/M_b = 0.10$. The four plots show excellent agreement between experiment and theory - especially in the higher modes of the system. In Figure 5.2, the mass-to-beam ratio has been increased to $M_c/M_b = 0.33$. The lower two modes show good agreement, but the higher two modes from the experiment are shifted significantly downward. However, it should be noted that these modes do retain the same relative shape seen in the theoretical model. Figure 5.3 shows frequency variations for a mass-to-beam ratio of $M_c/M_b = 0.65$. Again, there is relative agreement for the lower two modes, but the 3rd and 4th mode depart radically from theory, both in size and in shape.

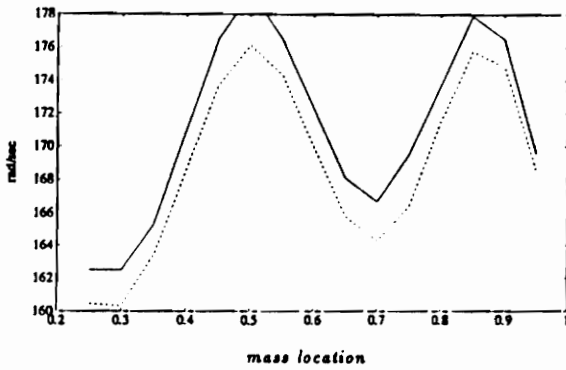
The most plausible explanation for the discrepancies between simulation and experiment is the limitations on the original Euler-Bernoulli equation. This equation does not include a term for the rotary inertia of the beam, which



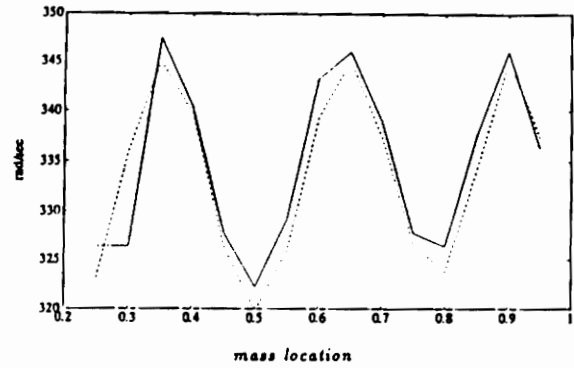
(a) First Mode



(b) Second Mode



(c) Third Mode

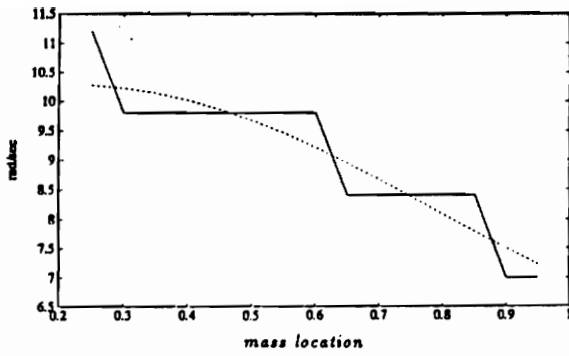


(d) Fourth Mode

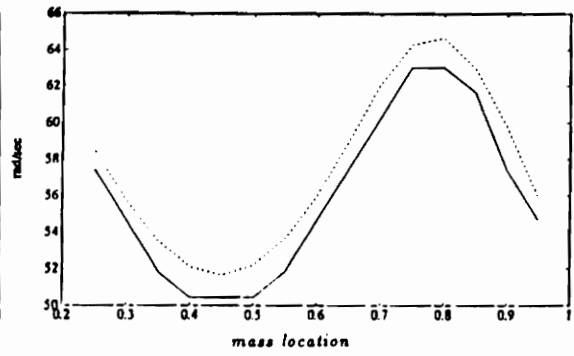
Theoretical -----

Actual —————

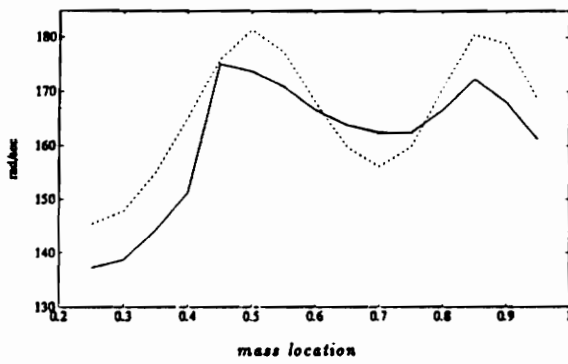
Figure 5.1 Identified and Theoretical Frequencies - $M_c/M_b = 0.10$



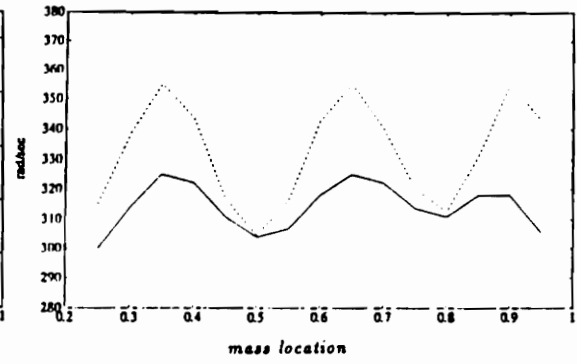
(a) First Mode



(b) Second Mode



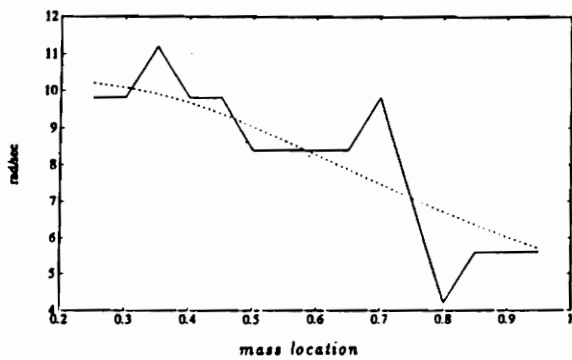
(c) Third Mode



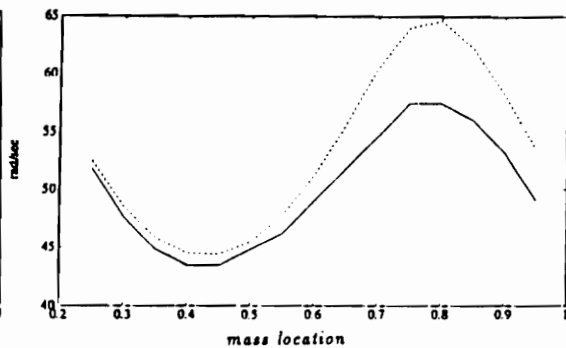
(d) Fourth Mode

Theoretical ———
 Actual ———

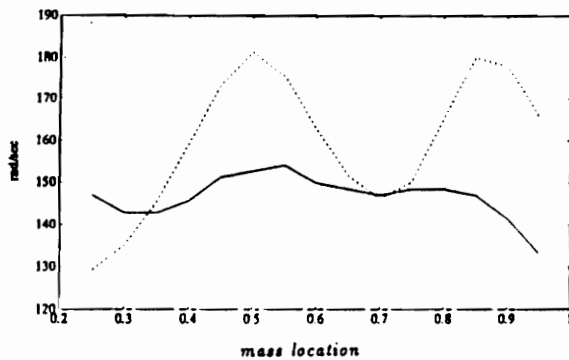
Figure 5.2 Identified and Theoretical Frequencies - $M_c/M_b = 0.33$



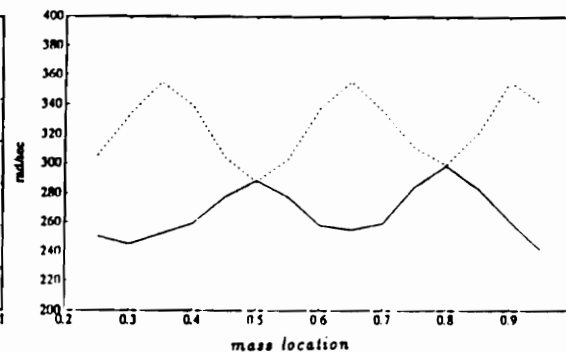
(a) First Mode



(b) Second Mode



(c) Third Mode



(d) Fourth Mode

Theoretical -----
 Actual —————

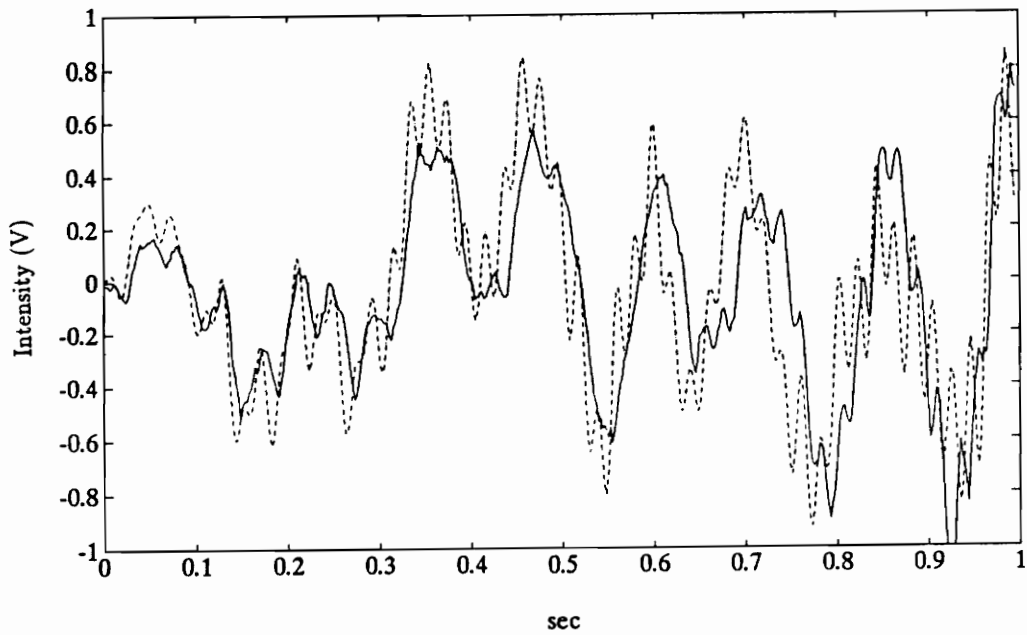
Figure 5.3 Identified and Theoretical Frequencies - $M_c/M_b = 0.65$

becomes considerable with increasing concentrated mass.

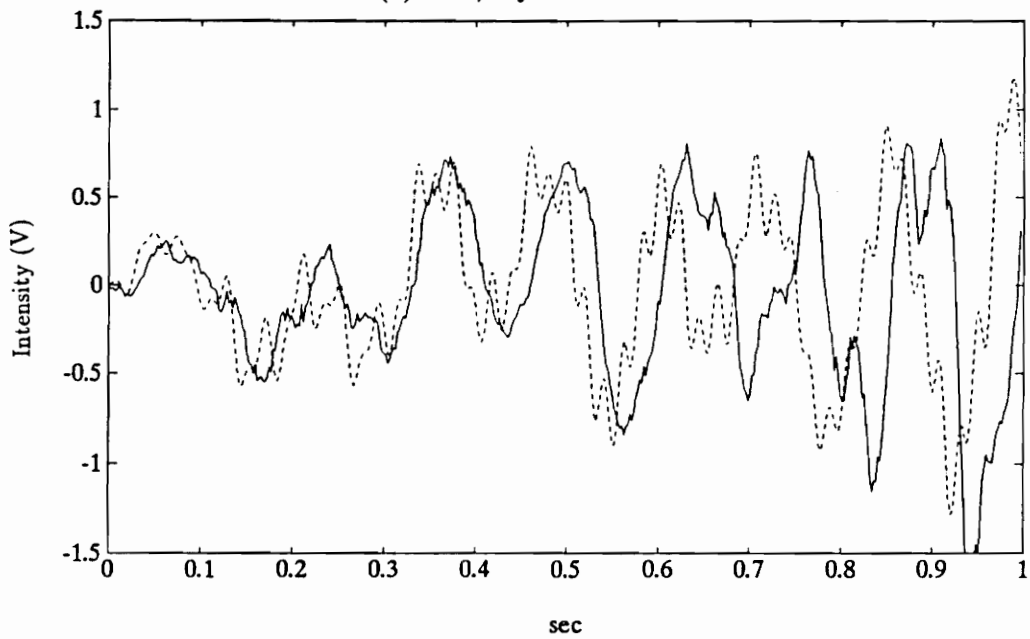
The discrepancies in the 1st mode of all the plots are largely due to the resolution of the FFT done on the response data. Two seconds of response data was measured, using a sampling interval of 0.0022 seconds. This corresponds to about 914 points of output data. Each response was zero padded out to 2048 points to increase the resolution of the frequency information. This limited the frequency resolution to $1/(N \cdot \Delta\tau) = 0.2230$ Hz. Changes smaller than this within the first mode were not detectable, which explains why the plot is not smooth.

5.1.2 Response Comparison

A variable frequency square wave of peak-to-peak value 100V was used as an input to the experiment and the response recorded. Figure 5.4 shows the response of the theoretical model and of the experiment for two different mass conditions. A four mode model was used to produce the simulated response in each case. Figure 5.4a compared responses for a smaller end mass ($M_c/M_b = 0.3261$, $a=1$), and Figure 5.4b for the larger end mass ($M_c/M_b = 0.6446$, $a=1$). As can be seen from the plots, as the mass-to-beam ratio increases, agreement between model and experiment grows worse. The response of the smaller mass shows the same general characteristics as the simulated response, but is worse than the simulated response of the beam with no mass (Figure 4.5). These plots again confirm that the model works well for lower concentrated masses, but fails as larger masses are used.



(a). $M_c/M_b = 0.33, a=1.0$.



(b). $M_c/M_b = 0.65, a=1.0$

Simulated -----
 Actual —————

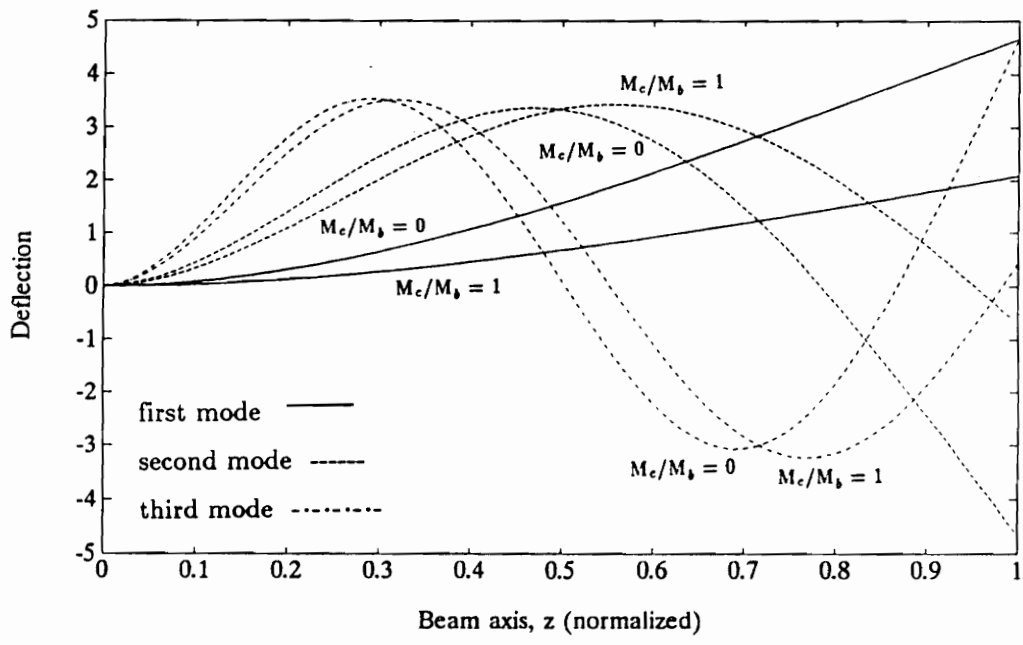
Figure 5.4 Simulated and Actual Responses for Varying Mass Loads

5.2 IDENTIFIED SYSTEMS

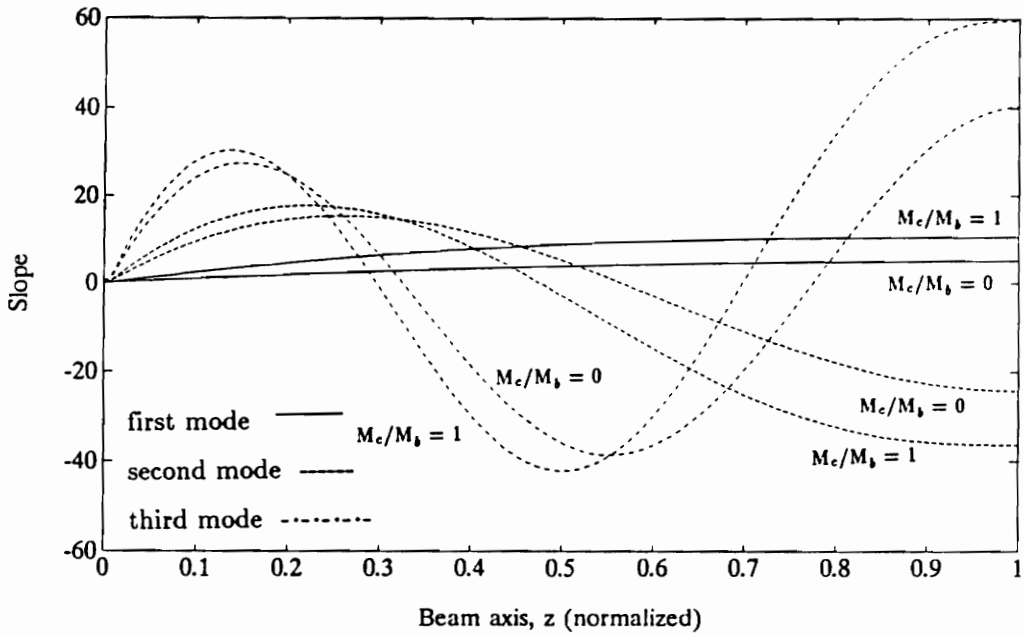
5.2.1 Sensor Placement

As mentioned previously, the fiber sensor in the present configuration behaves as a point sensor whose output is proportional to the derivative of the mode shape evaluated at the ends of the fiber. Thus, the same placement issues that plague point sensors must be considered when using the fiber sensor. Because the output of the sensor is a summation of contributions from different modes, care must be taken to insure that the fiber is placed in such a way as to register information from all of the system modes. If the fiber end happens to lie along a node of one of the mode shape derivatives, information from that mode will not show up in the output, and the system will be misidentified. This situation is compounded in cases where the parameters of the system are undergoing changes. A fiber placement that correctly identifies one configuration may not identify another. Figure 5.5 shows how the mode shapes and their derivatives change by adding a mass to the end of the beam. The nodes of the derivative are seen to move along the length of the beam in 5.5b, as the concentrated mass changes location and/or amount.

Figure 5.6a shows a Bode plot of the four mode theoretical model previously developed. The conditions on the beam are such that there is no concentrated mass, and the end of the fiber was simulated to be at $z=0.84$ of the normalized beam length ($l=1$). All four underdamped modes of vibration are clearly visible in the plot. A concentrated mass equal to the mass of the beam was simulated at the end of the beam, and the identification procedure repeated.

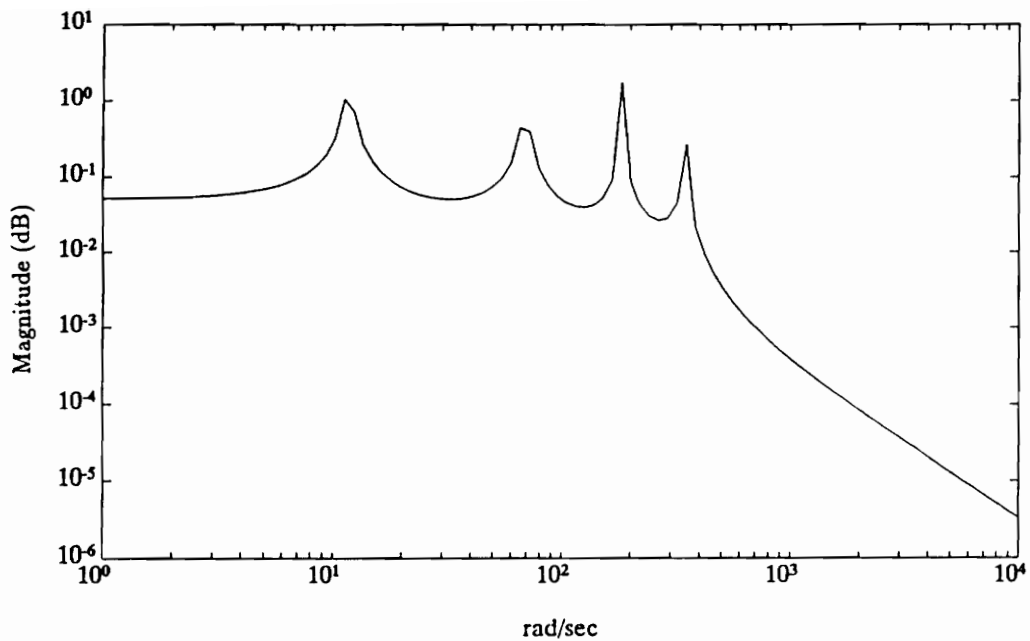


(a). Mode Shapes for $M_c/M_b = 0,1$; $a=1$.

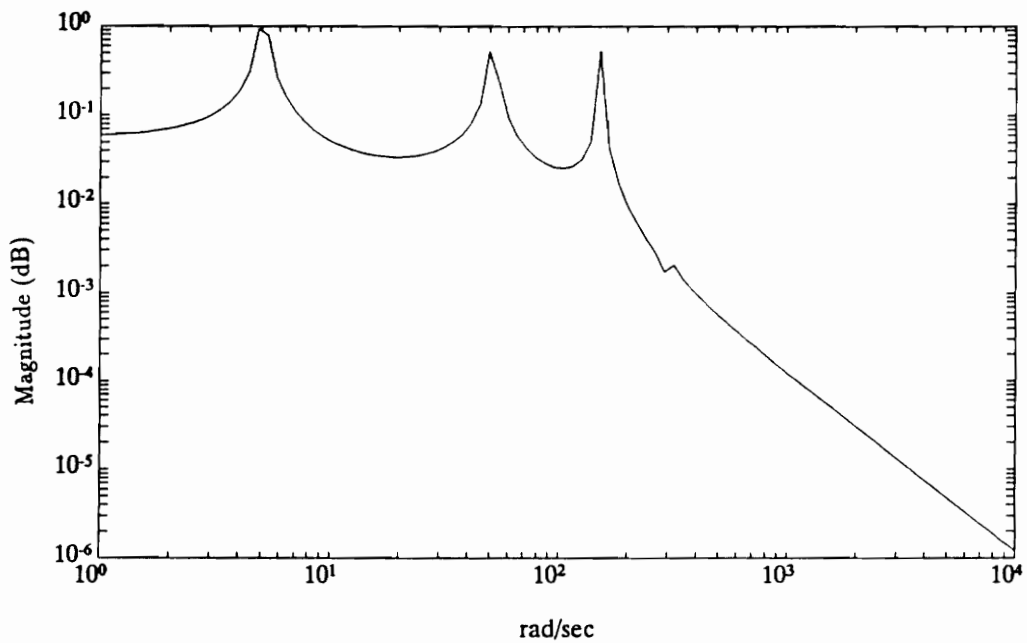


(b). Mode Shape Derivatives for $M_c/M_b = 0,1$; $a=1$.

Figure 5.5 Mode Shapes and Derivatives for Varying Mass Loads



(a). $M_c/M_b = 0$



(b). $M_c/M_b = 1, a=1.$

Figure 5.6 Inaccurate Identification due to Poor Sensor Placement

Figure 5.6b shows the Bode plot of the re-identified system. It is clear from this plot that the fourth mode of the system was missed, due to the fact that the mode shape derivative for this concentrated mass placement has a node near the end of the fiber.

5.2.2 Frequency Comparison

Outputs from the input pulses were recorded and used to identify various concentrated mass configurations. As in the previous chapter, the outputs were scaled appropriately, and fed into the ERA and a system model identified. Eigenvalues and MAC values for the three concentrated mass cases are shown in Table 5.1. As in the case with no concentrated mass, the complex part of the identified eigenvalues is much larger than the real part, indicating that the natural frequencies are approximated by the complex part of the eigenvalues.

The identified frequencies from the ERA show the same discrepancies with theory that were seen in the FFT plots shown earlier. However, the identified frequencies do compare well with the frequencies seen in the previous FFT plots. This is shown in Table 5.2, where a comparison is made between frequencies identified from the ERA, from FFT analysis and from theory. These results indicate that the identification is correct and the model fails for large attached masses.

Table 5.1 Eigenvalues and MAC Values for Varying Mass Loads

	$M_c/M_b = .106$ a= 0.25	$M_c/M_b = .326$ a= 0.80	$M_c/M_b = .645$ a= 0.50
mode	Eigenvalues		
1st	-0.114±10.727j	-0.404±6.289j	0.160±8.112j
2nd	-0.029±62.330j	-0.104±63.310j	-0.029±44.579j
3rd	-0.084±162.038j	-0.203±166.511j	-0.446±153.538j
4th	-0.134±326.674j	-0.492±310.674j	-0.181±288.953j
mode	MAC values		
1st	0.9985	0.9070	0.9791
2nd	0.9998	0.9999	0.9995
3rd	0.9992	1.0000	0.9811
4th	0.9959	0.9998	0.9978

Table 5.2 Frequency Identification by FFT and ERA

	FFT	ERA	Model
mode	Case 1: $M_c/M_b = 0.10$, $a=0.25$		
1st	11.21 rad/sec	10.73 rad/sec	10.02 rad/sec
2nd	61.63	62.33	60.76
3rd	162.50	162.04	160.46
4th	326.39	326.67	323.07
mode	Case 2: $M_c/M_b = 0.33$, $a=0.80$		
1st	8.41 rad/sec	6.29 rad/sec	7.94 rad/sec
2nd	63.04	63.31	64.65
3rd	166.70	166.51	169.96
4th	310.98	310.67	310.66
mode	Case 3: $M_c/M_b = 0.65$, $a=0.50$		
1st	8.41 rad/sec	8.11 rad/sec	9.40 rad/sec
2nd	44.83	44.58	50.66
3rd	152.69	153.54	176.12
4th	288.57	288.95	295.77

5.2.3 Response Comparison

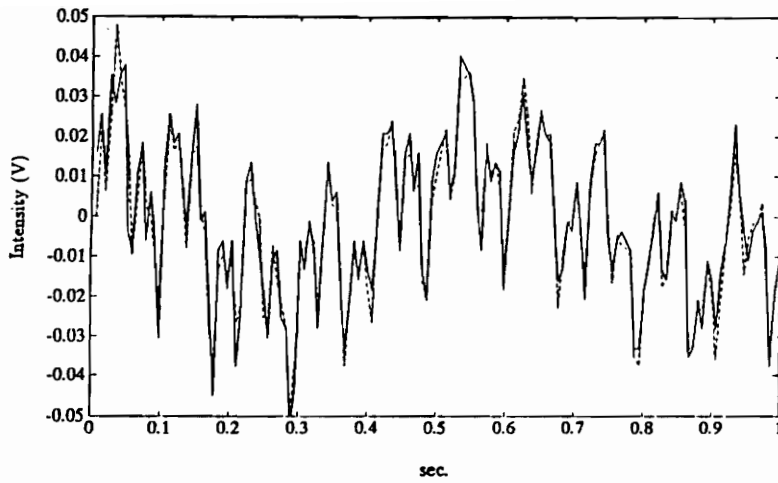
Figure 5.7 shows the responses of experimental and identified systems to the same pulse input. The three plots correspond to the three concentrated mass cases discussed previously. In Figure 5.7a the beam was loaded with the smallest concentrated mass. Figures 5.7b and 5.7c show the identified and actual responses for the middle and larger masses respectively. The plots show relatively good agreement in all three cases. The slight phase shift is due to the increased pulse width of the input pulse, as was seen in the identified response in Chapter 4.

Magnitude responses for all three systems described above are presented in Figure 5.8. The shift in resonant peaks is due to the different concentrated mass locations and quantities. The number of peaks reflect the number of underdamped modes present in the system. The location of each resonant peak compares well with the identified frequencies determined earlier. This gives further validity to the identification under changing mass conditions.

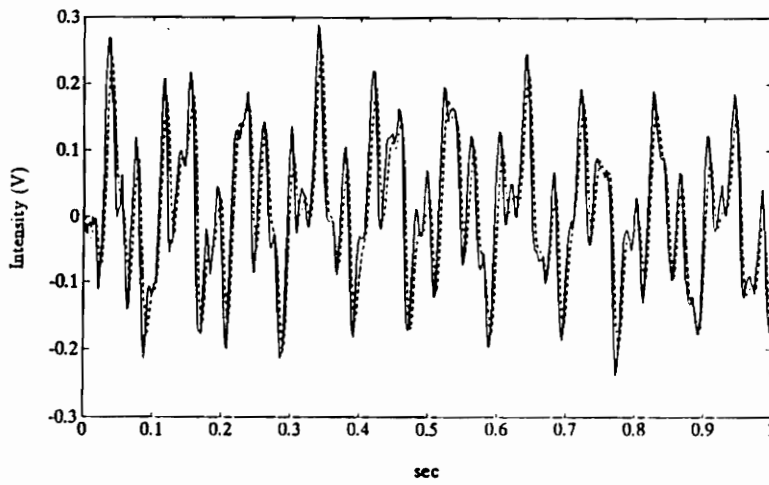
5.3 MASS IDENTIFICATION FROM SIMULATION

5.3.1 Frequency Analysis

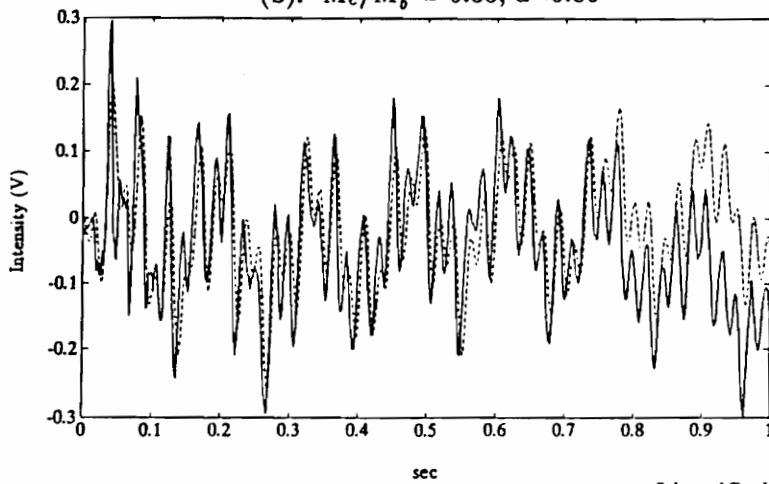
In Chapter 3, the frequencies for a cantilevered beam with variable concentrated mass were derived. Figure 3.1 displays the first four vibration frequencies as a function of both mass position and mass-to-beam ratio. For any given mode, there may exist a number of locations and masses that are similar in



(a). $M_c/M_b = 0.10, a=0.25$



(b). $M_c/M_b = 0.33, a=0.80$

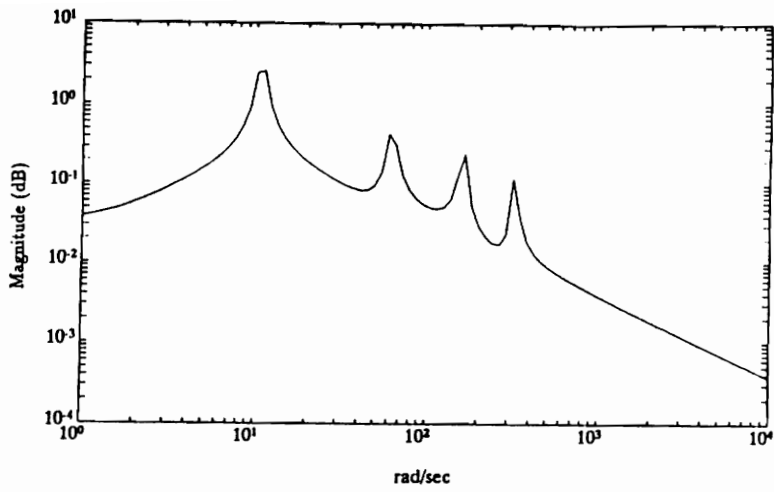


(c). $M_c/M_b = 0.65, a=0.50$

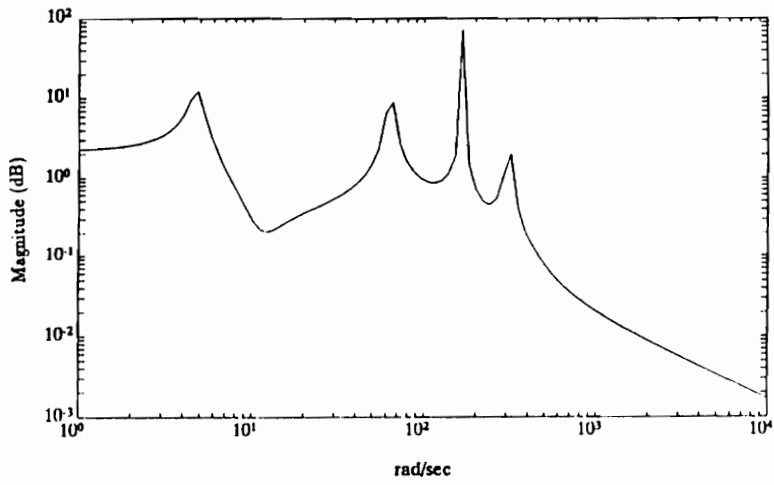
Identified -----

Actual —————

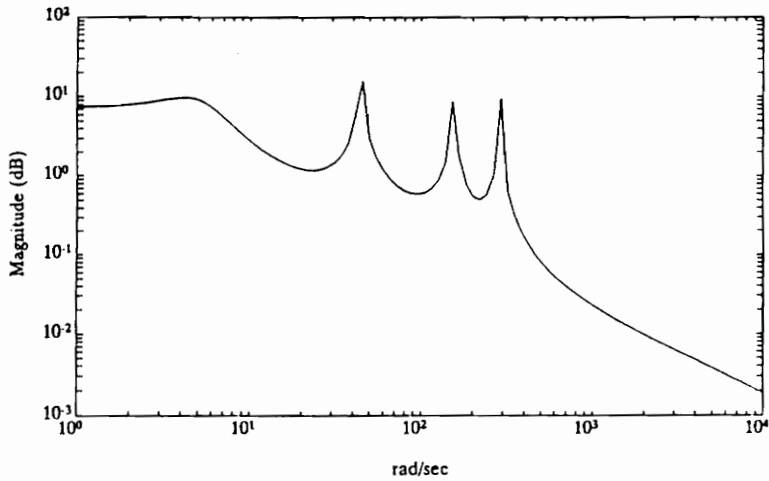
Figure 5.7 Identified and Actual Responses for Varying Mass Loads



(a). $M_c/M_b = 0.10, a=0.25$



(b). $M_c/M_b = 0.33, a=0.80$



(c). $M_c/M_b = 0.65, a=0.50$

Figure 5.8 Identified Bode Plots for Varying Mass Loads

frequency. However, if all of the four modes are compared at once, it is clear that the choices for the location and mass quantity are narrowed down considerably.

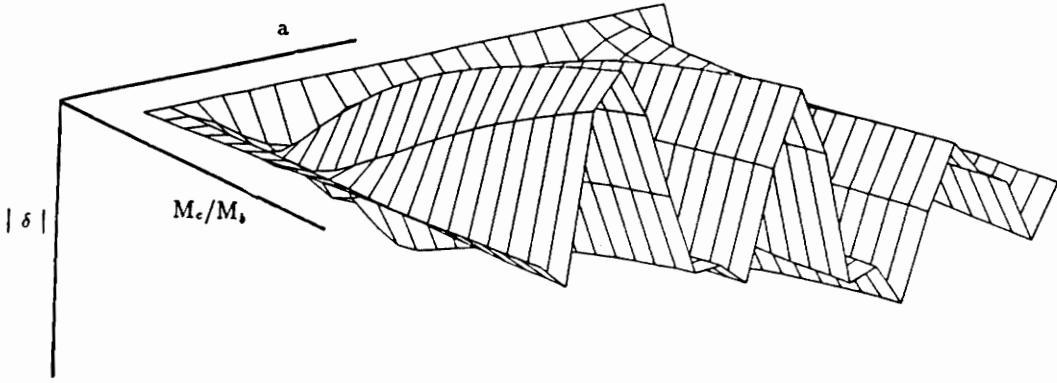
Mass identification in this case can be thought of as looking for a solution that minimizes some norm in a four-mode space. Identified frequencies are compared to a matrix of theoretical ones for a large number of locations and masses and an error norm is defined as

$$|\delta| = \sqrt{(\omega_1 - \tilde{\omega}_1)^2 + (\omega_2 - \tilde{\omega}_2)^2 + (\omega_3 - \tilde{\omega}_3)^2 + (\omega_4 - \tilde{\omega}_4)^2}, \quad (5.1)$$

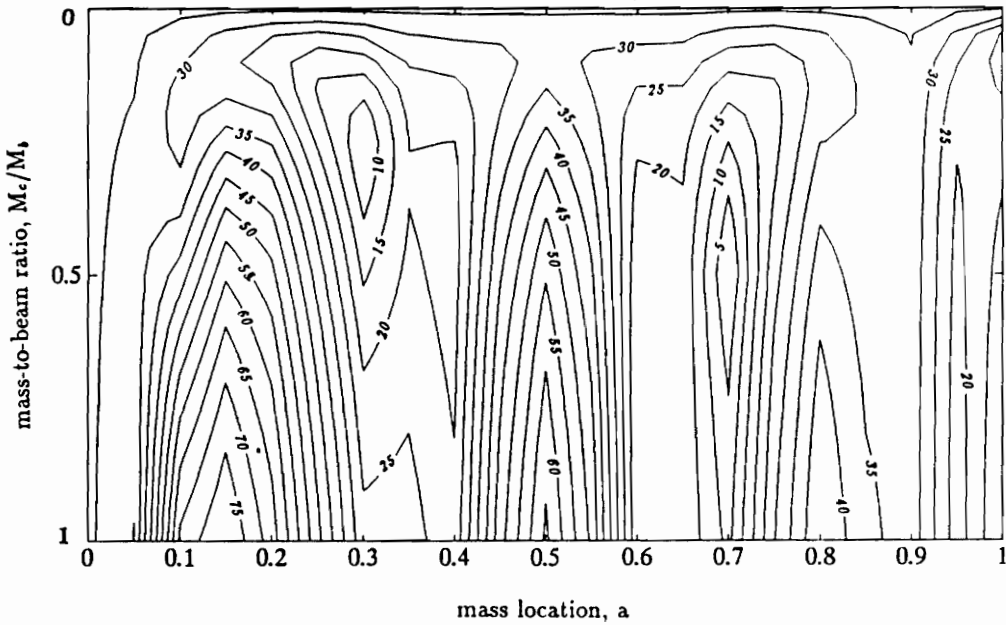
where $\tilde{\omega}_i$, refers to the i th identified natural frequency. The resulting matrix contains error norms for each set of frequencies at a specific mass location and mass-to-beam ratio. Ideally, the norm with the lowest value will correspond to the mass location and mass-to-beam ratio.

The first four frequencies were determined for simulated mass conditions of $M_c/M_b = 0.5$ and $a = 0.7$. These frequencies were compared to a theoretical matrix of frequencies and error norms determined as in (5.1). Figure 5.9 show both a 3-D and contour plot of the error norms. By looking at the three dimensional plot as well as the contour plot, it is clear that the mass-to-beam ratio is $M_c/M_b = 0.5$, and the location is $a = 0.7$. Elongation of peaks and valleys along the M_c/M_b axis shows that the mass quantity will be harder to determine than the location.

This type of parameter identification is only suited to situations where a lot of information is known about the parameter change *a priori*. In this experiment, it was known that a concentrated mass was applied at a point along the beam. However, in situations where damage detection is sought, it would be highly unlikely that the frequencies for all possible damage situations could be



(a). 3-D Plot of the Error Norms, $|\delta|$.



(b). Contour Plot of Error Norms, $|\delta|$

Figure 5.9 Error Norms for an Identified Four Mode Simulated System

theoretically derived. In such cases, the techniques developed in chapter 2 should be employed.

5.4 MASS IDENTIFICATION FROM EXPERIMENT

The methods described in the previous section were applied to the experiment and tested to see how well mass location and amount could be identified. Because the model and the experiment diverge for large concentrated masses, the experimental masses were kept small.

Three different cases were attempted, all using a concentrated mass such that $M_c/M_b = 0.106$. The three cases involved placing the mass at locations $a=0.25$, $a=0.60$, and $a=0.95$. A short pulse was applied to the beam, and the frequencies of vibration identified. Identified frequencies were compared to a theoretical matrix of frequency values and the lowest error norm searched for. The results of this algorithm are given in Table 5.3.

The most striking feature of Table 5.3 is that the position of the mass is identified with outstanding accuracy, while the mass amount is subjected to less accuracy. The explanation of this is quite clear by looking at the original 3-D plots of the frequency variations in Figure 3.1. For a given mass position along the beam, small mass increases will change the frequencies very little. For a given concentrated mass however, the frequencies may change drastically for small position changes. Thus, mass position is easier to resolve than mass quantity.

As mentioned before, the errors that contribute to the identification can lead to wrong estimates of the mass location and amount. By inspecting the plots

Table 5.3 Actual and Identified Mass Parameters

	Actual	Identified
Parameter	Case 1	
M_c/M_b	0.10	0.15
a	0.25	0.25
Parameter	Case 2	
M_c/M_b	0.10	0.05
a	0.95	1.00
Parameter	Case 3	
M_c/M_b	0.10	0.20
a	0.60	0.60

of the error norms as seen in the previous section, a neighborhood of the most likely area for the parameter change can be found. Plots of this nature are valuable in generating a “first approximation” of the parameter change. They could also be used to validate the estimates of other parameter identification techniques.

6.0 CONCLUSIONS

6.1 SUMMARY

This work has discussed the issues related to identification of a flexible beam using a fiber-optic sensor. Of major importance has been the instrumentation of this sensor on a cantilevered beam, and the identification of the system under a variety of parameter changes. The significant points in this process are summarized below.

The most important parameter identification techniques were presented in Chapter 2. The techniques are broken down along two main lines - sensitivity methods that recursively update a set of parameters based on measurements, and direct methods that seek to find a "best fit" of the parameters within a set of constraints.

A number of possibilities exist for using this fiber sensor for damage detection and parameter identification. Techniques that lend themselves most readily to the current sensor (single input-single output, uniformly weighted) are the sensitivity methods described in section 2.1. It was shown in Chapter 5 that the fiber sensor was able to identify the natural frequencies of the beam quite clearly, and these identified frequencies could be used to generate estimates to the

mass and stiffness changes. In fact, the technique that was carried out for the mass identification in Chapter 5 was a type of “sensitivity” analysis - relating the changes in frequency to the changes in the mass parameters. Because the only information that is required are identified frequencies, a single fiber placed along a structure would be adequate. Additional sensors would insure that modal information was not lost as was shown in section 5.3.1.

The model of the system was developed in Chapter 3 and used to provide simulated data to the ERA presented in Chapter 4. This algorithm depended on an impulse response estimate, and various ways of obtaining this estimate were described in Chapter 4 as well. A comparison of the ETFE and pulse input methods showed that both identified a model of the cantilevered beam. Identified system parameters were shown to match closely with theoretical ones.

Averaging of the measured signals provided no significant reduction in noise in the system. Measurements were recorded and used directly in the identification process, without any further signal conditioning performed.

Chapter 5 presented the results of various mass loadings on the beam. A comparison of the natural frequencies of the system as a concentrated mass is varied along the beam showed that the frequencies matched well for smaller masses but degraded considerably for larger ones. This was recognized as a limitation of the defining model equations, rather than poor identification. Experimental results showed that the location of the concentrated mass can be determined for small mass changes. Mass amount can be determined with lower accuracy, due to the nature of the frequency variations.

6.2 FURTHER RESEARCH

6.2.1 Spatially Weighted Fiber

The inherent problem of using the fiber sensor for identification is that the output is proportional to a spatial integral, and spatial information is lost once the light reaches the end of the fiber. As discussed in Chapter 3, the output becomes proportional to the derivative of the mode shape evaluated at the endpoints of the fiber. Therefore, the fiber reduces to a derivative point sensor.

If the fiber sensor can be weighted by some spatially distributed function, some of the spatial information may be retained in the output. If $w(z)$ represents some weighting function, then the equation that describes the output of the fiber can be modified from (3.43) as follows

$$I_f(t) = \frac{\alpha I_p t_b}{4} \sum_{i=1}^{\infty} \eta_i(t) \int_{z_1}^{z_2} w(z) \psi_i''(z) dz. \quad (6.1)$$

The simplest non-uniform weighting that can be used is

$$w(z) = \delta(z - z_j), \quad (6.2)$$

where z_j is a point along the beam. Substituting (6.2) into (6.1) and performing the integration yields

$$I_f(t) = \frac{\alpha I_p t_b}{4} \sum_{i=1}^{\infty} \eta_i(t) \psi_i''(z_j). \quad (6.3)$$

Equation (6.3) relates the intensity to the mode shape 2nd derivatives evaluated at a point z_j along the beam. In this configuration, the weighting changes the fiber into a strain gauge.

Other spatial weighting functions could be thought of as projecting the strain information onto a set of basis functions through the spatial integration. For instance, if the weighting function is taken as

$$w(z) = \psi_j''(z) \tag{6.4}$$

and the structure has a uniform strain distribution, then equation (6.1) becomes

$$I_j(t) = \frac{\alpha I_p t_b}{4} \eta_i(t) E_b I \delta_{ij} \tag{6.5}$$

due to the orthogonality of $\psi_i''(z)$ with respect to $E_b I$. In this case, all of the spatial information is projected onto one basis - corresponding to the j th mode of the structure. Parameter changes to the system will cause the projections onto the basis functions to change. Analyzing these projections may aid in the identification process. Other weighting functions may make it possible to back out information about the system parameters.

6.1.2 Mode Shape Detection

One possible method of obtaining spatial information is to use many varying length fibers distributed over the same area. Since the ends of the fiber

define the point at which the mode derivative is to be evaluated, a series of fibers attached to a beam could provide a number of mode derivative values. A single laser could provide the source light into all sensors at once, and the various outputs recorded and processed off line.

The ERA algorithm would provide an excellent choice for identification since the identified values in the $C\Phi$ matrix are proportional to the mode shape derivatives. These values can be scaled appropriately as was shown in section 4.1. Obviously, the more measurements are available, the better the interpolation to the mode derivative and approximation of the mode shape.

Another alternative to using many different fiber lengths is to pick off the intensity pattern at various points along the fiber length. An in-line beam splitter that successfully isolates one of the two lobed intensity patterns while allowing the other to pass through has been demonstrated [33]. A series of such beam splitters could provide spatially discrete data at various points along one length of fiber, provided that losses are kept to a minimum at each splitter interface. A potential drawback is that such in-line beam splitters are very difficult to manufacture and their viability in a series configuration is questionable.

If the mode shapes of the structure can be estimated within reasonable accuracy, then the direct methods of Chapter 2 can be applied to the identification problem. There are two problems that must be addressed, however. The first is a problem of interpolation. Given a number of discrete data points, one needs to find a continuum of values that will best fit the problem at hand. The second problem is integration. Since the output of the fiber sensor is spatial derivative data, this information must be interpolated and integrated to generate the required mode shapes.

APPENDIX A: SIMULATION PROGRAMS

The computer programs that were written to simulate the beam, fiber, and piezo are included in this appendix. The programs solve the eigenvalue problem and find the mode shapes and mode derivatives given the concentrated mass conditions. A number of subroutines are included, including a Simpson's rule integration program and a orthogonalization program.

```

%*****
%
% This program estimates eigenvalues and mode shapes for a
% clamped-free beam with an arbitrary mass located on the beam.
% The eigenvalues are estimated via a very crude root finding
% method, and then passed to a secant method for refinement.
% The length of the beam is normalized to be unity.
%
% inputs:   mrat - mass/beam ratio
%           a - distance from root to mass (0-1)
%           m - # modes desired
%
% function/file calls:  eigen.m      arbshape.m
%                       ortho.m     newbeam.mat (beam specs)
%
% returns:  mode - matrix of normalized mode shapes
%           x - beam spatial values (sampled at 0.01)
%           norm - normalization constants
%           y - eigenvalues of characteristic equation
%*****

load newbeam
clear mode,clear model,clear mode2

mrat=input('Input the nonzero mass/beam ratio, mrat= ');
a=input('Input the (normalized) distance of the mass from root, a= ');
m=input('Input the number of modes, m= ');

dt=.5;
b=1-a;
t=[0:dt:30];
n=max(size(t));

for i=1:n
    func(i)=eigen(t(i),a,mrat);
end

%*****
% The roots of the equation are estimated by looking at points
% in the domain where the range changes sign.
%*****

clear y;
chk1=-1;
for j=2:n
    chk2=sign(func(j));
    if chk2~=chk1
        y=[y;t(j)];
        chk1=chk2;
    end
end
end

```

```

%*****
% The first m eigenvalues are now refined using the secant method.
%*****

for i=1:m
i
yone=y(i);
ytwo=y(i)-dt/2;
eps=1;

while eps>1.e-12
    temp1=(ytwo-yone)*eigen(ytwo,a,mrat);
    temp2=(eigen(ytwo,a,mrat)-eigen(yone,a,mrat));
    ythr=ytwo-temp1/temp2;
    eps=ythr-ytwo;
    yone=ytwo;
    ytwo=ythr;
    eps=abs(ytwo-yone);
end

y(i)=ythr;

end

y=y(1:m)

%*****
% Calculation of normalizing coefficients and mode shapes
%*****

x=[0:.01:1];

if mrat==0
    for j=1:m
        j
        mode = [mode;endshape(y(j),x)];
        mode1 = [mode1;0,(diff(mode(j,:))./diff(x))/l]];
        mode2 = [mode2;0,(diff(mode1(j,:))./diff(x))/l]];
    end

    norm=ortho(mode,mrat*mb,mb,1,m);
end

if mrat ~ =0
    for j=1:m
        j
        mode= [mode;arbshape(y(j),x,a,mrat,mb)];
        mode1=[mode1;0,(diff(mode(j,:))./diff(x))/l]];
        mode2=[mode2;0,(diff(mode1(j,:))./diff(x))/l]];
    end
end

```

```

    norm=ortho(mode,mrat*mb,mb,a,m);
end

for j=1:m
    if mode(j,2)<0
        flip(j)=-1;
    else flip(j)=1;
    end
end

for i=1:m
    mode(i,:)=flip(i)/sqrt(norm(i,i))*mode(i,:);
    mode1(i,:)=flip(i)/sqrt(norm(i,i))*mode1(i,:);
    mode2(i,:)=flip(i)/sqrt(norm(i,i))*mode2(i,:);
end

omega=y.^2*sqrt((Eb*I)/(mb*l^3));

clear temp1,clear temp2,clear yone,clear ytwo,clear ythr,clear t
clear zta,clear chk1,clear chk2,clear documentation,clear func
clear f1,clear f2,clear Eb,clear i,clear j,clear dt,clear bh
clear I,clear d31,clear b,clear n,clear p1,clear p2,clear tp
clear shape,clear rho,clear Ep,clear tb

```

```

%*****
% -This program generates the state space model for a clamped free beam
%   with a variable mass placed anywhere along the beam.
% -A Modal domain sensor is assumed to run out and back between f1 and f2.
% -A piezoelectric is used as an actuator, located between p1 and p2.
% -The stiffness of the piezo is considered negligible.
% -An m mode model is used.
% -The analysis follows that of Crawley & de Luis, AIAA Journal Oct. 1987.
%
% Requires:
% rho   - density, mass/unit volume
% Eb    - Young's modulus of beam
% Ep    - Young's modulus of piezo
% bh    - beam height
% l     - beam length
% f1,f2 - end points of fiber
% p1,p2 - end points of piezo patch
% tb    - thickness of beam
% tp    - thickness of piezo
% d31   - piezo strain coefficient (charge constant)
% zta   - damping factor (0-1)
%
% Returns:
% A,B,C - State space matrices
% *****

```

```
load newbeam
```

```

%*****
% Input the locations of the fiber ends. A vector of several end
% locations may be used to simulate multiple fibers.
%*****

```

```

f1=input('Input left end locations of fiber, f1= ');
f2=input('Input right end locations of fiber, f2= ');
scale=64e+5;
p=1;

```

```
psi=(Eb*tb*hb)/(Ep*tp*hp);
```

```

%*****
% Generate elements of coefficient matrices to 2nd order diffeq system
% M*r'' + Cd*r' + (Kb+Kp)*r = R*u; r - modal amp., u - voltage on piezo.
%*****

```

```
for i=1:m
```

```
    k(i)=omega(i)^2;
```

```
    if mrat=0
```

```
        kp(i)=Eb*tb^3*hb/(2*l^3*(6+psi))*(1/sqrt(norm(i,i)))*...
```

```

        (endder2(y(i),p2/l,l)*endder1(y(i),p2/l,l)-...
        endder2(y(i),p1/l,l)*endder1(y(i),p1/l,l));

R(i)=-Eb*tb^2*hb*d31/(l*(6+psi)*tp)*(1/sqrt(norm(i,i)))*...
        (endder1(y(i),p2/l,l)-endder1(y(i),p1/l,l));

for j=1:p
    c(j,i)=scale*(tb/2)*(1/sqrt(norm(i,i)))...
            *(endder1(y(i),f2(j),l)-endder1(y(i),f1(j),l));
end
end

if mrat~=0

kp(i)=Eb*tb^3*hb/(2*l^3*(6+psi))*(1/sqrt(norm(i,i)))*...
        (arbder2(y(i),p2/l,a,mrat,l)*arbder1(y(i),p2/l,a,mrat,l)-...
        arbder2(y(i),p1/l,a,mrat,l)*arbder1(y(i),p1/l,a,mrat,l));

R(i)=-Eb*tb^2*hb*d31/(l*(6+psi)*tp)*(1/sqrt(norm(i,i)))*...
        (flip(i)*arbder1(y(i),p2/l,a,mrat,l)...
        -flip(i)*arbder1(y(i),p1/l,a,mrat,l));

for j=1:p
    c(j,i)=scale*(tb/2)*(1/sqrt(norm(i,i)))*...
            (flip(i)*arbder1(y(i),f2(j),a,mrat,l)...
            -flip(i)*arbder1(y(i),f1(j),a,mrat,l));
end
end

end

M=eye(i,i);
K=diag(k)+diag(kp);
Mi=inv(M);
MiR=Mi*(R');
MiK=Mi*K;

for i=1:m
    MiD(i,i)=2*zta(i)*sqrt(MiK(i,i));
end

% *****
% Convert to first order diffeq system x'=Ax+Bu y=Cx with x=[r;r']
% *****

A=[zeros(m,m),eye(m);-MiK,-MiD];
B=[zeros(m,1);MiR];
C=[c,zeros(p,m)];
d=zeros(p,1);
xo=zeros(2*m,1);

clear c,clear d31,clear i,clear k,clear scale

```

```
clear l,clear p2,clear p1,clear psi,clear rho,clear rho1,clear f1,clear f2
clear tb,clear tp,clear zta,clear MiD,clear Eb,clear Ep,clear I,
clear Mi,clear MiR,clear R,clear bh,clear MiK,clear j
```

```

function y=eigen(x,a,mrat)

%*****
%
% Evaluates the eigenvalue equation for an euler beam
% with arbitrarily placed mass.
%
% x - value in the domain of the function
% a - distance from root to mass
% mrat - mass/beam ratio
%
%*****

b=1-a;

num=2*(1+cosh(x)*cos(x));
den1=(1-cosh(x*a)*cos(x*a));
den2=(sinh(x*b)*cos(x*b)-cosh(x*b)*sin(x*b));
den3=(1+cosh(x*b)*cos(x*b));
den4=(cosh(x*a)*sin(x*a)-cos(x*a)*sinh(x*a));
y=mrat*x*(den1*den2+den3*den4)-(num);

```

```

%*****
% This program provides an orthogonality check for mode shapes
% of a cantilevered beam with variable concentrated mass.
%
% Inputs are:
%     a - position of the mass
%     mc - concentrated mass
%     mb - beam mass
%     mode - a matrix containing the mode shapes
%     m - # modes
%
% function calls: simp.m
%
% returns:      norm - m x m matrix of normalization constants
%
% norm=ortho(mode,mc,mb,a,m)
%*****

function norm=ortho(mode,mc,mb,a,m)

xa=a*100+1;

for i=1:m
for j=1:m
norm(i,j)=mb*simp(mode(i,:).*mode(j,:),.01)+mc*mode(i,xa)*mode(j,xa);
end
end

```

```

%*****
%
% This program numerically integrates a vector of function
% values in a composite Simpson's rule algorithm. The number
% of elements in the function vector must be an odd number.
% The spacing between function values is given by h.
%
%*****

function y=simp(f,h)

n=max(size(f));
temp1=0;
temp2=0;

for j=1:(n-3)/2
    temp1=temp1+f(2*j+1);
end

for j=1:(n-1)/2
    temp2=temp2+f(2*j);
end

y=(h/3)*(f(1)+2*temp1+4*temp2+f(n));

```

```

%*****
% This is a function call to evaluate mode shapes for the
% case of an arbitrarily placed variable mass. Eigenvalues
% are input one at a time.
%
% variables:
%
% k - eigenvalue cooresponding to mode
% x - vector of beam length coordinates
% a - distance from root to mass
% mrat - mass/beam ratio
%
% Format: mode=arbshape(k,x,a,mrat,mb)
%*****

function mode=arbshape(k,x,a,mrat,mb)
b=1-a;

den=1+cosh(k)*cos(k);

num1a=(cosh(k*b)+cos(k*b))*(sinh(k)+sin(k));
num1b=(sinh(k*b)+sin(k*b))*(cosh(k)+cos(k));
num1=(num1a-num1b);

num2a=(sinh(k*b)+sin(k*b))*(sinh(k)-sin(k));
num2b=(cosh(k*b)+cos(k*b))*(cosh(k)+cos(k));
num2=(num2a-num2b);

n=max(size(x));

for i=1:n

    mode(i)=(num1*mrat*k/(den*4))*(cosh(k*x(i))-cos(k*x(i)));
    mode(i)=mode(i)+(num2*mrat*k/(den*4))*(sinh(k*x(i))-sin(k*x(i)));

    if x(i)>a
        mode(i)=mode(i)+(mrat*(k/2))*(sinh(k*(x(i)-a))-sin(k*(x(i)-a)));
    end

end
end

```

```

%*****
% This function determines the 1st derivative of the mode shape
% for the arbitrarily placed mass, given either a specific
% coordinate, or a vector of values
%*****

function dy=arbder1(k,x,a,mrat,l)
b=1-a;

den=1+cosh(k)*cos(k);

num1a=(cosh(k*b)+cos(k*b))*(sinh(k)+sin(k));
num1b=(sinh(k*b)+sin(k*b))*(cosh(k)+cos(k));
num1=(num1a-num1b);

num2a=(sinh(k*b)+sin(k*b))*(sinh(k)-sin(k));
num2b=(cosh(k*b)+cos(k*b))*(cosh(k)+cos(k));
num2=(num2a-num2b);

n=max(size(x));

for i=1:n

    dy(i)=(num1*(mrat)*(k^2)/(den*4*1))*(sinh(k*x(i))+sin(k*x(i)));
    dy(i)=dy(i)+(num2*mrat*(k^2)/(den*4*1))*(cosh(k*x(i))-cos(k*x(i)));

    if x(i)>a
        dy(i)=dy(i)+(mrat*k^2/(2*1))*(cosh(k*(x(i)-a))-cos(k*(x(i)-a)));
    end

end
end

```

```

%*****
% This function determines the 2nd derivative of the mode shape
% for the arbitrarily placed mass, given either a specific
% coordinate, or a vector of values. The result is scaled
% so that dy2 is the 2nd derivative of the normalized mode shape.
%
% Format: dy2=arbder2(k,x,a,mrat,l)
%*****

function dy2=arbder2(k,x,a,mrat,l)
b=1-a;

den=1+cosh(k)*cos(k);

num1a=(cosh(k*b)+cos(k*b))*(sinh(k)+sin(k));
num1b=(sinh(k*b)+sin(k*b))*(cosh(k)+cos(k));
num1=(num1a-num1b);

num2a=(sinh(k*b)+sin(k*b))*(sinh(k)-sin(k));
num2b=(cosh(k*b)+cos(k*b))*(cosh(k)+cos(k));
num2=(num2a-num2b);

n=max(size(x));

for i=1:n

    dy2(i)=(num1*(mrat)*(k^3)/(den*4*l^2))*(cosh(k*x(i))+cos(k*x(i)));
    dy2(i)=dy2(i)+(num2*mrat*(k^3)/(den*4*l^2))*(sinh(k*x(i))+sin(k*x(i)));

    if x(i)>a
        dy2(i)=dy2(i)+(mrat*k^3/(2*l^2))*(sinh(k*(x(i)-a))+sin(k*(x(i)-a)));
    end

end
end

```

```

%*****
% This function evaluates modeshapes for the end mass condition
% given an eigenvalue (k) and a range parameter.
%*****

```

```

function y=endshape(k,x)

eps=(cos(k)+cosh(k))/(sin(k)+sinh(k));

y=1/2*(cosh(k*x)-cos(k*x)-eps*(sinh(k*x)-sin(k*x)));

```

```

%*****
% This function call evaluates the derivative of the mode shape
% (for a given eigenvalue, k) at a given point in the domain (x).
% This holds only for the endmass condition
%*****

```

```

function y=endder1(k,x,l)

eps=(cos(k)+cosh(k))/(sin(k)+sinh(k));

y=(k/(2*l))*(sin(k*x)+sinh(k*x)-eps*(cosh(k*x)-cos(k*x)));

```

```

%*****
% This function evaluates the second derivative of the mode shape
% (for a given eigenvalue, k) at points in the domain (x). This
% routine only holds for the case of an endmass.
%*****

```

```

function y=endder2(k,x,l)

eps=(cos(k)+cosh(k))/(sin(k)+sinh(k));

y=(k^2/(2*l^2))*(cos(k*x)+cosh(k*x)-eps*(sinh(k*x)+sin(k*x)));

```

APPENDIX B: IDENTIFICATION PROGRAMS

The programs that were developed for the identification process are included in this appendix. These programs include the Eigensystem Realization Algorithm and the Empirical Transfer Function Estimator, and the Modal Amplitude Coherence Measures. Also included is a program that compares theoretical frequencies to the identified frequencies and estimates the position and mass from the lowest error norm. All programs were written using MATLAB.

```

%*****
%
% This is a program to do identification using the Eigensystem
% Realization Algorithm. The impulse response to a set of state-
% space equations is found and the Hankel matrix is formed. From
% this, an estimate of A,B,and C are found.
%
%*****

n=input('Input the order of the Hankel Matrix, n= ');
h=input('Actual or Estimated impulse response? h= ');
p=min(size(h));

clear nshape,clear hank

for i=1:n+1
    clear temp
    for j=1:n+1
        temp=[temp,h(:,j+i)];
    end
    hank=[hank;temp];
end

h0=hank(1:p*n,1:n);
h1=hank(1:p*n,2:n+1);
clear hank,clear h,clear temp

% Do the Singular Value Decomposition

[P,S,Q]=svd(h0);
clear h0

% Check for non-zero values and determine the order.

singval=diag(S);

format long e

if max(size(singval))>20
    singval(1:20)
else
    singval
end

format short

eps=input('Input the tolerance, eps= ');

r=0;

for i=1:n
    if singval(i) > eps

```

```

    r=r+1;
  end
end

sr=S(1:r,1:r)
pr=P(:,1:r);
qr=Q(:,1:r);

clear S
clear Q
clear P

sinv=inv(sr);
sinv2=sqrt(sinv);

z=zeros(p*(n-1),p);
em=[1;zeros(n-1,1)];
ep=[eye(p,p);z];

adid=sinv2*pr'*h1*qr*sinv2;
bdid=sqrt(sr)*qr'*em;
cdid=ep'*pr*sqrt(sr);
d=zeros(p,1);

[xx,dd]=eig(adid);
modamp=inv(xx)*bdid;
modshp=cdid*xx;

dd

clear z,clear sinv2,clear sinv,clear pr
clear em,clear ep,clear h1,clear r

```

```

%*****
% This program calculates the discrete unit response to a
% system given a forced input/output pair. The identification
% is done using the Empirical Transfer Function Estimate (which
% calculates the discrete transfer function values) and then
% performs an inverse FFT to find the discrete impulse response.
% Input and output data are zero padded to n ( $n=2^i$ ,  $i=1,2,3,\dots$ ).
% Multiple input/output pairs are possible, and are used to
% average out noise effects in the data.
%*****

% Read in the values of the input and output data

u=input('Input the name of the input data, u= ');
y=input('Input the name of the output data, y= ');
n=input('Input the value of n (n < # pts,  $n=2^i$ ), n= ');

% Zero padding on input and output

u=[u;zeros(n-max(size(u)),min(size(u)))];
y=[y;zeros(n-max(size(y)),min(size(y)))];

% Calculate transfer function estimate

uf=fft(u);
yf=fft(y);

clear u
clear y

hf=yf./uf;

hf=[hf(1:n/2+1);conj(hf(n/2:-1:2))];

clear yf
clear uf

hest=ifft(hf);
hest=real(hest)';

clear hf
clear n

```

```

%*****
% Check the modal amplitude coherence value
%*****

ss=input('Input the continuous eigenvalues, ss= ');

clear quebar

que=(inv(xx)*sqrt(sr)*qr)';
bee=(modamp)';

for j=1:size(dd)
    clear quebarj
    for i=1:max(size(qr))
        quebarj=[quebarj,exp(dt*(i-1)*ss(j))];
    end
    quebar=[quebar;quebarj*bee(j)];
end

for j=1:size(dd)
    macgamma(j)=abs(quebar(j,:)*que(:,j))/...
        sqrt(abs(quebar(j,:)*quebar(j,:)'*abs(que(:,j))*que(:,j)));
end

macgamma=macgamma'

clear quebar,clear quebarj,clear que,clear ss,clear bee

```

```

%*****
% This program draws comparisons between the theoretical frequencies for
% a beam with arbitrarily placed mass, and the identified ones. The file
% reads in data from a known matrix of beam frequencies and calculates
% a norm between all possible values (121) of the first four modes.
% It then returns an 11x11 matrix of norms from which the user can
% determine the lowest.
%*****

est=input('Input the first four estimated values, est= ');
theo=input('Input the matrix of theoretical values, theo= ');

temp=1e+20;

for i=1:21
for j=1:21
diff(i,j)=sqrt((theo(i+3*(i-1),j)-est(1))^2+...
               (theo(i+1+3*(i-1),j)-est(2))^2+...
               (theo(i+2+3*(i-1),j)-est(3))^2+...
               (theo(i+3+3*(i-1),j)-est(4))^2);
if diff(i,j)<temp
imin=i;
jmin=j;
temp=diff(i,j);
end
end
end

mratest=(imin-1)/20
aest=(jmin-1)/20

clear imin,clear jmin,clear temp,clear theo
clear est,clear i,clear j

```

REFERENCES

- [1] R. M. Measures, N. D. W. Glossop, J. Lymer, R. C. Tennyson, "Structural Integrated Fiber Optic Damage Assessment System for Composite Materials," *Proceedings of the SPIE O/E Fiber Lase*, Boston, MA, Vol. 986, September, 1988.
- [2] J. R. Dunphy and G. Meltz, "Optical Fiber Shock Wave Sensor for Composites," *Proceedings of the SPIE O/E Fiber Lase*, Boston, MA, Vol. 986, September, 1988.
- [3] R. O. Claus and J. C. Wade, "Distributed Strain Measurement in a Rectangular Plate Using an Array of Optical Fiber Sensors," *Journal of Nondestructive Evaluation*, Vol.41, p. 106, 1983.
- [4] E. Denman, T. Hasselman, C. T. Sun, J. Juang, J. L. Junkins, F. Udwadia, V. Venkayya and M. Kamat, *Identification of Large Space Structures on Orbit - AFRPL TR-86-054 Final Report*, September, 1986.
- [5] N. G. Creamer and S. L. Hendricks, "Structural Parameter Identification Using Modal Response Data," *Proceedings of the Fifth VPI&SU/AIAA Symposium on Dynamics and Control of Large Flexible Spacecraft*, Blacksburg, VA, 1985.
- [6] M. A. Norris and L. Meirovitch, "On the Problem of Modelling for Parameter Identification in Distributed Structures," *International Journal for Numerical Methods in Engineering*, Vol. 28, pp. 2451-2463, 1989.
- [7] L. Meirovitch, **Elements of Vibration Analysis**, McGraw-Hill, New York, 1986.
- [8] J. C. Chen and J. A. Garba, "Analytical Model Improvement Using Modal Test Results," *AIAA Journal*, Vol. 18, No. 6, pp. 684-690, June 1980.
- [9] A. Berman, "Mass Matrix Correction Using an Incomplete Set of Measured Modes," *AIAA Journal*, Vol. 17, pp. 1147-1148, October 1979.

- [10] A. Berman and E. J. Nagy, "Improvement of a Large Analytical Model using Ground Vibration Test Data," *AIAA Journal*, Vol. 21, pp. 1168-1173, August 1971.
- [11] C. W. White and B. D. Maytum, "Eigensolution Sensitivity to Parametric Model Perturbations," *Shock and Vibration Bulletin*, Vol. 46, Part 5, pp. 123-133, 1976.
- [12] H. Baruh and L. Meirovitch, "Parameter Identification in Distributed Systems," *Journal of Sound and Vibration*, Vol. 101, No. 4, pp. 551-564, 1985.
- [13] P. Hajela and F. J. Soeiro, "Structural Damage Detection Based on Static and Modal Analysis," *Proceedings of the 30th SDM Conference*, Mobile, AL, April 1989.
- [14] C. A. Kircher, *Ambient and Forced Vibration Analysis of Full Scale Structures*, Ph.D. Dissertation, Stanford University, November 1977.
- [15] W. M. West Jr., "Single Point Random Modal Test Technology Application to Failure Detection," *The Shock and Vibration Bulletin*, pp. 25-31, May 1982,
- [16] S. W. Smith and S. L. Hendricks, "Damage Detection and Location in Large Space Trusses," *AIAA SDM Issues of the International Space Station, A Collection of Technical Papers*, Williamsburg, VA, pp. 56-63, 1988.
- [17] A. M. Kabe, "Stiffness Matrix Adjustment Using Mode Data," *AIAA Journal*, Vol. 23, No.9, pp. 1431-1436, September 1985.
- [18] F. J. Soeiro and P. Hajela, "Damage Detection in Composite Materials Using Identification Techniques," *Proceedings of the 31st SDM Conference*, March 1990.
- [19] R. P. Goel, "Vibrations of a Beam Carrying a Concentrated Mass," *Transactions of the ASME, Journal of Applied Mechanics*, pp. 821-822, September 1973.
- [20] P. A. A. Laura, J. L. Pombo and E. A. Susemihl, "A Note on the Vibrations of a Clamped-Free Beam with a Mass at the Free End," *Journal of Sound and Vibration*, Vol. 37, No. 2, pp. 161-168, 1974.
- [21] Y. Chen, "On the Vibration of Beams or Rods Carrying a Concentrated Mass," *Transactions of the ASME, Journal of Applied Mechanics*, pp. 310-311, June 1963.
- [22] C. D. Butter and G. B. Hocker, "Fiber Optics Strain Gauge," *Applied Optics*, Vol. 17, No. 18 pp. 2867-2869, September 1978.

- [23] D. E. Cox, *Active Control of Flexible Structures using Fiber Optic Modal Domain Sensors*, M.S. Thesis, Virginia Tech, June 1990.
- [24] B. D. Duncan, *Modal Interference Techniques for Strain Detection in Few-Mode Optical Fibers*, M. S. Thesis, Virginia Tech, March 1987.
- [25] D. E. Cox and D. K. Lindner, "Active Control for Vibration Suppression in a Flexible Beam Using a Modal Domain Optical Fiber Sensor," submitted to *ASME Journal of Vibration and Acoustics*, July 1990.
- [26] E. F. Crawley and J. de Luis, "Use of Piezoelectric Actuators as Elements of Intelligent Structures," *AIAA Journal*, pp. 1373-1385, October 1987.
- [27] J. Juang and R. S. Pappa, "An Eigensystem Realization Algorithm for Modal Parameter Identification and Model Reduction," *Journal of Guidance, Control, and Dynamics*, Vol. 8, No. 5, pp. 620-627, September 1985.
- [28] S. R. Ibrahim, "A Method for the Direct Identification of Vibration Parameters from the Free Response," *Shock and Vibration Bulletin*, No. 47, pp.183-198.,1977
- [29] J. Juang and R. S. Pappa, "Effects of Noise on Modal Parameters Identified by the Eigensystem Realization Algorithm," *Journal of Guidance, Control, and Dynamics*, Vol. 9, No. 3, pp. 294-303, May-June 1986.
- [30] N. K. Sinha and B. Kuszta, **Modeling and Identification of Dynamic Systems**, Van Nostrand Reinhold Co., New York, 1983
- [31] L. Ljung, **System Identification for the User**, Prentice Hall, New York, 1987.
- [32] F. P. Beer and E. R. Johnston, **Mechanics of Materials**, McGraw-Hill Inc., New York, pp.396-400, 1981.
- [33] M. Miller, *Advances in Elliptical Core Two Mode Optical Fiber Sensors*, " MS Thesis, Virginia Tech, April 1990.

VITA

Charles Zachary Furness was born in Washington, D.C., on March 30, 1963. He grew up in Arlington, VA and graduated from Yorktown High School in the spring of 1981. In 1986 he received a Bachelor of Science degree in Physics from Virginia Polytechnic Institute and State University. In June of 1990, he received his Master of Science degree in Electrical Engineering, also from VPI & SU.

Mr. Furness is currently working for The MITRE Corporation, located in McLean, VA. His professional interests include signal processing, system theory, and communications.

A handwritten signature in black ink that reads "Charles Zachary Furness". The signature is written in a cursive style with a large, stylized 'Z' and 'F'.